Doctoral Thesis

Tungsten Oxide-Based Hydrogen Gas Sensors Prepared by Advanced Reactive Magnetron Sputtering Technique

Submitted by

Nirmal Kumar

Under the supervision of

Doc. Ing. Pavel Baroch, Ph.D.

Consultant

RNDr. Stanislav Haviar, Ph.D.

Department of Physics and NTIS

Faculty of Applied Sciences
University of West Bohemia, Pilsen

2021

Disertační práce

Senzory vodíku na bázi oxidu wolframu připravené pokročilými metodami reaktivního magnetronového naprašování

Vypracoval

Nirmal Kumar

Vedoucí práce

Doc. Ing. Pavel Baroch, Ph.D.

Konzultant

RNDr. Stanislav Haviar, Ph.D.

Katedra fyziky

Fakulta aplikovaných věd
Západočeská univerzita v Plzni

2021

Declaration

This is to certify that I prepared this doctoral thesis on 'Tungsten oxide-based hydrogen gas sensors prepared by the advanced reactive magnetron sputtering technique' to fulfill the requirement of 'Ph.D. in Plasma Physics and Thin Films' by myself. All the results presented in this thesis were obtained during my doctoral study at the Department of Physics and NTIS, Faculty of Applied Sciences, University of West Bohemia. I declare that the work done in this thesis is completely original.

Pilsen, 22.10.2021 …….

Nirmal Kumar

Acknowledgments

This acknowledgment is intended to thank all individuals for their support at every stage of this research work. Their consistent help is a dominant factor in making it possible to carry out my research successfully.

As the author of this thesis, I express my deep sense of gratitude toward ass. prof. Pavel Baroch for granting me the opportunity to undertake my Ph.D. research at the Department of Physics at the University of West Bohemia and for his invaluable guidance, support, kindness, and encouragement. I would like to express my special thanks to Dr. Stanislav Haviar for his continuous guidance, inspiration, and patience. I am also honored to meet and work with him and will never forget his advice and support. His vast knowledge and passion for science have greatly enlightened me in the field of sensor technology.

I would also like to express my thanks to Ing. Šárka Batková, ass. prof. Jiří Čapek, Dr. Jiří Rezek, ass. prof. Jiří Houška, and Dr. Radomír Čerstvý for their contribution and advice in my research work. I am very grateful to Prof. Jaroslav Vlček, for his emotional support and motivation.

In the end, I would like to thank my family and friends for their incessant love and support throughout my life.

Abstract

This Ph.D. thesis reports on the research and development of new materials to be used for thin films-based hydrogen gas sensors and on subsequent investigation of their hydrogen gas sensing properties. For this purpose, the tungsten oxide-based thin films were combined with other materials in order to improve the sensing properties of the tungsten oxide thin films. This thesis contains a general introduction that describes the basic sensing principles of tungsten oxide-based sensors. Then an overview of the possible strategies for improvement is given. Several of these strategies are used and described in detail in the following chapters. One chapter is also dedicated to an overview of the techniques used to synthesize the materials, which are various sputtering deposition techniques. Also, the method of testing the sensing behavior that was developed as a part of my Ph.D. thesis is described in detail.

The first presented approach deals with the topic of nanostructuralization of the sensor surface. High-purity CuO nanoparticles were deposited using a gas aggregation-based cluster source (GAS) and added on top of the surface of tungsten oxide films. The sensing response was changing with the varying density of the CuO nanoclusters. The sensing response was significantly enhanced with the increasing density of the nanoclusters on the WO_3 film due to the formation of nano-sized PN junctions at the CuO/WO_3 interface.

In the second applied strategy, the formation of $CuWO_4$ nanoislands on the top of sub-stoichiometric tungsten oxide (WO_{3-x}) films was studied using a two-step deposition process. The WO_{3-x} deposited by reactive DC magnetron sputtering was followed by CuO deposition by RF sputtering deposition. This resulted in the formation of $CuWO_4$ nanoislands over the WO_{3-x}. The $CuWO_4/WO_{3-x}$ system was studied for hydrogen gas detection. The sensing response of the combined films was much higher than that of the individual CuO and WO_{3-x} films. The sensing mechanism based on the formation of the NN junction between $CuWO_4$ and WO_{3-x} is described.

Following the second strategy, the order of the CuO and WO_{3-x} deposition processes was reversed. The synthesized $CuWO_4$/CuO system was studied for hydrogen gas detection. The trend for the sensing response was similar to the $CuWO_4/WO_{3-x}$ system in dry air. The sensing response specifically for $CuWO_4$/CuO system was studied in dry and humid air, and it was found that the response was reduced dramatically in the humid air. To overcome or reduce the influence of humidity, the $CuWO_4$/CuO bilayers were overlayered by Pd thin films, deposited by RF sputtering. During the after-deposition treatment at 200°C, Pd was transformed into a form of Pd nanoparticles and PdO nano-sized islands. The value of the sensing response for the Pd/$CuWO_4$/CuO multi-layer was then equalized in dry and humid environments and at the same time, the sensors responded at lower temperatures. The formation of multiple junctions, *i.e., the* NN junction at the PdO / $CuWO_4$ and the PN junction at the $CuWO_4$ / CuO interfaces, remarkably improved the response and reduced the influence of humidity.

In the last described strategy, the structure and composition of the WO_{3-x} films were tuned by varying the deposition parameters of the HiPIMS (High-Power Impulse Magnetron Sputtering) technique. These were the oxygen partial pressure, voltage pulse length, and average power density. In addition to the experiments, the reactive HiPIMS model combined with the plasma

discharge model was used successfully to understand the effect of the discharge parameters on the structure and stoichiometry of the WO_{3-x} films. Owing to this model, WO_{3-x} could be synthesized with various stoichiometries and structures using HiPIMS with varying voltage pulse lengths. The varied stoichiometry, *i.e.*, various concentrations of oxygen vacancies, has a significant impact on the sensing response towards hydrogen. In addition, the sensing response for hydrogen gas for the monoclinic phase was found to be superior to those of the other crystalline phases.

Resumé

Tato disertační práce se zabývá výzkumem a vývojem nových materiálů pro přípravu a následné testování tenkovrstvých senzorů vodíku. Tenké vrstvy na bázi oxidu wolframu byly kombinovány s dalšími materiály za účelem zlepšení senzorického chování materiálu. Práce obsahuje obecný úvod popisující základní principy senzorů na bázi oxidu wolframu. Dále je uveden přehled strategií, kterými je možné vylepšovat základní senzorické vlastnosti oxidického materiálu. Několik z těchto strategií bylo použito a je podrobně popsáno v jednotlivých kapitolách. Samostatná kapitola je rovněž věnována přehledu depozičních technik, které byly použity pro přípravu zkoumaných materiálů. Zároveň je v této kapitole popsána metodika testování připravených senzorů, která byla během řešení práce dále zdokonalena.

První uplatněnou strategií pro zlepšení senzorického chování vrstev oxidu wolframu je kombinace vrstev s nanostrukturami oxidu měďnatého. Konkrétně se jedná o nanočástice CuO deponované pomocí zdroje klastrů založeného na agregaci plynů (GAS). Tyto nanočástice byly deponovány na povrch wolframoxidové (WO_3) vrstvy a následně byl zkoumán vliv různého množství nanočástic CuO na senzorické vlastnosti. S rostoucí hustotou nanoklastrů na povrchu vrstvy WO_3 se výrazně zvýšila senzorická odezva, což je vysvětleno vznikem nano-PN přechodů na rozhraní CuO/WO_3.

V rámci druhé strategie byla studována tvorba nanoostrůvků $CuWO_4$ na souvislé vrstvě oxidu wolframu pomocí dvoustupňového procesu depozice. Substechiometrický oxid wolframu (WO_{3-x}) byl deponován reaktivním DC magnetronovým naprašováním a následně byla nanesena vrstva CuO pomocí RF naprašování. Tento postup vedl k vytvoření strukturovaného $CuWO_4$. Následně byla testována citlivost systému $CuWO_4/WO_{3-x}$ na plynný vodík. Senzorická odezva této kombinace byla mnohem vyšší než u samostatných vrstev CuO či WO_{3-x}. V tomto případě stojí za zlepšením odezvy vznik NN heteropřechodů mezi $CuWO_4$ a WO_{3-x}.

V navazující kapitole jsou popsány výsledky studie, kdy bylo zaměněno pořadí depozičních procesů pro vrstvy CuO a WO_{3-x} a je zde zkoumán výsledný systém $CuWO_4/CuO$. Z výsledků vyplývá, že trend odezvy na plynný vodík je podobný jako u systému $CuWO_4/WO_{3-x}$, nicméně zde byla odezva navíc studována v syntetickém vzduchu s proměnnou vlhkostí. Bylo potvrzeno, že ve vlhkém vzduchu se odezva dramaticky snižuje. Pro korekci vlivu vlhkosti byly dvojvrstvy $CuWO_4/CuO$ doplněny tenkými vrstvami paladia nanesenými pomocí RF naprašování. Při následné stabilizaci při teplotě 200 °C se deponované paladium přemění jednak na nanočástice a jednak na ostrůvky oxidu paladia. Díky této komplexní struktuře je senzorická odezva u vícevrstev $PdO/CuWO_4/CuO$ vyrovnaná v suchém i vlhkém vzduchu, navíc systém pracuje při nižší teplotě.

V poslední popsané a uplatněné strategii byla struktura a složení vrstev WO_{3-x} zkoumány v závislosti na změně depozičních parametrů metodou reaktivního HiPIMS (vysokovýkonová pulzní magnetronová depozice). Byl zkoumán vliv změny parciálního tlaku kyslíku, délky napěťového pulsu a průměrné hustoty výkonu. Experimenty byly doplněny o model plazmového výboje, který umožnil lepší pochopení vlivu parametrů výboje na strukturu

a složení (stechiometrii) WO_{3-x} vrstev. Různá stechiometrie, tedy množství kyslíkových vakancí, se ukázala jako významný parametr ovlivňující senzorickou odezvu, přičemž množství vakancí bylo možné řídit změnou délky napěťového pulsu. Nadto bylo prokázáno, že krystalická struktura ovlivňuje citlivost vrstev. Konkrétně u monoklinické fáze je odezva lepší než u ostatních připravených krystalických fází.

Contents

1 Introduction

Rapid growth of energy consumption of human society due to both economic and population growth demands more accessible and efficient energy resources. Moreover, an exponential reduction in fossil fuel reserves due to the overutilization of coal and petroleum products and environmental consequences made it necessary to develop clean and green sources of energy. Hydrogen is a prominent candidate which fits best into such requirements due to its efficient and renewable essence. Hydrogen is an inspiring and motivating candidate in itself for the research because of its unique properties as a clean and green source of energy. It can be obtained from water and, at the same time, produces water as a by-product after combustion. H_2 is widely used as fuel in chemical industries, fuel cells, space crafts, and rockets. Although, H_2 is extremely dangerous because it has a wide explosive concentration, low ignition energy, and large propagation velocity. In addition, its tasteless, odorless, and colorless essence make it impossible to detect by the human senses. Taking the extreme importance of hydrogen and its undetectable and explosive nature into account, it has become necessary to develop materials for hydrogen gas detection for the purpose of safety. The materials developed for hydrogen detection are discussed in this chapter along with a brief introduction to relevant concepts and some fundamental information of gas sensors and their types, importance of hydrogen, and the materials, mainly metal oxides (WO_3, CuO, $CuWO_4$, and PdO). Furthermore, the most common techniques implemented to synthesize metal oxide semiconductors are explained in the thesis, followed by challenges and strategies to improve the performance of gas sensors. Subsequently, the objective and structure of the thesis are presented.

1.1 Structure of the Thesis

The thesis deals with the preparation of conductometric gas sensors based on nanostructured thin films of tungsten oxide modified with several other materials. The results are presented in the form of manuscripts *describing the combination of CuO, $CuWO_4$, and Pd/PdO with WO_3 films*.

The motivation for choosing tungsten oxide (WO_3) and the other materials, as well as the choice of sputtering deposition technique, is described in individual sections later. Since the work was closely connected to the construction and enhancing of the testing experimental setup and workflow, there is an individual Chapter 2 dedicated to methodology. The thesis is organized as follows:

Chapter 1 introduces the fundamental knowledge of the sensors, types of sensors, the importance of hydrogen gas detection, and sensing mechanism for WO_3 towards hydrogen gas, which is similar to that of any N-type metal oxide semiconductor for any reducing gas. Several strategies have been discussed extensively to improve the performance of sensors and various influencing parameters. This key discussion can be found in Section 1.6 on page 6.

Chapter 2 describes the synthesis of the nanostructured materials. The sputtering systems used to prepare WO_3 and CuO thin films, and CuO nanoclusters are described in detail. The characterization techniques are also described briefly in this chapter. It also illustrates the design and development of a custom-built sensitivity measurement system. The principle of operation and utilization of various techniques are discussed in detail.

Chapter 3 presents the objective of the thesis. The main tasks that are the backbone of this research for the motivation of the thesis are presented.

Chapter 4 reports the results in the form of published articles. Various approaches have been implemented to enhance the sensing performance of WO_3-based sensors towards hydrogen gas. The chapter is organized into five sections as A, B, C, D, and E on the basis of different strategies which are discussed in chapter 1. The mechanism behind the improvement of sensor performance is discussed in individual sections in this introductory chapter 1 as well as in individual manuscripts.

Chapter 5 presents the summary and conclusion of the work carried out during the Ph.D. study. This chapter also describes the fulfillment of the objective of the thesis. A brief comparison of the results obtained from the various approaches is also summarized.

1.2 Gas Sensors

The gas sensors, as the name suggests, provide information about any change in their intrinsic properties such as optical band gap, electric resistance, carrier concentration, etc. on interacting with any external analyte (CO, H_2, SO_2, NO_2. As the name suggests, the gas sensors provide information about any change in their intrinsic properties such as optical band gap, electric resistance, carrier concentration, etc. on interacting with any external analyte (CO, H2, SO2, NO_2 ethanol, etc. and explosive gases during the production, manufacturing, and transportation process of the products in industries. They are widely used in chemical and petrochemical industries, hospitals, medical institutions, food and drinks processing, environmental, scientific, and engineering research organizations, and many more industrial applications [1]–[3]. The gas sensors have an important role not only in industry and but also in agriculture and domestic uses to maintain air quality, fragrance, and humidity control. Gas sensors can be used to monitor harmful gases both indoors and outdoors. In environmental aspects, these sensors are used to control air pollution from automobile exhaust gases [4].

There are various types of Gas sensing technologies characterized according to their operational mechanism. Some of them are considered most suitable and intuitive and used to detect harmful gases, which are: Electrochemical gas sensors, Optical gas sensors, Electrical gas sensors, Catalytic Bead sensors, Infrared gas sensors, Acoustic-based sensors, etc. [5]. Description of the most common types follows.

Electrochemical gas sensors are mainly resistive types such as conductometric and potentiometric, which work on the mechanism of charge transfer within the electrodes on the interaction with electroactive species, which include the chemical recognition processes. They specifically measure the concentration by either reducing or oxidizing the target gas on the electrodes. They mainly detect the change in current flow, voltage, and capacitance of the materials due to the interaction of the target gas with the sensing material [1], [6]–[8].

Optical gas sensors operate on optical phenomena which include changes in absorption, reflectance and luminescence spectra, refractive index, optothermal effect, and light scattering. Most of the optical gas sensors detect changes in visible light during the interaction with the chemicals. Optical absorption, chemiluminescence, and fluorescence are quite common techniques employed for optical gas sensors. For example, the absorption characteristics of the target molecule can provide information of the target gas concentration by detecting the intensity of photon radiation that arrives to the sensor [9]–[12].

Electrical type gas sensors work on the mechanism of surface interaction with the target gas. They cover a large group of gas sensors such as polymer, semiconductor, metal, metal oxides conductometric sensors, capacitance sensors, Schottky-barrier, MOS, and FET-based sensors. They mainly measure the resistivity (conductivity) of the sensing material changes by the reaction that takes place between the target gas and the surface material layer [13]–[17].

Gas sensors are developed to provide information on any chemical composition of their surrounding environment. Therefore, an ideal gas sensor should work continuously, and it should be selected for any specific gas, it should be economic, and must have a quick response and recovery time. Portability, low power requirements, explosion-proof housing, and quantitative reliability are also useful requirements for the best gas sensor. However, it is challenging to fabricate a gas sensor with all these characteristics. Researchers are still trying to fabricate such gas sensors for the power production industries.

1.3 Importance of H_2 Detection

Among the demand and importance of the detection of toxic, polluted, and flammable gases, hydrogen detection is also important to consider as hydrogen is a clean, renewable, efficient, and reliable source of energy for the future. It is the best candidate source for replacing fossil fuels because it can reduce carbon dioxide emissions by 20% in the industry. The byproduct is just water rather than any other harmful gas produced by industries and automobiles. Apart from being a source of energy, Hydrogen has vast applications. Liquid hydrogen is used as fuel for aircraft and rockets. Moreover, because of its reducing properties, it is also used in metal smelting, glassmaking, steel industries, semiconductor processing, petroleum extraction, and the daily chemical industry. Additionally, it can be applied in environmental protection, biomedical applications, an indication of certain bacterial infections, etc. Being such a prominent source of energy, it is difficult to control and store hydrogen due to its explosive nature. For the sake of safety, it becomes more important to develop the H_2 gas sensor to detect the low concentration of H_2 during storage, transport, and domestic uses [18]–[20]. The rapidly growing hydrogen industry requires the development of new hydrogen gas sensors for the purpose of safety during the process of production, storage, transportation, and domestic use of hydrogen-based fuel cells. Hydrogen is a clean, green, and reliable source of energy and has some unusual properties, such as low boiling point (20.39 K), highly diffusive (diffusion coefficient is 0.61 cm^2/s), low ignition energy (0.02 mJ), high combustion heat (142 kJ/g H_2), wide inflammable range (4-75%) and high combustion velocity. Hydrogen is colorless, odorless, and tasteless, making it almost impossible to detect by ordinary human senses [18], [20], [21].

The aforementioned characteristics of hydrogen gas require special precautions in certain applications. Rapid and precise H_2 gas concentration measurement is necessary to detect during the production, storage, and use of hydrogen to alert about the leakage and prevent the risk of formation of explosive mixture with air. However, hydrogen sensors have been studied for many decades but there is a continued need for faster, selective, and more accurate detection of hydrogen gas in various industrial fields for monitoring and controlling hydrogen concentration. For example, monitoring of hydrogen concentration is essential in the synthesis of ammonia, nuclear reactor safety, hydration of hydrocarbons, desulphurization of petrochemical products, welding, and galvanic plating.

There are various methods to detect hydrogen, which employ instruments like mass spectrometers, chromatography, or/and specific ionization gas pressure. Each of them has a different sensing mechanism for the detection of a target gas. These traditional hydrogen sensors are limited by their large size, slow response and recovery time, high cost of fabrication, and high-power requirements. Whereas, the sensors need to have a small size, fast response and recovery time, low operating temperatures, low cost, and selectivity too. To fulfill the requirements of modern industrial technologies, researchers need to develop materials for an efficient gas sensor.

1.4 Materials for Hydrogen Sensors

Numerous materials have been studied and are still being studied to design hydrogen gas sensors. Hydrogen gas sensors based on metals, metal-oxide semiconductors, covalent semiconductors, solid electrolytes, organic semiconductors, polymers, graphene, MXenes, and other 2D materials have been studied [22]–[24]. Recently, these materials might be used as semiconductor, electrochemical, thermoelectrical, metallic, optical, and acoustic sensors. Among all of them, semiconductor-based sensors are highly sensitive, stable, and exhibit a fast response time. In recent works, several nanostructures, and types of semiconductors have been studied to design suitable hydrogen sensors such as metal-oxide semiconductors (MOS), organic semiconductors, and covalent semiconductors.

Metal-oxide semiconductors, mainly binary and ternary oxides, with a wide range of bandgaps, have been used to design hydrogen gas sensors. Medium bandgap materials such as SnO_2, CeO_2, Ta_2O_5, ZnO, and In_2O_3, materials with narrow bandgap like CuO, $ZnWO_4$ $CuWO_4$, Cr_2O_3, and V_2O_5, and wide bandgap materials, such as HfO_2 and ZrO_2 have been studied for gas detection. Among these MOS, WO_3 is a promising candidate for gas sensing applications. Apart from sensing application WO_3 has a wide range of applications in electrochromic materials [25], photochromic materials [26], photocatalysis [27], battery electrodes [28], thermoelectric devices [29], solar cells electrodes [30], superconductors [31], and electrochemical cell [32] because of its unique physical and chemical properties.

WO_3 exhibits different forms of crystal structures at different temperatures. The phase stability of WO_3 is as follows: monoclinic (ε-WO_3) below –43 °C, triclinic (δ-WO_3) in range of –43 °C to 330 °C, orthorhombic (β-WO_3) from 330 °C to 740 °C and tetragonal (α-WO_3) above 740 °C. The bandgap in WO_3 varies in the range of 2.6 eV to 3.3 eV from crystalline to amorphous form [33], respectively which is suitable for the application of gas sensing. It is an N-type semiconductor in which free electrons are generated due to oxygen vacancies [34]. The

morphology, stoichiometry, and structure of WO_3 can easily be controlled by various preparation techniques. Sensitivity can be improved by changing the baseline resistance of the WO_3 films by controlling the microstructures and stoichiometry [35]–[37]. WO_3 possesses high sensitivity and selectivity for a wide variety of gases, both oxidizing and reducing [38], [39]. WO_3 is considered a potential candidate because interaction with hydrogen leads to a change in its electrical resistance by several orders of magnitude [40].

1.5 Sensing Mechanism

The fundamental mechanisms known for the detection of the reducing gases are applied to hydrogen gas as well. When WO_3 is exposed to air, oxygen molecules chemisorb on the surface of WO_3 and create an electron depletion channel by drawing electrons from the conduction band. Furthermore, the evolution of reactive oxygen species such as O^-, and O^{2-}, O_2^- takes place on the surface at certain temperatures. Many researchers have studied the stability and contribution of different oxygen species in the sensing mechanisms at different temperatures [41]. The stability temperature of the various oxygen species is shown in Table 1. The surface adsorbed oxygen species then react with the target gas (H_2) and donate the trapped electrons back to the sensing layer, which narrowed the space charge region and leads to a change in resistance as illustrated in Figure 1.1. A couple of additional small physical effects can be introduced to the fundamental mechanism to enhance the sensing response by tempering the pure WO_3 film with other phenomena discussed in the following section. There are several definitions used for the WO_3 sensor response S, but the most common is

$$S(t) = \frac{R_a}{R_g} \tag{1}$$

to reduce gas. R_a denotes the value of electric resistance in synthetic air and R_g represents the resistance value in the presence of the target gas. Sometimes, the sensing response is also defined as:

$$S(t) = \frac{R_a - R_g}{R_g} \tag{2}$$

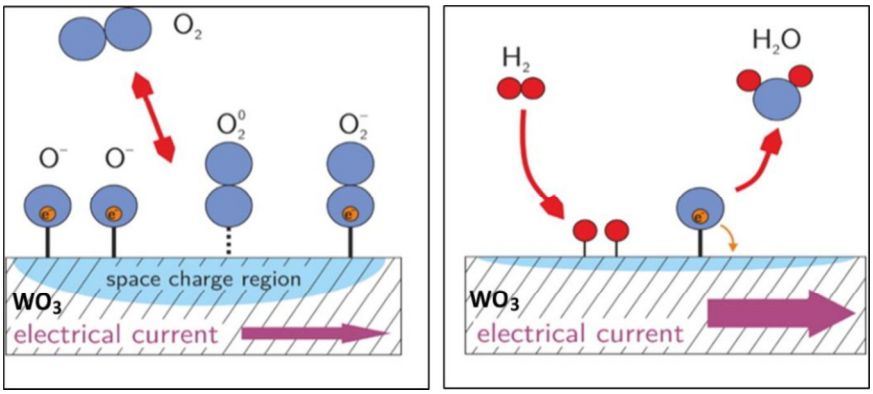

Figure 1.1. Fundamental sensing mechanism of the WO_3 film towards hydrogen gas.

Table 1 Dominant adsorbed oxygen species on the surface of WO_3

Oxygen Species	Stability Temperature (°C)
O^-	300–450
O^{2-}	> 350
O_2^-	RT–150
O_2	50–100

1.6 Challenges and Strategies

It is quite challenging to fabricate an ideal gas sensor. On the basis of the research done so far, there are some important parameters that are quite challenging to achieve. A gas sensor should exhibit

i. high sensitivity
ii. fast response and recovery time
iii. Selective towards a particular gas
iv. low working temperature (nearly room temperature)
v. stability
vi. zero or very low influence of humidity or other relevant accompanying gases for the application.

To deal with these challenges, various strategies and approaches have been developed during the last couple of decades [18], [20], [42]. Some of them are briefly discussed in this thesis. The strategies which have been adopted to develop the metal-oxide semiconductor are as follows.

a) Materials Selection

A large number of MOS have been investigated in the past century. Several N-type binary and ternary oxides with the band gap in the range of 2 to 4 eV such as SnO_2, TiO_2, ZnO, Ta_2O_5, Ga_2O_3, WO_3, $CuWO_4$, etc. are studied [43], [44]. In P-type MOS, CuO, NiO, Co_3O_4, and PdO are widely investigated [45]. Perovskite oxides such as $BaTiO_3$, $SrTiO_3$, and $LaFeO_3$, which also exhibit P-type behavior, are also studied to develop better gas sensors [42]. Graphene and other 2D materials such as h-BN, GaAs, MoS_2, MXenes, etc. are emerging and trending materials for gas detection along with their wide range of applications [46]–[49]. In this work, we particularly focused on WO_3 due to its unique properties and suitable band gap as described in the previous section. WO_3 is combined with various metals or MOS such as Pd, CuO, $CuWO_4$, and PdO to improve the sensing response of WO_3 towards hydrogen gas.

b) Doping

Most of the MOS-based sensors work on the phenomenon of adsorption and desorption of the target gas at the surface of the material. These sensors can be activated at higher temperatures which consume more power [50]. To overcome the issue, many efforts have been put into reducing the operating temperature. Amongst all the efforts, metal doping is a common way to modify the electronic structure due to impurity levels in the bandgap of the metal oxide to

improve the performance towards various applications including gas sensing [51], [52]. Investigation of transition-metal-doped ZnO in order to improve the sensitivity is quite common [53], [54]. Several researchers doped WO_3 with other metals such as In, Fe, Pd, and Ag to improve sensor performance and lower working temperature [55]–[57].

c) Porous Films

Porous MOS films are very attractive from the point of view of the sensors due to their unique crystalline structure, which provides a large surface for the enhancement of the effects of adsorbate and high activity in chemical reactions at the surface [58], [59]. A desirable change can be seen in electrical and optical characteristics of the porous MOS upon adsorption of molecules by filling the pores at the surface. In this case, the 'capillary condensation effect' also contributes along with the surface adsorption effect to improve sensor performance [60], [61]. Several porous MOS have been studied to enhance sensitivity and reduce the influence of humidity [62]–[64]. Porous WO_3 films are found very promising to enhance sensitivity, selectivity toward NO gas [65], [66].

d) Nanostructures

The nanostructures exhibit mechanical, optical, electrical, and magnetic properties different from those of the bulk state. An enormous variation in the electric properties of an oxide artifact can be noticed by moving towards nano dimensions. This does limit the conductivity trapped to the surface because at least one dimension is lesser than the depletion depth [42]. Nanostructures have a high surface over volume ratio. High surface area is desirable credit for the MOS sensors. Recently, the production of nanostructured MOS by adapting various preparation techniques for conductometric sensors is quite popular. MOS can be produced as nanoparticles (0D), nanowires, nanorods and nanotubes (1D), and nanosheets (2D) with high surface area [67]–[71]. The strategy has been pursued in the research work and the results are shown in Chapters 4 Sections A, B, and E.

e) Noble Metal Decoration

Introducing additive material (oxide or metallic form) on the surface of the sensing materials significantly enhances the sensitivity, lowers the operating temperature, and fastens the response and recovery time. The selective metals with high work functions (Pd, Pt, Au, Rh, etc.) are used to cover some portion of the surface of the sensing materials. Their high work function leads to the formation of the Schottky barrier at the metal/oxide interface, which increases the baseline resistance of the sensing material. The aforementioned precious metals exhibit catalytic characteristics which shift the working temperature to the lower values as reported in the literature [42], [72]–[74]. Furthermore, the most important contribution of the additive metal is to reduce the interference of relative humidity in the sensing mechanism. This approach has been successfully implemented in this thesis to improve the performance of the sensors and results are presented in Chapter 4 Sections C and E of the thesis.

f) PN-type Heterojunction

In this approach, N-type, and P-type MOS are placed in contact with each other for gas sensing. There might be two configurations depending on the selection of the backbone material and the functionalized material. If a P-type backbone material will provide a dominant conduction path functionalized by N-type MOS it would be called P-N junction and N-P junction when N-type MOS is selected as backbone material and P-type as functionalized material [71]. Charge carriers transfer from the functionalized material to the backbone materials at the junction, which results in thickening of the depletion layer which changes the resistance of the backbone material. Several studies successfully investigated these effects in a combination with materials such as ZnO/CuO, PdO/WO_3, SnO_2/CuO, Pyrrole/WO_3, etc. [75]–[77]. This approach is presented in Chapter 4 Section A.

g) NN-type Heterojunction

The depletion region of an N-type MOS can also be modified by combining with another N-type MOS. In this case, electrons then transfer from a higher energy conduction band to the lower energy conduction band and form an 'accumulation layer' at the interface rather than a depletion layer in the cases of PN-type heterojunction. Oxygen adsorption during the sensing process can deplete the accumulation layer and change the resistance of the backbone material to enhance sensitivity. Such strategies have been successfully employed to improve sensor performance by combining SnO_2/ZnO, SnO_2/WO_3, ZnO/WO_3, WO_3/MoO_3, etc. [78]–[81]. We used this approach in Chapter Section B.

h) Oxygen Vacancies

Recently, it has been observed that oxygen vacancies play an important role in the mechanism of gas sensing for MOS-based sensors. Varying the oxygen vacancies is an alternative approach to improve the sensor's performance. Oxygen vacancies directly affect oxygen absorption on the surface of the material and facilitate ionosorption to improve performance and lower operating temperature [82]. As the sensing mechanism states, the target gas needs adsorbed oxygen species at the surface for the interactions. The adsorption and activation of the target gas can be affected by the oxygen vacancies, mainly vacancies that might donate electrons to form more chemisorbed oxygen species [83]. It has been reported that sub-stoichiometric WO_{3-x} provided a successful scope of improving the gas sensing by varying oxygen vacancies; see Chapter 4 Section E. However, it is challenging to have control over oxygen vacancies, but there are possible ways to prepare sub-stoichiometric metal oxide materials [82]–[86]. The oxygen defects can change the coordination number of the neighboring atoms, which tune the active species of reactive sites, consequently, the sensing [87].

1.7 Material Synthesis

There are a vast number of methods and techniques for preparing the material either in the form of bulk, thick films, thin films, or nanostructures. There are thousands of ways to prepare the MOS material from the PVD, CVD, Thermal oxidation, wet chemical techniques, etc. and each has its own features, and every method has its limitations as well, for example, it is still challenging to control chemical composition, surface morphology, reproducibility, and

crystalline phase of the nanostructure's synthesis using thin-film technology methods. The most common wet techniques, such as sol-gel, hydrothermal, and precipitation synthesis, are used to provide films with high surface area, porosity, and fixed stoichiometry. The problems of these techniques are worse integrability with microcircuit fabrication, tuning of stoichiometry, and a limited range of accessible compositions.

These challenges are possible to address with PVD techniques such as Sputtering, Pulsed Laser Deposition, Thermal Evaporation, Molecular beam Epitaxy, and many more allow precise control of the stoichiometry, crystallite size, structure, and crystalline phases. All of the above-mentioned techniques have been used to synthesize thin films, porous thick films, and nanocomposites such as nanowires, nanorods, nanoflowers, etc. for the gas-sensing application. Multiple synthesis methods are investigated to tune the morphology, structure, and stoichiometry of the MOS to improve the sensing performance [1], [71], [88]–[90].

Sputtering deposition is a favored technique because it can be used to deposit a large variety of materials. The prominent feature of sputtering is that it can be used to deposit metals, insulators, semiconductors, etc. The palette of materials is wide; multiple elements can be easily combined including tuning of the stoichiometry of oxides. Importantly, it is compatible with microcircuit fabrication processes. Last but not least, it is a scalable technique, being used for large area coatings.

Sputtering is a plasma-based physical process in which the atoms or molecules are released from the surface of the target as a result of the bombardment of gas ions on the target, and these atoms/molecules then deposit on the substrate. It is a process of collision between the target and incident ions. In the case of magnetron sputtering, efficiency is enlarged by the employment of a magnetic field which bounds the secondary electrons to a specific target surface area and promotes ionization efficiency. This leads to an increment of the ion density and therefore sputtering rate. Magnetron sputtering is a useful technique for growing high-purity films at low temperatures and low cost.

Sputtering can be utilized in various power modes such as DC, RF, HiPIMS, Pulsed DC, etc. Each works on a slightly different principle. Oxide and nitride films can easily be deposited by reactive sputtering using oxygen or nitrogen as a reactive gas [91]–[93]. Various researchers have been investigated the properties of MOS films prepared by magnetron sputtering [94]–[98]. The structure of metal oxide films can be easily controlled by the sputtering technique. The structure can be tuned from amorphous through nanocrystalline to well-crystalline by varying the deposition parameters such as target power density, duty cycle, voltage pulse length, etc. [99] [100]. Control over deposition rate provides a controlled thickness and uniform film by various modes of the sputtering technique [98], [101]

In this work, we employed the DC reactive magnetron sputtering and HiPIMS to deposit WO_{3-x} from a tungsten metal target which is described in Chapter 4 Sections A–E, and RF reactive sputtering for the deposition of CuO, and Pd by Cu and Pd metallic target, respectively, as described in Chapter Sections B, and C. DC magnetron sputtering is employed to deposit Cu nanoclusters which are naturally oxidized (Chapter 4 Section A).

1.8 References

[1] G. Korotcenkov, S. do Han, and J. R. Stetter, "Review of electrochemical hydrogen sensors," *Chemical Reviews*, vol. 109, no. 3. Pp. 1402 1433, Mar. 11, 2009. Doi: 10.1021/cr800339k.

[2] G. Korotcenkov, "Integrated Analytical Systems Series Editor: Radislav A. Potyrailo Handbook of Gas Sensor Materials." [Online]. Available: http://www.springer.com/series/7427

[3] S. Capone *et al.*, "SOLID STATE GAS SENSORS: STATE OF THE ART AND FUTURE ACTIVITIES," 2003.

[4] A. D. Wilson and M. Baietto, "Applications and advances in electronic-nose technologies," *Sensors*, vol. 9, no. 7. Pp. 5099–5148, Jul. 2009. Doi: 10.3390/s90705099.

[5] R. Jaaniso and O. K. Tan, *Semiconductor gas sensors*.

[6] S. Neethirajan, D. S. Jayas, and S. Sadistap, "Carbon dioxide (CO 2) sensors for the agri-food industry-A review," *Food and Bioprocess Technology*, vol. 2, no. 2. Pp. 115–121, 2009. Doi: 10.1007/s11947-008-0154-y.

[7] J. Zosel, W. Oelner, M. Decker, G. Gerlach, and U. Guth, "The measurement of dissolved and gaseous carbon dioxide concentration," *Measurement Science and Technology*, vol. 22, no. 7. Institute of Physics Publishing, 2011. Doi: 10.1088/0957-0233/22/7/072001.

[8] A. M. Azevedo, D. M. F. Prazeres, J. M. S. Cabral, and L. P. Fonseca, "Ethanol biosensors based on alcohol oxidase," *Biosensors and Bioelectronics*, vol. 21, no. 2. Pp. 235–247, Aug. 15, 2005. Doi: 10.1016/j.bios.2004.09.030.

[9] O. S. Wolfbeis, "Fiber-optic chemical sensors and biosensors," *Analytical Chemistry*, vol. 78, no. 12. Pp. 3859–3873, Jun. 15, 2006. Doi: 10.1021/ac060490z.

[10] X. D. Wang and O. S. Wolfbeis, "Optical methods for sensing and imaging oxygen: Materials, spectroscopies and applications," *Chemical Society Reviews*, vol. 43, no. 10. Royal Society of Chemistry, pp. 3666–3761, May 21, 2014. Doi: 10.1039/c4cs00039k.

[11] C. Ast, E. Schmälzlin, H. G. Löhmannsröben, and J. T. van Dongen, "Optical oxygen micro- and nanosensors for plant applications," *Sensors (Switzerland)*, vol. 12, no. 6. Pp. 7015–7032, Jun. 2012. Doi: 10.3390/s120607015.

[12] J. Shemshad, S. M. Aminossadati, and M. S. Kizil, "A review of developments in near infrared methane detection based on tunable diode laser," *Sensors and Actuators, B: Chemical*, vol. 171–172. Pp. 77–92, Aug. 2012. Doi: 10.1016/j.snb.2012.06.018.

[13] T. Sakuma, "OVERVIEW Phase Transformation and Microstructure of Partially-Stabilized Zirconia*," 1988.

[14] B. Podlepetsky, M. Nikiforova, and A. Kovalenko, "Chip temperature influence on characteristics of MISFET hydrogen sensors," *Sensors and Actuators, B: Chemical*, vol. 254, pp. 1200–1205, Jan. 2018, doi: 10.1016/j.snb.2017.07.156.

[15] C. H. Chang, K. W. Lin, H. H. Lu, R. C. Liu, and W. C. Liu, "Hydrogen sensing performance of a Pd/HfO2/GaOx/GaN based metal-oxide-semiconductor type Schottky diode," *International Journal of Hydrogen Energy*, vol. 43, no. 42, pp. 19816–19824, Oct. 2018, doi: 10.1016/j.ijhydene.2018.08.213.

[16] A. Boudiba, P. Roussel, C. Zhang, M. G. Olivier, R. Snyders, and M. Debliquy, "Sensing mechanism of hydrogen sensors based on palladium-loaded tungsten oxide (Pd-WO_3)," *Sensors and Actuators, B: Chemical*, vol. 187, pp. 84–93, 2013, doi: 10.1016/j.snb.2012.09.063.

[17] W. Maziarz, "TiO 2 /SnO 2 and TiO 2 /CuO thin film nano-heterostructures as gas sensors," *Applied Surface Science*, vol. 480, pp. 361–370, Jun. 2019, doi: 10.1016/j.apsusc.2019.02.139.

[18] T. Hübert, L. Boon-Brett, G. Black, and U. Banach, "Hydrogen sensors – A review," *Sensors and Actuators, B: Chemical*, vol. 157, no. 2. Pp. 329–352, Oct. 20, 2011. Doi: 10.1016/j.snb.2011.04.070.

[19] G. Meng, C. Jiang, J. Ma, Q. Ma, and X. Liu, "Comparative study on the performance of a SDC-based SOFC fueled by ammonia and hydrogen," *Journal of Power Sources*, vol. 173, no. 1, pp. 189–193, Nov. 2007, doi: 10.1016/j.jpowsour.2007.05.002.

[20] S. Phanichphant, "Semiconductor Metal Oxides as Hydrogen Gas Sensors," in *Procedia Engineering*, 2014, vol. 87, pp. 795–802. Doi: 10.1016/j.proeng.2014.11.677.

[21] H. Gu, Z. Wang, and Y. Hu, "Hydrogen gas sensors based on semiconductor oxide nanostructures," *Sensors (Switzerland)*, vol. 12, no. 5. Pp. 5517–5550, May 2012. Doi: 10.3390/s120505517.

[22] I. Constantinoiu and C. Viespe, "Hydrogen detection with SAW polymer/quantum dots sensitive films," *Sensors (Switzerland)*, vol. 19, no. 20, Oct. 2019, doi: 10.3390/s19204481.

[23] S. A. Singh, P. S. More, Y. B. Khollam, and S. B. Kondawar, "Enhanced hydrogen gas sensing characteristics of graphene modified with rubidium (Rb)," *Materials Chemistry and Physics*, vol. 260, Feb. 2021, doi: 10.1016/j.matchemphys.2020.124105.

[24] S. Mehdi Aghaei, A. Aasi, and B. Panchapakesan, "Experimental and Theoretical Advances in Mxene-Based Gas Sensors," *ACS Omega*, vol. 6, no. 4. American Chemical Society, pp. 2450–2461, Feb. 02, 2021. Doi: 10.1021/acsomega.0c05766.

[25] V. R. Buch, A. K. Chawla, and S. K. Rawal, "Review on electrochromic property for WO_3 thin films using different deposition techniques," in *Materials Today: Proceedings*, 2016, vol. 3, no. 6, pp. 1429–1437. Doi: 10.1016/j.matpr.2016.04.025.

[26] S. Wang, W. Fan, Z. Liu, A. Yu, and X. Jiang, "Advances on tungsten oxide based photochromic materials: Strategies to improve their photochromic properties," *Journal of Materials Chemistry C*, vol. 6, no. 2. Royal Society of Chemistry, pp. 191–212, 2018. Doi: 10.1039/c7tc04189f.

[27] A. Fakhri and S. Behrouz, "Photocatalytic properties of tungsten trioxide (WO_3) nanoparticles for degradation of Lidocaine under visible and sunlight irradiation," *Solar Energy*, vol. 112, pp. 163–168, Feb. 2015, doi: 10.1016/j.solener.2014.11.014.

[28] X. Wu and S. Yao, "Flexible electrode materials based on WO_3 nanotube bundles for high performance energy storage devices," *Nano Energy*, vol. 42, pp. 143–150, Dec. 2017, doi: 10.1016/j.nanoen.2017.10.058.

[29] H. Wang, X. Dong, S. Peng, L. Dong, and Y. Wang, "Improvement of thermoelectric properties of WO 3 ceramics by ZnO addition," *Journal of Alloys and Compounds*, vol. 527, pp. 204–209, Jun. 2012, doi: 10.1016/j.jallcom.2012.03.022.

[30] K. Hara, Z. G. Zhao, Y. Cui, M. Miyauchi, M. Miyashita, and S. Mori, "Nanocrystalline electrodes based on nanoporous-walled WO_3 nanotubes for organic-dye-sensitized solar cells," *Langmuir*, vol. 27, no. 20, pp. 12730–12736, Oct. 2011, doi: 10.1021/la201639f.

[31] A. v. Palnichenko, O. M. Vyaselev, A. A. Mazilkin, I. I. Zver'kova, and S. S. Khasanov, "Metastable superconductivity of W/WO_3 interface," *Physica C: Superconductivity and its Applications*, vol. 534, pp. 61–67, Mar. 2017, doi: 10.1016/j.physc.2017.02.002.

[32] P. A. Shinde, A. C. Lokhande, A. M. Patil, and C. D. Lokhande, "Facile synthesis of self-assembled WO_3 nanorods for high-performance electrochemical capacitor," *Journal of Alloys and Compounds*, vol. 770, pp. 1130–1137, Jan. 2019, doi: 10.1016/j.jallcom.2018.08.194.

[33] R. A. Potyrailo, "Integrated Analytical Systems Series Editor." [Online]. Available: http://www.springer.com/series/7427

[34] W. Wang, A. Janotti, and C. G. van de Walle, "Role of oxygen vacancies in crystalline WO_3," *Journal of Materials Chemistry C*, vol. 4, no. 27, pp. 6641–6648, 2016, doi: 10.1039/c6tc01643j.

[35] M. D. Antonik, J. E. Schneider, E. L. Wittman, K. Snow, J. F. Vetelino, and R. J. Lad, "5764 Sm;ver Rrsrurclr Cwrer, Cgniwr.~i/y of' Maim," 1995.

[36] Z. Xu, J. F. Vetelino, R. Lec, and D. C. Parker, "Electrical properties of tungsten trioxide films," *Journal of Vacuum Science & Technology A: Vacuum, Surfaces, and Films*, vol. 8, no. 4, pp. 3634–3638, Jul. 1990, doi: 10.1116/1.576517.

[37] W. Noh *et al.*, "Effects of NiO addition in WO 3-based gas sensors prepared by thick film process." [Online]. Available: www.elsevier.com/locate/ssi

[38] R. Godbole, A. Vedpathak, V. Godbole, and S. Bhagwat, "Tungsten oxide thin films: Detection and trapping of hazardous gases," *Materials Research Express*, vol. 4, no. 7, Jul. 2017, doi: 10.1088/2053-1591/aa72a8.

[39] S. Haviar, Š. Chlupová, P. Kúš, M. Gillet, V. Matolín, and I. Matolínová, "Micro-contacted self-assembled tungsten oxide nanorods for hydrogen gas sensing," *International Journal of Hydrogen Energy*, vol. 42, no. 2, pp. 1344–1352, Jan. 2017, doi: 10.1016/j.ijhydene.2016.09.187.

[40] G. Mattoni, B. de Jong, N. Manca, M. Tomellini, and A. D. Caviglia, "Single-Crystal Pt-Decorated WO_3 Ultrathin Films: A Platform for Sub-ppm Hydrogen Sensing at Room Temperature," *ACS Applied Nano Materials*, vol. 1, no. 7, pp. 3446–3452, Jul. 2018, doi: 10.1021/acsanm.8b00627.

[41] "36. Barsan1999_Article_FundamentalAndPracticalAspects".

[42] P. T. Moseley, "Progress in the development of semiconducting metal oxide gas sensors: A review," *Measurement Science and Technology*, vol. 28, no. 8. Institute of Physics Publishing, Jun. 28, 2017. Doi: 10.1088/1361-6501/aa7443.

[43] S. B. Jagadale, V. L. Patil, S. A. Vanalakar, P. S. Patil, and H. P. Deshmukh, "Preparation, characterization of 1D ZnO nanorods and their gas sensing properties," *Ceramics International*, vol. 44, no. 3, pp. 3333–3340, 2018, doi: 10.1016/j.ceramint.2017.11.116.

[44] A. Trinchi, W. Wlodarski, and Y. X. Li, "Hydrogen sensitive GA2O3 Schottky diode sensor based on SiC," *Sensors and Actuators, B: Chemical*, vol. 100, no. 1–2, pp. 94–98, Jun. 2004, doi: 10.1016/j.snb.2003.12.028.

[45] H. J. Kim and J. H. Lee, "Highly sensitive and selective gas sensors using p-type oxide semiconductors: Overview," *Sensors and Actuators, B: Chemical*, vol. 192. Pp. 607–627, Mar. 01, 2014. Doi: 10.1016/j.snb.2013.11.005.

[46] K. Deshmukh, T. Kovářík, and S. K. Khadheer Pasha, "State of the art recent progress in two dimensional Mxenes based gas sensors and biosensors: A comprehensive review," *Coordination Chemistry Reviews*, vol. 424. Elsevier B.V., Dec. 01, 2020. Doi: 10.1016/j.ccr.2020.213514.

[47] Y. J. Zhang *et al.*, "Theoretical insights into the uranyl adsorption behavior on vanadium carbide Mxene," *Applied Surface Science*, vol. 426, pp. 572–578, Dec. 2017, doi: 10.1016/j.apsusc.2017.07.227.

[48] L. Zhang, K. Khan, J. Zou, H. Zhang, and Y. Li, "Recent Advances in Emerging 2D Material-Based Gas Sensors: Potential in Disease Diagnosis," *Advanced Materials Interfaces*, vol. 6, no. 22. Wiley-VCH Verlag, Nov. 01, 2019. Doi: 10.1002/admi.201901329.

[49] Q. Wang, "Simulations of the bending rigidity of graphene," *Physics Letters, Section A: General, Atomic and Solid State Physics*, vol. 374, no. 9, pp. 1180–1183, Feb. 2010, doi: 10.1016/j.physleta.2009.12.063.

[50] Y. Wang *et al.*, "Low-Temperature H2S Detection with Hierarchical Cr-Doped WO_3 Microspheres," *ACS Applied Materials and Interfaces*, vol. 8, no. 15, pp. 9674–9683, May 2016, doi: 10.1021/acsami.5b12857.

[51] Y. J. Choi, Z. Seeley, A. Bandyopadhyay, S. Bose, and S. A. Akbar, "Aluminum-doped TiO2 nano-powders for gas sensors," *Sensors and Actuators, B: Chemical*, vol. 124, no. 1, pp. 111–117, Jun. 2007, doi: 10.1016/j.snb.2006.12.005.

[52] M. C. Carotta *et al.*, "Nanostructured pure and Nb-doped TiO 2 as thick film gas sensors for environmental monitoring," 1999.

[53] A. P. Rambu, L. Ursu, N. Iftimie, V. Nica, M. Dobromir, and F. Iacomi, "Study on Ni-doped ZnO films as gas sensors," *Applied Surface Science*, vol. 280, pp. 598–604, Sep. 2013, doi: 10.1016/j.apsusc.2013.05.033.

[54] M. Hjiri, L. el Mir, S. G. Leonardi, A. Pistone, L. Mavilia, and G. Neri, "Al-doped ZnO for highly sensitive CO gas sensors," *Sensors and Actuators, B: Chemical*, vol. 196, pp. 413–420, Jun. 2014, doi: 10.1016/j.snb.2014.01.068.

[55] L. Chen and C. Tsang, "Ag doped WO 3-based powder sensor for the detection of NO gas in air."

[56] V. Khatko *et al.*, "Gas sensing properties of nanoparticle indium-doped WO_3 thick films," in *Sensors and Actuators, B: Chemical*, Nov. 2005, vol. 111–112, no. SUPPL., pp. 45–51. Doi: 10.1016/j.snb.2005.06.060.

[57] C. Piloto, M. Shafiei, H. Khan, B. Gupta, T. Tesfamichael, and N. Motta, "Sensing performance of reduced graphene oxide-Fe doped WO_3 hybrids to NO_2 and humidity at room temperature," *Applied Surface Science*, vol. 434, pp. 126–133, Mar. 2018, doi: 10.1016/j.apsusc.2017.10.152.

[58] G. Korotcenkov and B. K. Cho, "Porous semiconductors: Advanced material for gas sensor applications," *Critical Reviews in Solid State and Materials Sciences*, vol. 35, no. 1. Pp. 1–37, Jan. 2010. Doi: 10.1080/10408430903245369.

[59] M. Tiemann, "Porous metal oxides as gas sensors," *Chemistry – A European Journal*, vol. 13, no. 30, pp. 8376–8388, 2007, doi: 10.1002/chem.200700927.

[60] V. Parkhutik, "Porous siliconÐmechanisms of growth and applications."

[61] R. C. Anderson, R. S. Muller, C. W. Tobias, B. Sensor, and A. Center, "INVESTIGATION OF POROUS SILICON FOR VAPOR SENSING Investigations of Porous Silicon for Vapor Sensing."

[62] K. Iizuka, M. Kambara, and T. Yoshida, "Highly sensitive SnO 2 porous film gas sensors fabricated by plasma spray physical vapor deposition," *Sensors and Actuators, B: Chemical*, vol. 173, pp. 455–461, Oct. 2012, doi: 10.1016/j.snb.2012.07.060.

[63] C. Lee *et al.*, "Self-assembled monolayers coated porous SNO_2 film gas sensor with reduced humidity influence," *Sensors (Switzerland)*, vol. 21, no. 2, pp. 1–11, Jan. 2021, doi: 10.3390/s21020610.

[64] S. Abegg, D. K. Cerrejon, A. T. Güntner, and S. E. Pratsinis, "Thickness optimization of highly porous flame-aerosol deposited WO_3 films for NO_2 sensing at PPB," *Nanomaterials*, vol. 10, no. 6, pp. 1–15, Jun. 2020, doi: 10.3390/nano10061170.

[65] T. Kida, A. Nishiyama, Z. Hua, K. Suematsu, M. Yuasa, and K. Shimanoe, "WO_3 nanolamella gas sensor: Porosity control using SnO_2 nanoparticles for enhanced NO_2 sensing," *Langmuir*, vol. 30, no. 9, pp. 2571–2579, Mar. 2014, doi: 10.1021/la4049105.

[66] Z. Xie, Y. Zhu, J. Xu, H. Huang, D. Chen, and G. Shen, "Porous WO_3 with enhanced photocatalytic and selective gas sensing properties," *CrystEngComm*, vol. 13, no. 21, pp. 6393–6398, Nov. 2011, doi: 10.1039/c1ce05579h.

[67] C. Dong, R. Zhao, L. Yao, Y. Ran, X. Zhang, and Y. Wang, "A review on WO_3 based gas sensors: Morphology control and enhanced sensing properties," *Journal of Alloys and Compounds*, vol. 820. Elsevier Ltd, Apr. 15, 2020. Doi: 10.1016/j.jallcom.2019.153194.

[68] H. G. Moon *et al.*, "Glancing angle deposited WO_3 nanostructures for enhanced sensitivity and selectivity to NO_2 in gas mixture," *Sensors and Actuators, B: Chemical*, vol. 229, pp. 92–99, Jun. 2016, doi: 10.1016/j.snb.2016.01.084.

[69] F. Huber, S. Riegert, M. Madel, and K. Thonke, "H_2S sensing in the ppb regime with zinc oxide nanowires," *Sensors and Actuators, B: Chemical*, vol. 239, pp. 358–363, Feb. 2017, doi: 10.1016/j.snb.2016.08.023.

[70] J. Deng, B. Yu, Z. Lou, L. Wang, R. Wang, and T. Zhang, "Facile synthesis and enhanced ethanol sensing properties of the brush-like ZnO-TiO2 heterojunctions nanofibers," *Sensors and Actuators, B: Chemical*, vol. 184, pp. 21–26, 2013, doi: 10.1016/j.snb.2013.04.020.

[71] T. Li, W. Zeng, and Z. Wang, "Quasi-one-dimensional metal-oxide-based heterostructural gas-sensing materials: A review," *Sensors and Actuators, B: Chemical*, vol. 221. Elsevier, pp. 1570–1585, Dec. 31, 2015. Doi: 10.1016/j.snb.2015.08.003.

[72] R. Ishihara, Y. Yamaguchi, K. Tanabe, Y. Makino, and K. Nishio, "Preparation of Pt/WO 3 -coated polydimethylsiloxane membrane for transparent/flexible hydrogen gas sensors," *Materials Chemistry and Physics*, vol. 226, pp. 226–229, Mar. 2019, doi: 10.1016/j.matchemphys.2018.12.052.

[73] Y. Wang *et al.*, "NH3 gas sensing performance enhanced by Pt-loaded on mesoporous WO_3," *Sensors and Actuators, B: Chemical*, vol. 238, pp. 473–481, Jan. 2017, doi: 10.1016/j.snb.2016.07.085.

[74] S. Vallejos, I. Grácia, O. Chmela, E. Figueras, J. Hubálek, and C. Cané, "Chemoresistive micromachined gas sensors based on functionalized metal oxide nanowires: Performance and reliability," *Sensors and Actuators, B: Chemical*, vol. 235, pp. 525–534, Nov. 2016, doi: 10.1016/j.snb.2016.05.102.

[75] J. H. Kim, A. Katoch, and S. S. Kim, "Optimum shell thickness and underlying sensing mechanism in p-n CuO-ZnO core-shell nanowires," *Sensors and Actuators, B: Chemical*, vol. 222, pp. 249–256, Jan. 2016, doi: 10.1016/j.snb.2015.08.062.

[76] S. Bai *et al.*, "Polyaniline@SnO_2 heterojunction loading on flexible PET thin film for detection of NH3 at room temperature," *Sensors and Actuators, B: Chemical*, vol. 226, pp. 540–547, Apr. 2016, doi: 10.1016/j.snb.2015.12.007.

[77] J. Sun *et al.*, "Preparation of polypyrrole@WO_3 hybrids with p-n heterojunction and sensing performance to triethylamine at room temperature," *Sensors and Actuators, B: Chemical*, vol. 238, pp. 510–517, Jan. 2017, doi: 10.1016/j.snb.2016.07.012.

[78] S. H. Yan *et al.*, "Synthesis of SnO_2-ZnO heterostructured nanofibers for enhanced ethanol gas-sensing performance," *Sensors and Actuators, B: Chemical*, vol. 221, pp. 88–95, Jul. 2015, doi: 10.1016/j.snb.2015.06.104.

[79] V. K. Tomer, S. Devi, R. Malik, S. P. Nehra, and S. Duhan, "Highly sensitive and selective volatile organic amine (VOA) sensors using mesoporous WO_3-SnO_2 nanohybrids," *Sensors and Actuators, B: Chemical*, vol. 229, pp. 321–330, Jun. 2016, doi: 10.1016/j.snb.2016.01.124.

[80] O. Merdrignac-Conanec and P. T. Moseley, "Gas sensing properties of the mixed molybdenum tungsten oxide, W0.9Mo0.1O3," *Journal of Materials Chemistry*, vol. 12, no. 6, pp. 1779–1781, 2002, doi: 10.1039/b111118n.

[81] D. R. Miller, S. A. Akbar, and P. A. Morris, "Nanoscale metal oxide-based heterojunctions for gas sensing: A review," *Sensors and Actuators, B: Chemical*, vol. 204. Elsevier, pp. 250–272, Dec. 01, 2014. Doi: 10.1016/j.snb.2014.07.074.

[82] W. Yu *et al.*, "Improving gas sensing performance by oxygen vacancies in sub-stoichiometric WO_{3-x}," *RSC Advances*, vol. 9, no. 14, pp. 7723–7728, 2019, doi: 10.1039/c9ra00116f.

[83] W. Ding, D. Liu, J. Liu, and J. Zhang, "Oxygen Defects in Nanostructured Metal-Oxide Gas Sensors: Recent Advances and Challenges†," *Chinese Journal of Chemistry*, vol. 38, no. 12, pp. 1832–1846, Dec. 2020, doi: 10.1002/cjoc.202000341.

[84] Y. Qin, M. Hu, and J. Zhang, "Microstructure characterization and NO_2-sensing properties of tungsten oxide nanostructures," *Sensors and Actuators, B: Chemical*, vol. 150, no. 1, pp. 339–345, Oct. 2010, doi: 10.1016/j.snb.2010.06.063.

[85] D. B. Migas, V. L. Shaposhnikov, and V. E. Borisenko, "Tungsten oxides. II. The metallic nature of Magńli phases," *Journal of Applied Physics*, vol. 108, no. 9, Nov. 2010, doi: 10.1063/1.3505689.

[86] S. Cong, F. Geng, and Z. Zhao, "Tungsten Oxide Materials for Optoelectronic Applications," *Advanced Materials*, vol. 28, no. 47, pp. 10518–10528, Dec. 2016, doi: 10.1002/adma.201601109.

[87] J. Liu *et al.*, "Influence of oxygen vacancy behaviors in cooling process on semiconductor gas sensors: A numerical analysis," *Sensors (Switzerland)*, vol. 18, no. 11, 2018, doi: 10.3390/s18113929.

[88] J. S. Moya, S. Lopez-Esteban, and C. Pecharromán, "The challenge of ceramic/metal microcomposites and nanocomposites," *Progress in Materials Science*, vol. 52, no. 7. Pp. 1017–1090, Sep. 2007. Doi: 10.1016/j.pmatsci.2006.09.003.

[89] P. Henrique Cury Camargo, K. Gundappa Satyanarayana, and F. Wypych, "Nanocomposites: Synthesis, Structure, Properties and New Application Opportunities." [Online]. Available: www.scirus.com

[90] F. L. Meng, Z. Guo, and X. J. Huang, "Graphene-based hybrids for chemiresistive gas sensors," *TrAC – Trends in Analytical Chemistry*, vol. 68. Elsevier B.V., pp. 37–47, May 01, 2015. Doi: 10.1016/j.trac.2015.02.008.

[91] Batková, J. Čapek, J. Rezek, R. Čerstvý, and P. Zeman, "Effect of positive pulse voltage in bipolar reactive HiPIMS on crystal structure, microstructure and mechanical

properties of CrN films," *Surface and Coatings Technology*, vol. 393, Jul. 2020, doi: 10.1016/j.surfcoat.2020.125773.

[92] J. Čapek *et al.*, " Bixbyite-Ta 2 N 2 O film prepared by HiPIMS and postdeposition annealing: Structure and properties ," *Journal of Vacuum Science & Technology A*, vol. 38, no. 3, p. 033409, May 2020, doi: 10.1116/6.0000066.

[93] P. Zeman *et al.*, "Superior high-temperature oxidation resistance of magnetron sputtered Hf-B-Si-C-N film," *Ceramics International*, vol. 42, no. 4, pp. 4853–4859, Mar. 2016, doi: 10.1016/j.ceramint.2015.11.171.

[94] Y. Zhao *et al.*, "Preparation of WO_3 Films with Controllable Crystallinity for Improved Near-Infrared Electrochromic Performances," *ACS Sustainable Chemistry and Engineering*, vol. 8, no. 31, pp. 11658–11666, Aug. 2020, doi: 10.1021/acssuschemeng.0c03141.

[95] R. Jolly Bose *et al.*, "Preparation and characterization of Pt loaded WO 3 films suitable for gas sensing applications," *Applied Surface Science*, vol. 440, pp. 320–330, May 2018, doi: 10.1016/j.apsusc.2018.01.098.

[96] M. Z. Ahmad *et al.*, "Hydrogen sensing using gold nanoclusters supported on tungsten trioxide thin films," in *International Journal of Hydrogen Energy*, Sep. 2013, vol. 38, no. 29, pp. 12865–12877. Doi: 10.1016/j.ijhydene.2013.07.089.

[97] H. P. Dang, Q. H. Luc, V. H. Le, and T. Le, "The influence of deposition temperature and annealing temperature on Ga-doped SnO_2films prepared by direct current magnetron sputtering," *Journal of Alloys and Compounds*, vol. 687, pp. 1012–1020, 2016, doi: 10.1016/j.jallcom.2016.06.236.

[98] J. Vlček *et al.*, "High-rate reactive high-power impulse magnetron sputtering of hard and optically transparent HfO2 films," *Surface and Coatings Technology*, vol. 290, pp. 58–64, Mar. 2016, doi: 10.1016/j.surfcoat.2015.08.024.

[99] J. Musil and P. Baroch, "High-rate pulsed reactive magnetron sputtering of oxide nanocomposite coatings," *Vacuum*, vol. 87, pp. 96–102, 2013, doi: 10.1016/j.vacuum.2012.02.023.

[100] A. D. Pajdarová and J. Vlček, " Effects of power per pulse on reactive HiPIMS deposition of ZrO 2 films: A time-resolved optical emission spectroscopy study ," *Journal of Vacuum Science & Technology A*, vol. 37, no. 6, p. 061305, Dec. 2019, doi: 10.1116/1.5125721.

[101] T. Kozák and J. Vlček, "A parametric model for reactive high-power impulse magnetron sputtering of films," *Journal of Physics D: Applied Physics*, vol. 49, no. 5, Dec. 2015, doi: 10.1088/0022-3727/49/5/055202.

2 Methodology

In this chapter, a detailed overview of experimental and characterization techniques used to prepare and characterize the WO_3 is presented. Since the experimental setup has taken a great deal of the scientific work being discussed in this thesis, in this chapter, the synthesis specifics and testing routines, which cannot be covered in individual manuscripts, are described.

Mainly, two types of sputtering systems have been used to deposit materials such as WO_{3-x}, CuO, $CuWO_4$, Cu_2WO_4, and Pd/PdO. The thin films of WO_{3-x} were deposited by a reactive magnetron sputtering system in DC and HiPIMS mode, while the CuO and Pd/PdO films were deposited by the reactive sputtering system in RF mode. The RF mode sputters the CuO/Pd target uniformly without any racetrack. The thicknesses of CuO and Pd films are less than 20 nm and 1 nm, respectively which can easily be deposited and controlled in RF mode. The CuO nanoclusters were deposited using a magnetron-based gas aggregation cluster source (GAS).

2.1 Synthesis of Nanostructured Materials

The individual manuscripts contain information about the synthesis parameters. Here, only general remarks are given.

a) Preparation of the Substrates

The Si wafer with plane orientation (001) was thermally oxidized by using a long-term annealing system that can be heated to 1800° C with a heating rate in the range of 0.1 to 50 °C/min in the presence of oxygen or argon. The thermal oxidation leads to a growth of a 2-µm-thick SiO_2 layer over the Si wafer. The Si wafer is then cut into pieces of dimension 9×9 mm^2 or 10×10 mm^2. In the next step, the substrates were cleaned using an ultrasonicator for 10 minutes in isopropyl alcohol and 10 minutes in DI water and dried by blowing nitrogen.

b) Deposition of Thin Film and Nanoclusters

A Leybold-Heraeus sputtering deposition system (LH Z400) has been used for the preparation of the thin films of MOS. The sputtering system is mounted with a horizontal cylindrical chamber of a total volume of 25 liters and a diameter of 42 cm. Three grounded/biased substrate holders with a heating plate underneath are placed at the bottom, and a carousel with four different target holders is facing it from the top side shown in Figure 2.1. This allows the deposition of various materials from different targets (**Error! Reference source not found.**). The rotation of the target

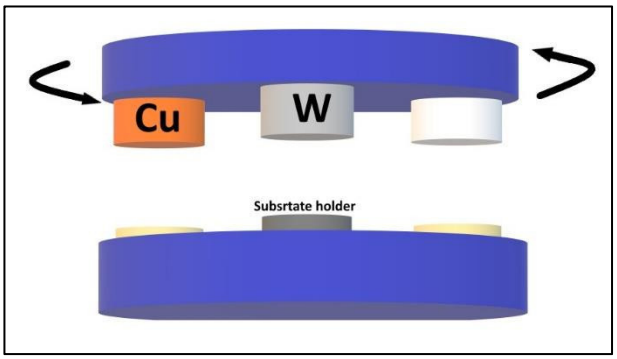

Figure 2.1 Schematic of target holder inside the vacuum chamber.

carousel can be controlled from outside the vacuum chamber.

Targets can be connected with various modes of power supply, such as DC, RF, and HiPIMS. A regular flow of water circulates across the target and the chamber to control heat damage. The chamber was connected to a turbomolecular pump (TMP) of a pumping speed up to 690 l/s (for nitrogen gas) which is backed by a scroll pump. The chamber can be pumped down to a base pressure of 1.0×10^{-3} Pa. There are three gas inlets into the chamber where argon is used for plasma generation, oxygen as a reactive gas, and nitrogen is used to vent the chamber. The partial pressure of the gases is controlled by the flow controllers to optimize the stoichiometry, quality, and crystallinity of the films. The base pressure can be lowered (not measurable in the

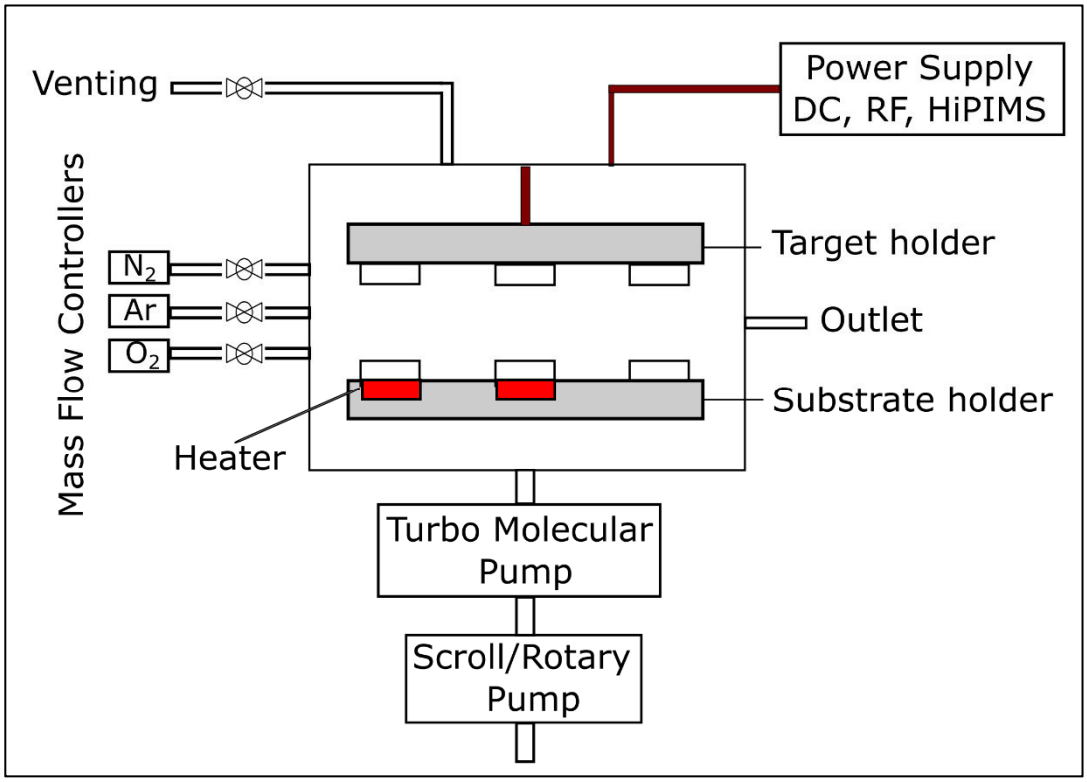

Figure 2.2 Schematic of Leybold-Heraeus LH Z 4000

current setup) by the use of a cold trap cooled by approx. 300 ml of liquid nitrogen. This is advantageous for very pure films, especially when oxidation of the deposited metal is not desired.

All WO_3 and CuO (also Pd) films investigated in the thesis were deposited by the above-mentioned sputtering system using DC and RF modes, respectively. In order to prepare WO_3 films, a tungsten metallic target connected with a planar magnetron was sputtered in Ar and O_2 environment. The flow rates of Ar and O_2 and substrate temperature were varied to achieve crystalline films. Moreover, the Cu target was used to deposit various phases of copper oxide films in RF mode. Basically, three phases of copper oxide, CuO, Cu_2O, and Cu_4O_3, were obtained at the various partial pressures of Ar:O_2 ratios, of which we continued with the CuO phase for further studies. The individual values of the deposition parameters for WO_3 and CuO films are described in Chapter 4 Sections A, B, and C.

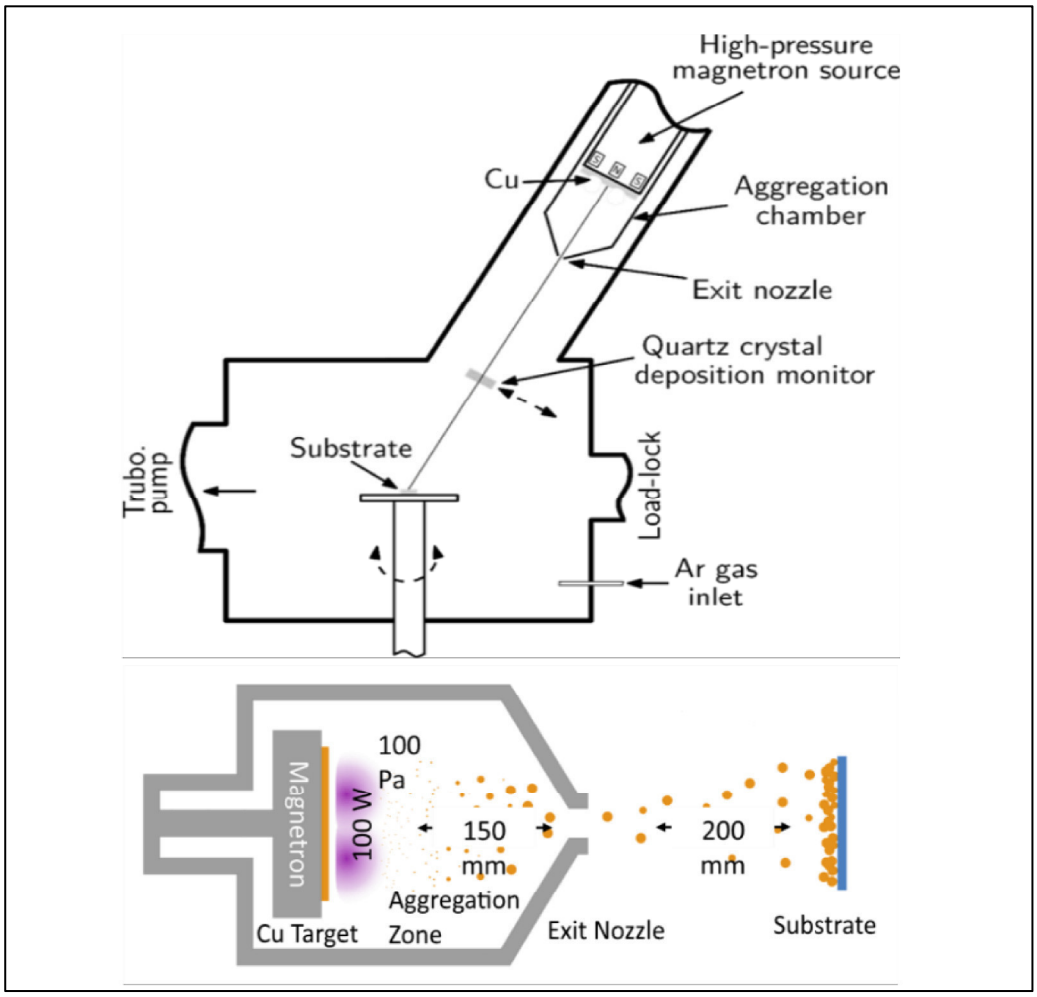

Figure 2.3 Schematic diagram of gas-aggregation based magnetron sputtering system b) Gas aggregation source.

In order to prepare sub-stoichiometric WO_{3-x} films, a unipolar high pulsed power supply was connected to the magnetron of the Leybold sputtering system (LH Z 400). HiPIMS was used to deposit crystalline WO_{3-x} films at lower deposition temperature and other deposition parameters were varied to achieve sub-stoichiometry and crystallinity in WO_{3-x} films. The thick films up to 1.5 µm were deposited to study the effect of the HiPIMS discharge parameters on the properties of the film, described in Chapter 4 Section D. The selected parameters were then used to prepare thin films (~100 nm) to study there to hydrogen gas detection. Further parameters will be provided in Chapters 4 Sections D and E specifically.

Gas aggregation sputtering system was used to prepare the nanoclusters. This customized gas aggregation source (GAS) consists of a movable cylindrical magnetron which is equipped with a Cu metallic target of diameter 5 cm and a cylindrical aggregation chamber. This GAS has a conical ending where the exit orifices with 1.5–4 mm of diameter range. This gas-aggregation source is connected at an angle of 30° to another vacuum chamber which is pumped by TMP with a speed up to 1250 l/s backed by a scroll pump. The base pressure in the main vacuum chamber and aggregation chamber before each deposition was 8×10^{-6} Pa and 2×10^{-5} Pa, respectively. The schematic is shown in Figure 2.3. The vacuum chamber has a rotating substrate holder to deposit the cluster uniformly on the substrates.

2.2 Characterization Techniques

This section briefly describes the characterization techniques used to study the properties of the as-prepared nanostructured materials. Also, the sensitivity measurement system is discussed in detail.

c) Characterization of Materials

In order to study the crystalline phases of the as-deposited films, XRD patterns are carried out using an X'Pert Pro PANalytical diffractometer system with Cu K_α radiation source in the Bragg-Brentano configuration. In the case of thin films, the ω-offset can be set according to the requirements to eliminate the reflection of the plane of the substrate, which is Si (001) in our case. Because the films thicknesses of the combined materials are too low, it is difficult to differentiate the phases by XRD because of the overlapping of the peaks. Raman spectroscopy (Horiba Jovin Yvon LABRAM HR Evolution) using a 532 nm laser and 100x magnification is carried out to overcome the issue of the crystalline phases in the as-deposited films.

The cross-sectional and top-view of the films are measured by using a Hitachi SU-70 scanning electron microscope consists of a vacuum chamber pumped by a scroll pump. The microscope is equipped with backscattered electron (BSE), secondary electrons (SE), transmission electrons (TE) detectors., Inside the chamber of the microscope energy dispersive X-rays spectroscopy (EDS), and wavelength dispersive X-rays spectroscopy (WDS) can be measured. The primary energy of the electron beam was in the range of 5 kV to 20 kV. In order to measure the thickness of the as-deposited film, a cross-sectional view is measured from SEM. To carry out the cross-sectional view the specimens are simply broken through a pre-scratch on substrates with deposited films. A thin film of chromium is deposited by a tabletop magnetron sputtering system (XXXX) on the specimens before taking the SEM measurements. Specific parameters used to image surface morphology and cross-sectional views are shown in Chapter 4

d) Sensitivity Measurement System

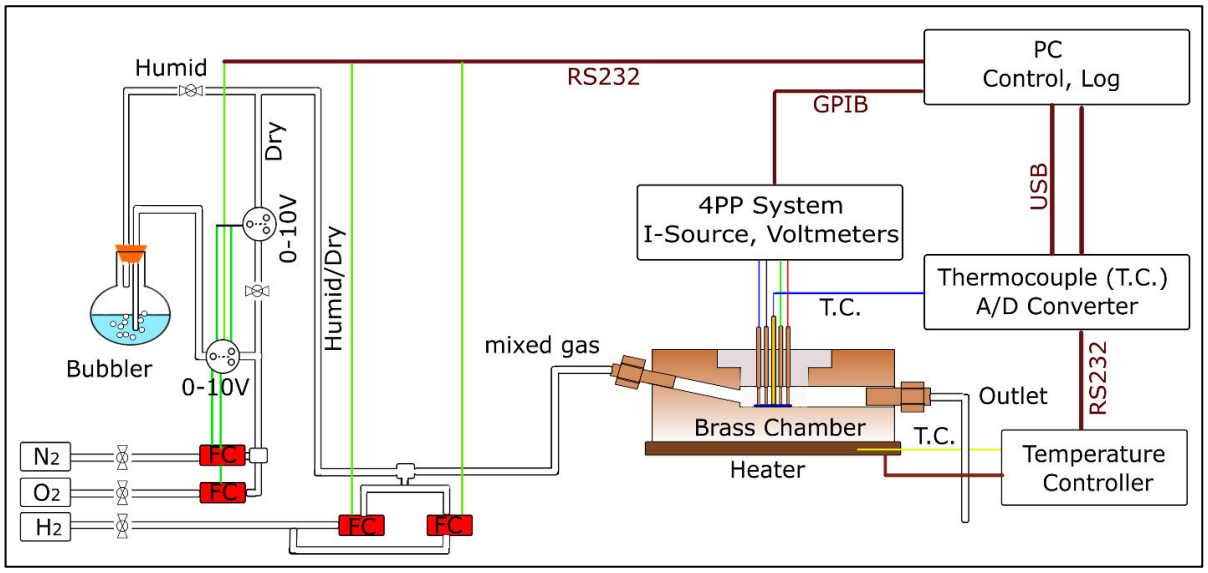

Figure 2.4 Schematic of custom-built sensitivity measurement system.

The sensing response of the sensors manufactured by the various combinations of the films was measured using a custom-built system as shown in Figure 2.4. A cylindrical brass chamber with a volume of 1 cm^3 consists of a gas inlet and outlet, mounted on a heating plate that is controlled by a temperature controller (*QuietChuck*). The flows of N_2 and O_2 can be precisely controlled by the *Alicat Scientific* mass flow controllers (FC, red boxes in Figure 2.4) with a range of 200 and 100 sccm, respectively, to adjust the required gas flow of carrying synthetic gas. Into the flow of the synthetic gas (usually 100 sccm total) a portion of hydrogen is inserted using flow controllers with ranges 10 and 1 sccm (depending on the concentration level a proper one is selected). To measure the conductometric response of the sensor to the hydrogen gas, the Four-Point Probe (4PP) technique is deployed by using four 1.5 cm long gold-plated spring-loaded pins with 2-mm pitch, which are pressed to the surface of the specimen placed inside the reaction chamber. In addition, a thermocouple (T.C.) is also placed along with the pins to record the temperature at the surface of the specimen during the measurements. The electrical parameters are governed by a DC source (*Keithley 6220*) and two electrometers (*Keithley 6514*). A LabVIEW-based software is utilized to control the whole setup and it precisely measures the change in the resistance values in presence of the various concentrations of hydrogen gas in synthetic air at various temperatures.

The above-described setup has been developed, and recently a further upgrade was done by introducing a water bubbler that produces water vapors to create a humid environment inside the chamber. The amount of relative humidity (RH) is controlled by mixing humid and dry air by varying their flows using two electrically driven valves. In order to study the influence of humidity on hydrogen gas detection (see Chapter 4 Section C), the percentage of RH volume can be varied from 0 to 90% in the gas mixture.

In order to examine rigorously the sensing response, the sample placed in the brass chamber is heated to various temperatures for a long time to reach a stabilization point of resistance value. The optimum temperature is determined by increasing the temperature in steps from room temperature to approximately 350 °C. The hydrogen cycle is continuously repeated at each

temperature for a couple of hours to observe the detectable but stable response. Furthermore, the specimens were heated at the optimum temperature for a long time to stabilize the structure and oxidation of the surface materials. The duration of stabilization is completely dependent on the specimen surface properties and temperature values. For example, $CuWO_4/WO_{3-x}$ stabilizes after 3–4 hours, on the other hand, it takes Pd-WO_{3-x} takes 6–7 hours to stabilize. Some samples were necessary to stabilize for more than 14 hours.

The sensing characteristics are recorded after stabilization by varying hydrogen concentrations at a constant applied electric current. The curves are shown in Figure 2.5a. The figure shows a red curve for the H_2 concentration which varies in the steps of 0, 200, 500, 7500, and 10000 ppm in synthetic air, and the other curve (black curve) is the resistance change at different values of H_2 concentration. Since hydrogen is reducing gas the resistance value decreases for N-type semiconductors such as $CuWO_4$, WO_3, and PdO and increases for P-type semiconductors such as CuO in this research work.

Figure 2.5b shows the long-term stability measurement by varying hydrogen concentration in the range 0–1 vol% in synthetic air. Sensitivity is measured using the maximum and minimum values of resistance in the absence and presence of hydrogen gas, respectively, as described with *equation 1* in Chapter 1. The values of resistance are obtained by fitting the data by the sum of two exponential decays [39]. The equation is as follows:

$$\boldsymbol{R(t) = R_0 + A_1.e^{-t/T1} + A_2.e^{-t/T2}}$$

Where R_0 denotes the saturation values of resistivity, $A_{1,2}$ and $T_{1,2}$ are the amplitudes and time constants of exponential fit.

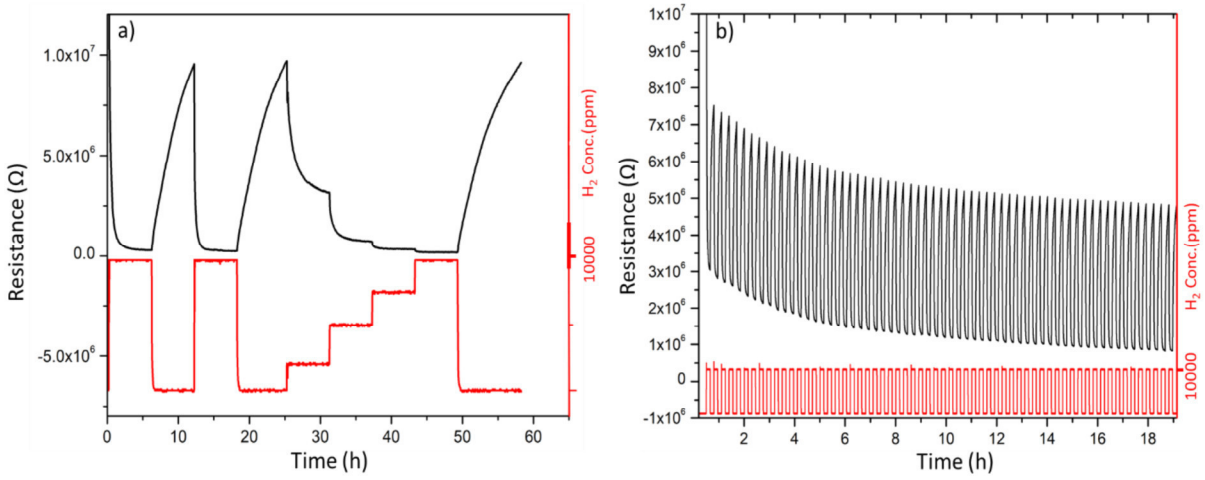

Figure 2.5 a) Sensing response at various concentrations of H_2. b) Response for a long cycle of 0-1Vol% of H_2 gas.

3 Research Objectives

This Ph.D. thesis reports on the preparation and characterization of nanostructured thin films of metal-oxide semiconductors deposited by sputtering techniques in order to find and explain relations between process parameters, properties, and sensing characteristics of prepared materials. The main focus is given to the enhancement of the sensing response of the materials toward hydrogen gas by combining the various metal-oxide semiconductors.

The main objectives of the thesis are as follows.

1) The purpose of this work was to design and develop a sensitivity measurement system and process routines to detect hydrogen gas in dry and humid environments at various temperatures and various concentrations of hydrogen gas.

2) To deposit crystalline WO_3 thin films by reactive magnetron sputtering with controlled deposition parameters at low deposition temperature (less than 400 °C).

3) Propose the reactive HiPIMS method to tune the crystalline structure and stoichiometry of the WO_{3-x} films to improve the sensing performance of as-deposited films.

4) Investigate the effect of various architectures and combinations of WO_3 with other noble metals (Pd) and MOS (CuO, $CuWO_4$, and PdO) on the sensing response to the H_2 gas.

5) To lower the operating temperature of the WO_3 based gas sensor toward hydrogen gas.

6) Reduce the influence of humidity on hydrogen gas sensing.

4 Results

This chapter represents the results of various detailed investigations of the sensing response of the combinations of CuO, $CuWO_4$, Pd, and PdO with WO_{3-x} towards the H_2 gas. The results are divided into 5 sections (A–E). Sections A, B, D, E are shown in the form of the research article published in peer-reviewed international journals. Section C is a manuscript currently in the process of publication. The most important results obtained during my Ph.D. are published in these articles. Every section of this chapter is based on the improvement of the sensing performance by adopting the strategies discussed in Chapter 1, Section 1.6 Challenges and Strategies.

In Section A, the thin films of WO_3 are decorated with various densities of CuO nanoclusters. The article presents the preparation and characterization of this architecture, study structure, morphology, and sensing response toward hydrogen gas of the prepared material system. In addition, the I–V characteristics of this combination by a modified geometry are studied to investigate the formation of heterojunction at the interface of CuO nanoclusters and WO_3 film.

The in-situ formation of $CuWO_4$ in situ by depositing CuO film on the WO_3 film is described in Section B. It also describes the formation and variation of $CuWO_4$ nano-islands by varying the thickness of RF-sputtered CuO. The formation of heterojunction at the $CuWO_4/WO_3$ interface enhances the sensing response. A similar structure by depositing the CuO and WO_3 films in reverse order gives the formation of $CuWO_4$ over CuO films are shown in Section C. Here, the bilayers are further improved by adding Pd/PdO nanoparticles and nanoislands over the $CuWO_4$/CuO bilayers for the purpose of further enhancement of the sensing response and reduction of the influence of relative humidity. Interestingly, all the structures are deposited using the conventional sputtering system in DC and RF regimes.

In order to reduce the deposition temperature, HiPIMS produced crystalline WO_{3-x} films, and the results are shown in Sections D and E. The reactive HiPIMS model and the discharge plasma model for the ionization region are combined for a deeper understanding of the influence of discharge parameters such as the voltage pulse length, the oxygen partial pressure, and the pulse-averaged target power density on the deposition rate and oxygen concentration in the WO_{3-x} films (Section D). The voltage pulse length is varied to tune the structure and Stoichiometry of WO_{3-x} thin films (Section E) and study the effect of oxygen vacancies on sensing response.

A

Hydrogen Gas Sensing Properties of WO_3 Sputter-Deposited Thin Films Enhanced by On-top Deposited CuO Nanoclusters

S. Haviar, J. Čapek, Š. Batková, **N. Kumar,** F. Dvořák, T. Duchoň, M. Fialová, P. Zeman

International Journal of Hydrogen Energy 43 (2018) 22756-22764

Available online at www.sciencedirect.com

ScienceDirect

journal homepage: www.elsevier.com/locate/he

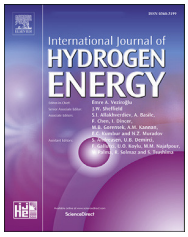

Hydrogen gas sensing properties of WO_3 sputter-deposited thin films enhanced by on-top deposited CuO nanoclusters

Stanislav Haviar [a,*], Jiří Čapek [a], Šárka Batková [a], Nirmal Kumar [a], Filip Dvořák [b], Tomáš Duchoň [b,c], Markéta Fialová [a], Petr Zeman [a]

[a] Department of Physics and NTIS-European Centre of Excellence, University of West Bohemia, Univerzitní 8, 30614, Plzeň, Czech Republic

[b] Department of Surface and Plasma Science, Faculty of Mathematics and Physics, Charles University, V Holešovičkách 2, 18000 Prague 8, Czech Republic

[c] Forschungszentrum Jülich GmbH, Peter Grünberg Institut 6, 52425, Jülich, Germany

ARTICLE INFO

Article history:
Received 15 August 2018
Received in revised form
12 October 2018
Accepted 15 October 2018
Available online 13 November 2018

Keywords:
Nanocomposites
Gas aggregation cluster source
Tungsten oxide
Cupric oxide
Hydrogen gas sensor
Magnetron sputtering

ABSTRACT

Magnetron-based gas aggregation cluster source (GAS) was used to prepare high-purity CuO (cupric oxide) nanoclusters on top of sputter-deposited thin film of tungsten trioxide (WO_3). The material was assembled as a conductometric hydrogen gas sensor and its response was tested and evaluated. It is demonstrated that addition of CuO clusters noticeably enhances the sensitivity of the pure WO_3 thin film. With an increasing amount of CuO clusters the sensitivity of CuO/WO_3 system rises further. When CuO clusters form a sufficiently thick and compact layer, the resistance response is reversed. Based on the sensorial behavior, conventional and near-ambient pressure X-Ray photoemission spectroscopies, and resistivity measurements, we propose that the sensing mechanism is based on the formation of nano-sized *p*-*n* junctions in between *p*-type CuO and *n*-type WO_3. The advantages of the GAS technique for preparing sensorial and/or catalytically active materials are emphasized.

Introduction

The hydrogen (H_2) energy market is rapidly growing and there is a strong interest in development of fast, stable and sensitive hydrogen gas sensors [1]. One of the most often explored approaches are chemiresistors based on metal-oxide semiconductors (MOSs) [2–4]. The main effort has been put into an improvement of the sensitivity, selectivity, stability and durability of the sensors [4]. Less attention has been paid to a development of new preparation methods that are compatible with thin-film microcircuit technology and also allowing large-scale production of the sensors. This is, however, a vital requirement for full integration of nanostructured sensorial materials into modern devices [5], such as on-chip fuel-cells. Last but not least, there is an effort to employ economically and environmentally reasonable materials for sensor production.

* *Corresponding author.*
E-mail address: haviar@ntis.zcu.cz (S. Haviar).

https://doi.org/10.1016/j.ijhydene.2018.10.127

Cupric oxide (CuO) has been getting more interest recently as one of the sensorial materials. The nanostructured CuO is used as a sensing material solely [6–10] or in combination with various *n*-type MOSs (SnO_2 [11,12], TiO_2 [13], WO_3 [14], …) most often to detect H_2S or NO_2 but rarely to detect H_2. Tungsten trioxide (WO_3) has been examined for its sensitivity to hydrogen [15,16] solely or in combination with other compounds (ZnO [17,18], SiC [19], PdO [20], …). The mentioned references employ various methods of preparation such as sol-gel or thermal. Most of the used recipes for preparation of nano-shaped materials require high-temperature sintering and/or complex post-treatment. These steps bring difficulties when considering scaling-up of the procedure or combining the techniques with thin-film microcircuit technology.

Magnetron sputtering is a versatile and scalable technique offering a possibility to prepare a wide range of MOSs in the form of a thin film with a tunable composition and microstructure. In the last decade, there has been an extensive development in the modification of the magnetron sputtering source into a magnetron-based gas aggregation cluster source (GAS) for production of nanoparticles. Such a source enables deposition of clusters with tunable diameter in the range 10^0–10^2 nm. As opposed to commonly used wet- or powder-based techniques, this sputtering-based approach produces high-purity microstructured materials in a wide range of both metallic and oxidic materials [21–24].

In this work, we present a novel advantageous approach utilizing GAS for preparation of a nanostructured hydrogen gas sensing material based on two high-purity MOSs. Tungsten trioxide (WO_3) in the form of a thin film and cupric oxide (CuO) clusters were selected as model materials due to the possibilities to finely control the stoichiometry and microstructure of WO_3 films and flux and size distribution of CuO clusters.

To our knowledge, we used the GAS for preparing a conductometric hydrogen gas sensor for the first time. The sensing response was enhanced (in comparison with the standalone materials) and moreover no noble metal was used for this.

At the end of the paper, the reaction sensing mechanism is discussed and an explanation based on the description of a formation of nano-sized heterojunctions [25] between *n*-type WO_3 and *p*-type CuO is proposed.

Material and methods

Material synthesis

All specimens were prepared on 10 × 10 mm^2 Si(111) substrates (625 μm thickness) with thermally grown SiO_2 (thickness > 350 nm). Before deposition the substrates were cleaned by sonication for 5 min in isopropylalcohol and demineralized water, subsequently.

The tungsten oxide films were deposited using a reactive *dc* magnetron sputtering from a tungsten target with a diameter of 72 mm in a stainless steel vacuum chamber (Leybold-Heraeus LH Z400) pumped by a turbomolecular pump (backed up with a scroll pump) and a cold trap (cooled by liquid nitrogen). The base pressure before each deposition was below 1×10^{-3} Pa. The substrate-to-target distance was 70 mm. The working gas was a mixture of argon and oxygen gases at flow rates of 14.0 sccm and 10.3 sccm, respectively. The working pressure was 635 mPa. The applied discharge target power of 60 W resulted in the deposition rate of 28.3 nm/min (deposited in oxide mode).

The nanoclusters were deposited using a magnetron-based gas aggregation cluster source (HVM Plasma Ltd.) attached to a second vacuum chamber. The chamber scheme is depicted in Fig. 1. It consists of a high-pressure magnetron source equipped with a circular Cu target 50 mm in diameter and a cylindrical water-cooled aggregation chamber. The cluster source is fitted onto a cylindrical stainless steel vacuum chamber at an angle of 30° from the vertical axis. The aggregation chamber was pumped together with the main chamber by a turbomolecular pump (HiPace 1200, Pfeiffer Vacuum) to a base pressure of 5×10^{-6} Pa. Argon (99.9999% purity) was introduced into the aggregation chamber at a flow rate of 140 sccm, resulting in a pressure of 76 Pa. The aggregation length (target-to-exit-nozzle distance) was set to 150 mm. The magnetron was driven by a *dc* power supply (TDK-Lambda Genesys) at a constant discharge target power of 100 W. The deposition rate of the cluster beam was monitored using a retractable quartz crystal microbalance. The rotating substrate holder was at a distance of 400 mm from the exit nozzle and the center of the cluster beam was directed at the center of the substrate holder. A dispersion of the cluster beam results in a gradient of density of clusters on the substrate holder. This was exploited for deposition of various amounts of clusters in a single deposition cycle just by placing the substrates at various distances from the center of the cluster beam.

Analyses

The scanning electron microscope (SEM) (Hitachi SU-70) was used for imaging of the specimens using a primary energy of

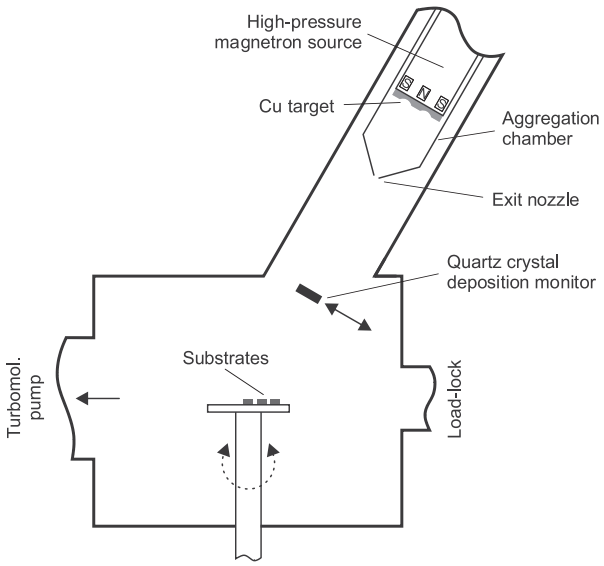

Fig. 1 – Scheme of the vacuum chamber with an attached gas aggregation cluster source. Key dimensions can be found in the text.

20 keV for top-view micrographs and 5 keV for cross-sectional views. The cross-sections of the specimens were produced by simply breaking the pre-scratched silicon substrates with the deposited films. Film thicknesses were determined from the cross-sectional views using image binarization; the RMS parameter is reported as an error of thickness.

X-ray diffraction (XRD) measurements of the structure of the as-deposited films were carried out using a diffractometer (X'Pert PRO, PANalytical) with Cu K_α radiation working in a slightly asymmetrical Bragg-Brentano geometry with an ω-offset of 1.5°and in the standard Bragg-Brentano geometry. The ω-offset was used to eliminate a strong reflection of the single-crystalline Si(100) substrate at 2θ angle of 69.17°. The data were collected using an ultrafast detector X'Celerator in the 2θ range of 15°–60°.

X-ray photoelectron spectroscopy (XPS) was performed with an Al K_α X-ray source ($h\nu = 1486.6$ eV, total energy resolution $E = 1$ eV) and the SPECS Phoibos MDC 9 energy analyzer. XPS measurement was performed in an ultrahigh vacuum (UHV) experimental chamber operating at a base pressure $< 10 \times 10^{-8}$ Pa.

Near-ambient pressure XPS (NAP) was performed in a laboratory UHV system with a monochromatized Al K_α X-ray source ($h\nu = 1486.6$ eV, total energy resolution $E = 0.6$ eV) and with SPECS Phoibos 150 1D DLD electron energy analyzer. The specimen was kept in an in-situ near-ambient pressure cell (maximum pressure 2 kPa) for XPS measurement in the reactive atmosphere. XPS data were acquired under conditions, which get close to working conditions of the sensor. The specimen was heated to 300 °C under 300 Pa of O_2 and then exposed to additional 30 Pa and 60 Pa partial pressure of H_2.

The gas response was analysed using a reaction chamber with a total volume of 9 cm^3. Three mass-flow controllers (Alicat Scientific, various flow ranges) were used to regulate the portions of N_2, O_2 and H_2 gases in the testing atmosphere, which was introduced into the chamber in the continuous-flow regime. The electrical contact was realized by a pair of gold-plated spring-loaded tips, which were pressed to the surface of the specimen; the spacing of the tips was 6 mm. Further details of the measurement chamber can be found in Ref. [15]. The sensitivity is defined as R_a/R_g or R_g/R_a for materials decreasing or increasing its resistivity in hydrogen, respectively. The R_a and R_g denote resistance in clean synthetic air and mixture of synthetic air with specified amount of hydrogen, respectively. The steady values were always obtained by fitting time dependence of resistance at changing hydrogen concentration. The fitting procedure is described also in Ref. [15].

The four-point resistance measurement of the macro heterojunction WO_3/CuO described in Section 3.3 was done using four-point technique with contacts attached to the surface using silver conductive paste.

Results and discussion

In order to investigate the sensorial behavior of WO_3 combined with CuO nanoclusters, WO_3 solid films with increasing amount of CuO clusters were deposited. These films are denoted as 'pure WO_3, sparse, low, medium, high' correspondingly to the increasing amount of CuO clusters deposited on-top of the WO_3 film.

Morphology and composition of films

In Fig. 2 there are XRD patterns of (a) as-deposited WO_3 thin film, (b) film with no clusters tested at 300 °C and (c) film with 25 nm thick cluster film tested at the same temperature. The films exhibit an orthorhombic crystalline structure with a preferred (002) orientation. There is no change in the structure after deposition of CuO nanoclusters. The film microstructure is stable at working temperature of 300 °C. The thickness of the film was measured as (85±4) nm.

In Fig. 3 there are top-view SEM micrographs of specimens with various amount of deposited clusters. From the 'sparse' specimen depicted in Fig. 3a one can see that the deposited clusters are approximately spherical within the resolution limit of the microscope. In order to quantify the amount of the CuO clusters we can calculate the surface coverage of the 'sparse' specimen to be 0.30±0.05. Other specimens show coverage greater than one. Therefore, they are characterized by the thickness of the nanocluster film. The thickness and morphology of the nanoclusters are visible in Fig. 4, where cross-sectional SEM micrograph of a 'low' specimen is depicted. For 'low', 'medium' and 'high' the determined thicknesses are 18, 25 and 27 nm, respectively. The overview of the film dimensions is given in Table 1.

The size of the clusters is characterized by a radius distribution histogram in Fig. 5. The statistics was acquired by image analysis of an SEM micrograph capturing an area of size of 1.1 μm^2. The density of clusters is similar to the density on 'sparse' specimen (see Fig. 3a). The size distribution does not change noticeably with the amount of deposited clusters, so we assume that the cluster size distribution remains the same for all specimens. There are two pronounced maxima visible in the distribution. The presence of two size families is in good

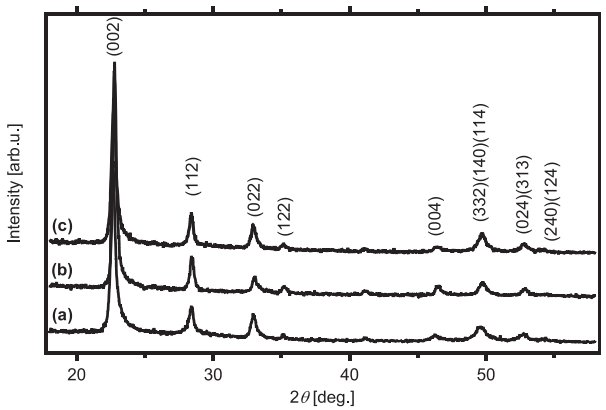

Fig. 2 – XRD patterns of (a) as-deposited WO_3 thin film, (b) film with no clusters after the test at 300 °C and (c) film with 25 nm thick cluster film tested at the same temperature. The structure is identified as orthorhombic crystalline structure with a preferred (002) orientation. All three patterns are almost identical. The film is stable at the used working temperature and deposition of cluster does not affect the microstructure.

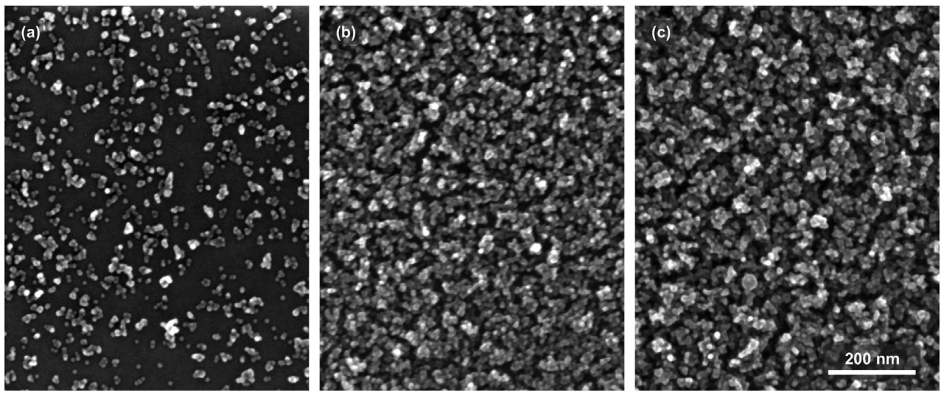

Fig. 3 – SEM micrographs of CuO/WO_3 specimens showing a varying concentration of CuO clusters on top of a WO_3 surface. The increasing surface concentration is denoted as 'sparse', 'low' and 'medium'. (The specimen 'high' is not shown since its top-view appearance does not differ from the 'medium'.)

agreement with Ref. [26]. According to this work, the histogram can be fitted by a sum of two log-normal distributions (the fitting function can be found in the figure caption). The dominant family is formed by clusters with a mean radius of 2.3 nm, the second family contains clusters with a mean radius of 4.9 nm (Based on our experience with the comparison of TEM and SEM measurements, we estimate the maximum error of clusters' radius to be [+0.1 nm; −0.6 nm].)

The composition of the prepared films was examined by means of XPS. The stoichiometry of the WO_3 film was confirmed by measurement of W 4f spectra as shown in Fig. 6. The only detected component is W^{6+} at a position of 35.6 eV [27,28]. This confirms that the film is a fully stoichiometric tungsten trioxide.

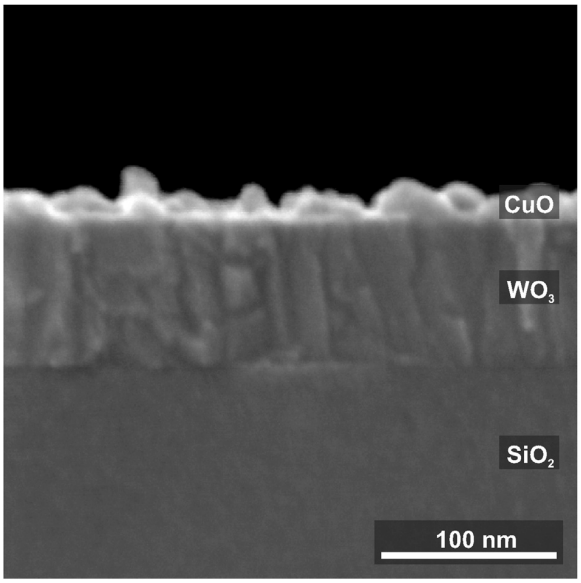

Fig. 4 – Example of cross-sectional SEM micrograph of CuO/WO_3 specimen. The thickness of the nanocluster layer for 'low' specimen was determined as (18±4) nm. The overview of film dimensions and of film properties is given in Table 1.

The chemical state of the nanoclusters was determined by means of XPS to be cupric oxide. An example of the typical specimens' Cu 2p spectrum is in Fig. 7. The chemical state of CuO is clearly confirmed by the presence of Cu^{2+} spectrum components [29]. Since the formation of the clusters takes place in a clean Ar atmosphere, the formation of the oxide takes place during the exposure to the ambient atmosphere [30]. The complete oxidation is eased by the porous structure of the film and the small dimensions of the clusters.

Sensorial behavior

The sensorial response of the prepared specimens is characterized by the dependence of electrical resistance on the concentration of hydrogen in synthetic air in Fig. 8. The hydrogen fraction was varied with a time period of 180 s and the concentration varied from 0% to 1% by volume. The sensor was assembled without the use of any noble metal catalyst, so the optimal working temperature was relatively high (300 °C) in comparison to optimized hydrogen sensors [31,32], but sufficiently low to keep the used oxides stable.

The specimens varied in initial resistivity (R_a) in steady state in synthetic air. Therefore the relative resistivity R/R_a is

Table 1 – Parameters of the examined specimens. R_a denotes the resistance in the synthetic air, R_g resistance at H_2 concentration of 1 vol%. The sensitivity is defined as R_a/R_g for the 'pure–medium' specimens and reversely as R_g/R_a for the 'high' specimen. See Fig. A.1 for sensitivity plots.

specimen	CuO amount [nm]	WO_3 film thickness [nm]	R_a [Ω]	Sensitivity [1]	τ_{90} [s]
pure	–		2.98×10^5	1.16	64
sparse	0.30 ± 0.05[a]		4.48×10^5	1.31	56
low	18 ± 4	85 ± 4	5.54×10^5	2.32	51
medium	25 ± 4		3.04×10^6	2.36	61
high	27 ± 6		2.20×10^6	1.30	28

[a] Coverage.

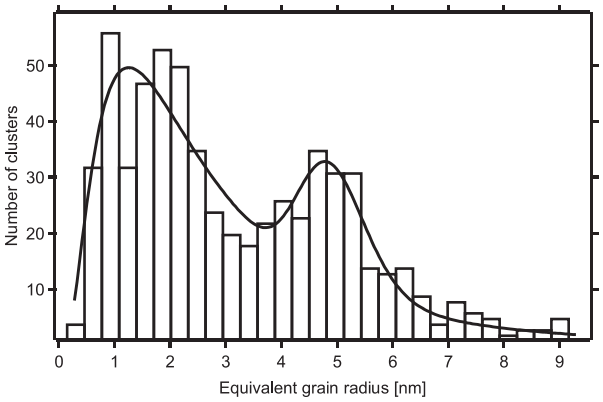

Fig. 5 – Histogram of clusters' equivalent radius r (clusters are considered to have spherical shape). The distribution was fitted with a sum of two log-normal distributions: $f(r) = \frac{1}{r\sqrt{2\pi}} \cdot \left[\frac{A_1}{\sigma_1}\exp\left(-\frac{(\ln r/R_1)^2}{2\sigma_1^2}\right) + \frac{A_2}{\sigma_2}\exp\left(-\frac{(\ln r/R_2)^2}{2\sigma_2^2}\right)\right]$. There are two dominant families of nanoclusters, with central radii gained from fit $R_1 = 2.3\pm0.2$ and $R_2 = 4.9\pm0.1$. The ratio of families' amplitudes is $A_1/A_2 = 5.2$.

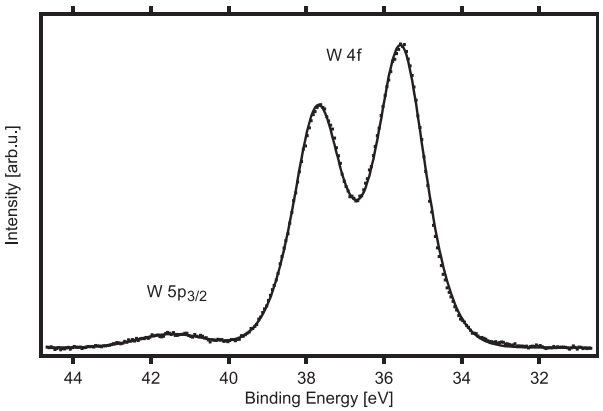

Fig. 6 – Fitting of W 4f photoelectron spectrum. The curve fitting of doublet W $4f_{7/2}$ and W $4f_{5/2}$ was performed with a fixed energy separation of 2.15 eV and a resulting peak ratio is 0.78. Accordingly, the only visible component W^{6+} is at an energy position of 35.6 eV [27,28].

plotted in Fig. 8 which enables a direct comparison of the specimens' response. The response of the pure WO_3 film is minute. With an increasing amount of CuO nanoclusters, the response is enhanced. The sensitivity values R_a/R_g for hydrogen concentration of 1.0 vol% are 1.2, 1.3, 2.3 and 2.4 for 'pure, sparse, low and medium' films, respectively.

The sensing characteristic is reversed when the amount of nanoclusters is increased even further. It is more sensible to calculate the sensitivity for 'high' specimen as $R_g/R_a = 1.3$ in this case.

The response and recovery time was obtained by fitting of the acquired data. The values of time constant τ_{90} are approximately the same for all specimens; the average is 57 s. The only exception is the reversely reacting specimen

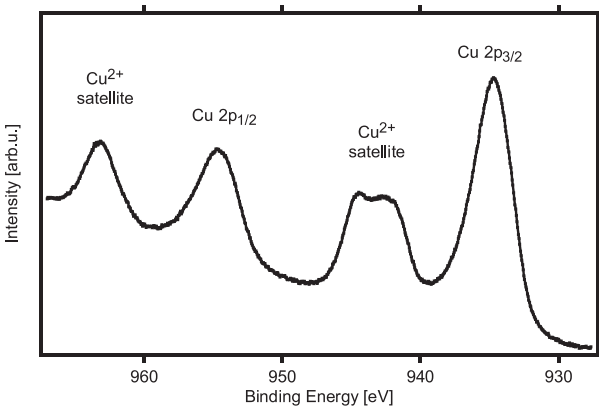

Fig. 7 – Cu 2p photoelectron spectrum typical for all specimens with CuO films. The Cu^{2+} state is clearly detectable by the presence of a strong satellite component located 8 eV toward higher binding energies in with respect to the Cu $2p_{3/2}$ peak at energy position of 934.6 eV.

with 'high' amount of nanoclusters, which exhibits the value $\tau_{90} = 28$ s.

The test was run four times for each specimen. The long-term stability was not tested.

All values are summarized in Table 1. In comparison with other approaches, the tested system worked at a similar temperature as radio frequency sputter-deposited Pd-loaded WO_3 films reported in Ref. [33]. Typically the reported working temperature is lower. This is typically achieved by addition of a noble metal ([34] – 150 °C), by light stimulation ([20] – room temperature) or by decorating with nanoparticles ([35] – 150 °C [36], – room temperature). The detection limit is lower in these cases in comparison with the bilayers presented in this paper. The response times are of the same order (tens of seconds), but a direct comparison is misleading since the working temperatures differ.

Discussion of the sensing mechanism

In order to explain the behavior of the CuO/WO_3 clusters the chemical state of the clusters in the presence of hydrogen was studied using near-ambient pressure XPS. The 'medium' specimen was held at the same working temperature of 300 °C as for sensorial measurements, and exposed to pure oxygen at a pressure of 300 Pa and the spectrum was acquired. Subsequently 30, 60 and 0 Pa of H_2 was added and the corresponding spectra were acquired. The Cu 2p spectra shown in Fig. 9 remain unchanged for all conditions and the presence of the Cu^{2+} satellite evidently proves that the clusters remain in the form of cupric oxide. In case of photoemission measurements the concentration of hydrogen is much higher than in the case of real sensor testing. Thanks to this, despite the fact that the pressure differs, we can assume that oxide clusters are not reduced (as in Ref. [37]) to metallic ones and the mechanism cannot be explained by the possibility that copper would act as a noble metal catalyst facilitating the dissociation of hydrogen [38]. Since the sensitivity of the sensor rises gradually with increasing amount of CuO clusters it is improbable

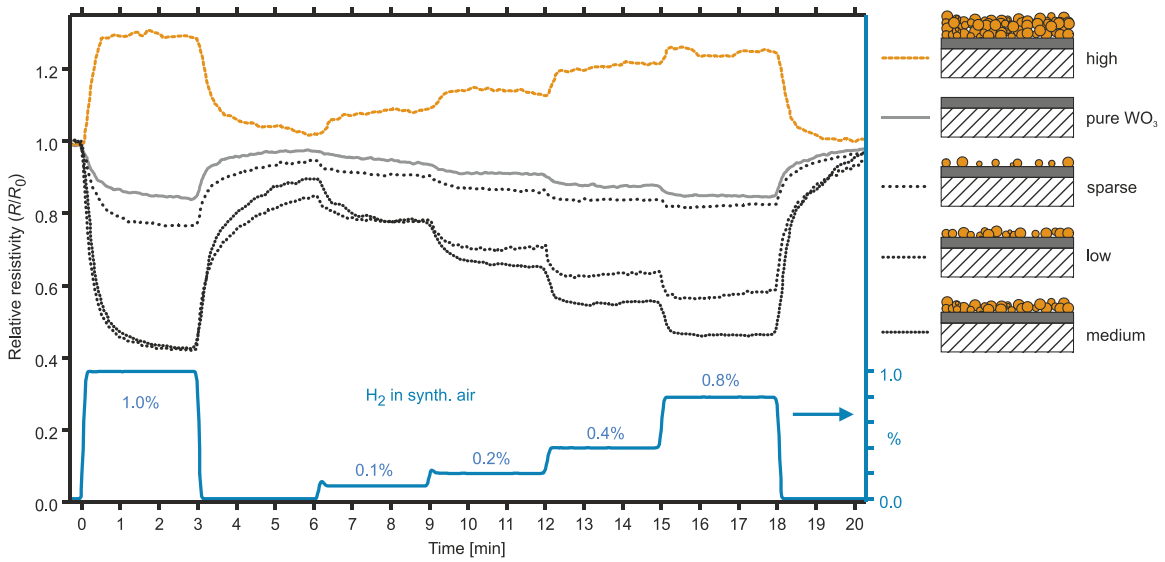

Fig. 8 – Resistive gas characterization of specimens with various amount of CuO nanoclusters. The concentration of hydrogen was modulated from 0.2 vol% up to 1.0 vol%. The response at 300 °C of pure WO_3 is poor. With an increasing amount of CuO the response increases. With the largest amount of CuO ('high') the response characteristic switches from *n*-type behavior to *p*-type behavior and so the resistivity is higher in the presence of hydrogen. See Fig. A.1 for corresponding sensitivity plots.

that the sensing mechanism differs from one specimen to the other. So, the results obtained for 'medium' specimen can be related for the other specimens as well.

Since the clusters remain MOS also in the working conditions, we propose the explanation of the sensing mechanism

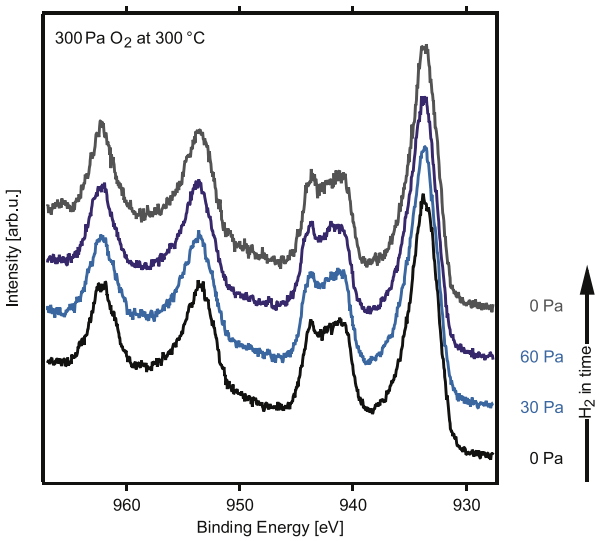

Fig. 9 – Waterfall plot of Cu 2p NAP spectra for the film topped by CuO clusters. The specimen was held at 300 °C and the spectra were measured at in a mixture of 300 Pa of O_2 with subsequently added H_2 at partial pressures 0, 30, 60 and 0 Pa representing 0, 9 and 17 vol%, respectively. There is no evidence of for reduction of CuO since the intensity of Cu^{2+} satellite is not changing.

by the formation of a heterojunctions between the *n*-type semiconductor WO_3 and the *p*-type CuO.

According to Ref. [5], the sensing mechanism on the pure WO_3 is described as follows (Fig. 10). The surface layer of the oxide loses electrons to the pre-adsorbed oxygen species originating from the air atmosphere. This forms a space charge region with a higher resistivity influencing the overall film resistance. During adsorption of hydrogen, thermal dissociation occurs and the atomic hydrogen reacts with the pre-adsorbed oxygen to form water molecules and the electron is returned to the material resulting in an increased conductivity. Contrary to commonly used sensors, our films are not equipped with a noble metal catalyst, therefore even at 300 °C the dissociation rate is poor and so is the response.

When the CuO is added on top of the WO_3 film in the form of nanoclusters, the heterojunction is formed near to the surface. The formation of the depletion region around the individual contacts of CuO with WO_3 results in a reduction of the conduction channel in the film and therefore in increase of the initial resistance (See initial resistance values R_a for specimens 'sparse'–'medium' in Table 1).

Furthermore, the reaction of hydrogen with the pre-adsorbed oxygen species takes place in a similar way as on pure WO_3; however, the injection of electrons during the forming of water molecules causes a larger change in the conduction channel size and therefore a larger resistive response. This description is in a good agreement with Ref. [20].

Another effect to be considered is surely the enlargement of the reaction surface when we presume that hydrogen can dissociate on a larger area provided by a porous CuO cluster film. Unfortunately, currently we are not able to quantitatively compare the particular contributions of the described effects.

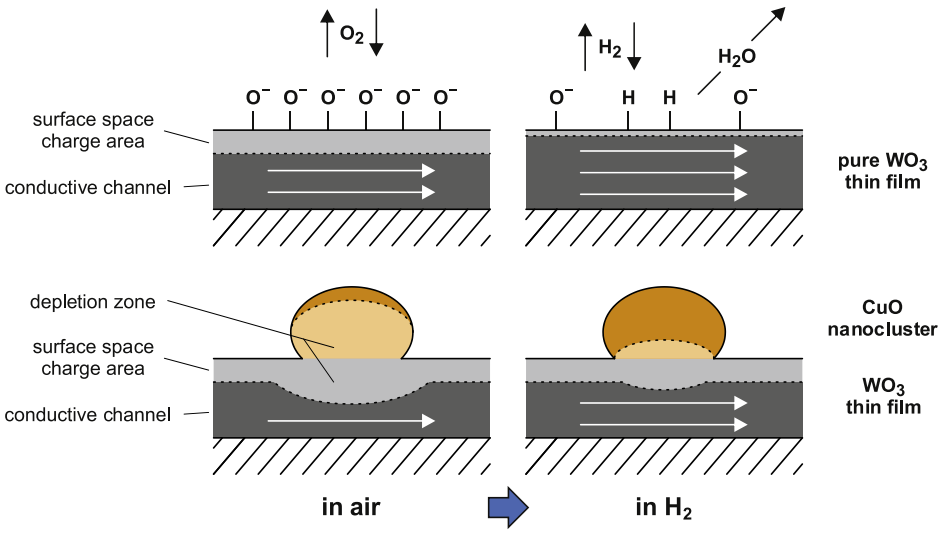

Fig. 10 – Diagram illustrating the proposed explanation of the sensing mechanism. The heterojunction is formed between the *p*-type CuO nanocluster and the *n*-type WO_3. The resulting depletion zone limits the conductive channel and influences the resistivity in air. During the exposure to H_2 the depletion zone is reduced by introducing electrons from desorbing water molecules.

We showed that the more CuO nanoclusters are added, the larger the resistive response for specimens 'sparse' to 'medium'. In case of further increase of the CuO clusters amount (the 'high' specimen) the main conductive channel is formed in the CuO cluster film itself and the heterojunction loses importance. The reaction of hydrogen with oxygen causes injection of an electron into the *p*-semiconductor leading to the a decrease of the number of the free charge carriers and therefore an increase of the resistance.

Further indication of forming of the network of heterojunctions can be seen in Table 1, where the initial resistances of each bi-layer are listed. With increasing amount of the CuO clusters (from 'sparse' to 'medium') the initial resistance rises, which indicates the forming of more heterojunctions resulting in higher overall volume of the depletion zones. This limits the resistance of the bi-layer.

The formation of the heterojunction is also indicated by the results of the I–V measurements shown in Fig. 11. The dedicated structure depicted in the inset of the figure was formed by partially overlapping a WO_3 thin film and a CuO nanocluster film. The thicknesses of the films were (38±2) nm and (72±3) nm, respectively. The I–V curve clearly shows the diode behavior. It proves that using our deposition technique, a *p-n* junction is formed on as-deposited materials, with no need for post-treatment.

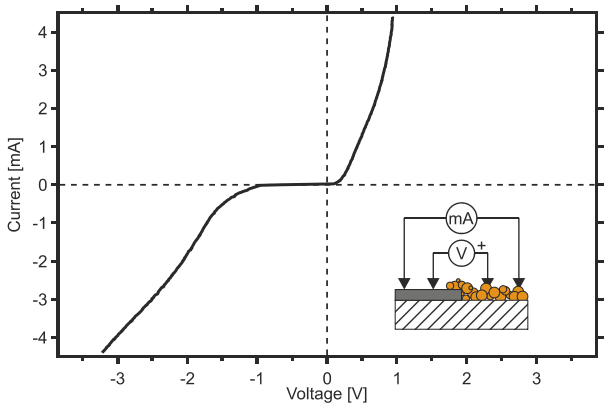

Fig. 11 – I-V characteristic of the structure depicted in the inset: CuO nanocluster film overlapping the WO_3 film in the central area (approx. 2 mm) of the specimen. The characteristic shows the diode behavior of the sputter-deposited bilayer. The electrical contacts on the 16 × 16 mm^2 specimen were placed with a spacing of 4 mm.

Conclusions

We used the gas aggregation cluster source technique for preparing a complex sensing material consisting of WO_3 thin film modified by on-top deposited CuO nanoclusters. The sensitivity rises with an increasing amount of clusters added to the surface of the WO_3 thin film. We believe that the mechanism is based on hydrogen-adsorption-stimulated change of volume of the nano *p-n* junctions formed at the contact of the WO_3 surface and the CuO nanoclusters. The formation of the depletion zone at the surface layer of the film changes the overall resistance and the variation due to the adsorption of hydrogen causes the response. When a continuous layer of the CuO nanoclusters is formed, the resistivity response is reversed and the interface between CuO and WO_3 does not play a role.

The final optimization of the sensitivity was not the goal of this research. On our model system CuO/WO_3 we demonstrated the advantages of the use of the gas aggregation cluster source technique, which can produce high-purity

particles which can be incorporated directly into functional materials.

The particles deposited by the cluster source were used "as-deposited" without the need of any post-treatment (sintering, drying, etc.). The used approach is compatible with microcircuit industry processes. This is a big advantage in contrary to commonly used wet techniques. Our approach can be therefore used for miniaturized portable devices using portable hydrogen-based devices.

In our case, the improvement of the response was achieved with no use of noble metal catalyst. In the future, the presented technique can be used for further straightforward optimization of the cluster size and/or composition. This will lead to more sensitive and applicable sensing materials.

Acknowledgements

The authors acknowledge the CERIC-ERIC Consortium for the access to experimental facilities and financial support.

The work was supported by the project LO1506 of the Czech Ministry of Education, Youth and Sports under the program NPU I.

S. H. would like to thank Dr. J. Rezek and Ass. Prof. Šimon Kos for their beneficial and useful comments.

Appendix A

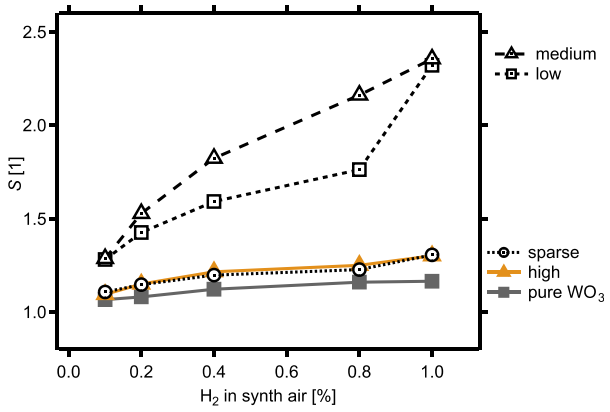

Fig. A.1 – Sensitivity plot of the examined specimens. The sensitivity is defined as R_a/R_g for the 'pure–medium' specimens and reversely as R_g/R_a for the 'high' specimen. See Table 1 for numerical values.

REFERENCES

[1] Hübert T, Boon-Brett L, Black G, Banach U. Hydrogen sensors – a review. Sensor Actuator B Chem 2011;157(2):329–52. https://doi.org/10.1016/j.snb.2011.04.070. https://doi.org/10.1016%2Fj.snb.2011.04.070.

[2] Barsan N, Weimar U. Conduction model of metal oxide gas sensors. J Electroceram 2001;7(3):143–67. https://doi.org/10.1023/a:1014405811371. https://doi.org/10.1023%2Fa%3A1014405811371.

[3] Korotcenkov G. Metal oxides for solid-state gas sensors: what determines our choice? Mater Sci Eng B 2007;139(1):1–23. https://doi.org/10.1016/j.mseb.2007.01.044. https://doi.org/10.1016%2Fj.mseb.2007.01.044.

[4] Dey A. Semiconductor metal oxide gas sensors: a review. Mater Sci Eng 2018;B 229:206–17. https://doi.org/10.1016/J.MSEB.2017.12.036. https://www.sciencedirect.com/science/article/pii/S0921510717303574?_rdoc=1&_fmt=high&_origin=gateway&_docanchor=&md5=b8429449ccfc9c30159a5f9aeaa92ffb.

[5] Korotcenkov G, Cho B, Han S, Cho B. Metal oxide composites in conductometric gas sensors: achievements and challenges. Sensor Actuator B Chem 2017;244:182–210. https://doi.org/10.1016/j.snb.2016.12.117. http://www.scientific.net/MSF.872.223Ωhttp://linkinghub.elsevier.com/retrieve/pii/S0925400516320895.

[6] Cerqui C, Ponzoni A, Zappa D, Comini E, Sberveglieri G. Copper oxide nanowires for surface ionization based gas sensor. Procedia Eng 2014;87:1023–6. https://doi.org/10.1016/J.PROENG.2014.11.335. https://www.sciencedirect.com/science/article/pii/S1877705814024503.

[7] Bari RH, Patil SB, Bari AR. Spray-pyrolized nanostructured CuO thin films for H2S gas sensor. Int Nano Lett 2013;3(1):12. https://doi.org/10.1186/2228-5326-3-12. http://link.springer.com/10.1186/2228-5326-3-12.

[8] Navale Y, Navale S, Stadler F, Ramgir N, Debnath A, Gadkari S, et al. Thermally evaporated copper oxide films: a view of annealing effect on physical and gas sensing properties. Ceram Int 2017;43(9):7057–64. https://doi.org/10.1016/j.ceramint.2017.02.135. https://doi.org/10.1016%2Fj.ceramint.2017.02.135.

[9] Zappa D, Comini E, Zamani R, Arbiol J, Morante J, Sberveglieri G. Copper oxide nanowires prepared by thermal oxidation for chemical sensing. Procedia Eng 2011;25:753–6. https://doi.org/10.1016/j.proeng.2011.12.185. https://doi.org/10.1016%2Fj.proeng.2011.12.185.

[10] Zappa D, Comini E, Zamani R, Arbiol J, Morante J, Sberveglieri G. Preparation of copper oxide nanowire-based conductometric chemical sensors. Sensor Actuator B Chem 2013;182:7–15. https://doi.org/10.1016/j.snb.2013.02.076. https://doi.org/10.1016%2Fj.snb.2013.02.076.

[11] Shao F, Hoffmann MWG, Prades JD, Zamani R, Arbiol J, Morante JR, et al. Heterostructured p-CuO (nanoparticle)/n-SnO2 (nanowire) devices for selective H2S detection. Sensor Actuator B Chem 2013;181:130–5. https://doi.org/10.1016/j.snb.2013.01.067. https://doi.org/10.1016/j.snb.2013.01.067Ω http://linkinghub.elsevier.com/retrieve/pii/S0925400513000841.

[12] Sukunta J, Wisitsoraat A, Tuantranont A, Phanichphant S, Liewhiran C. WO3nanotubesSnO2nanoparticles heterointerfaces for ultrasensitive and selective NO2detections. Appl Surf Sci 2018;458(July):319–32. https://doi.org/10.1016/j.apsusc.2018.07.096. https://doi.org/10.1016/j.apsusc.2018.07.096.

[13] Barreca D, Carraro G, Comini E, Gasparotto A, Maccato C, Sada C, et al. Novel synthesis and gas sensing performances of CuOTiO $_2$ nanocomposites functionalized with Au nanoparticles. J Phys Chem C 2011;115(21):10510–7. https://doi.org/10.1021/jp202449k. http://pubs.acs.org/doi/10.1021/jp202449k.

[14] Park S, Park S, Jung J, Hong T, Lee S, Kim HW, et al. H2S gas sensing properties of CuO-functionalized WO3 nanowires. Ceram Int 2014;40(7):11051–6. https://doi.org/10.1016/J.CERAMINT.2014.03.120. https://www.sciencedirect.com/science/article/pii/S0272884214004611.

[15] Haviar S, Chlupová Š, Kúš P, Gillet M, Matolín V, Matolínová I. Micro-contacted self-assembled tungsten oxide nanorods for hydrogen gas sensing. Int J Hydrogen

Energy 2017;42(2):1344–52. https://doi.org/10.1016/j.ijhydene.2016.09.187.
[16] Boudiba A, Roussel P, Zhang C, Olivier M-G, Snyders R, Debliquy M. Sensing mechanism of hydrogen sensors based on palladium-loaded tungsten oxide (PdWO3). Sensor Actuator B Chem 2013;187:84–93. https://doi.org/10.1016/j.snb.2012.09.063. http://www.sciencedirect.com/science/article/pii/S0925400512009768.
[17] Yang C, Cao X, Wang S, Zhang L, Xiao F, Su X, et al. Complex-directed hybridization of CuO/ZnO nanostructures and their gas sensing and photocatalytic properties. Ceram Int 2015;41(1):1749–56. https://doi.org/10.1016/j.ceramint.2014.09.120. https://doi.org/10.1016%2Fj.ceramint.2014.09.120.
[18] Liu Y, Yu J, Lai P. Investigation of WO3/ZnO thin-film heterojunction-based Schottky diodes for H2 gas sensing. Int J Hydrogen Energy 2014;39(19):10313–9. https://doi.org/10.1016/j.ijhydene.2014.04.155. https://doi.org/10.1016%2Fj.ijhydene.2014.04.155.
[19] Liu Y, Lai PT, Tang WM. Improved hydrogen-sensing performance of Pd/WO3/SiC Schottky diode by La doping. In: 2016 IEEE international conference on electron devices and solid-state circuits (EDSSC). IEEE; 2016. p. 338–41. https://doi.org/10.1109/EDSSC.2016.7785277. http://ieeexplore.ieee.org/document/7785277/.
[20] Geng X, Luo Y, Zheng B, Zhang C. Photon assisted room-temperature hydrogen sensors using PdO loaded WO3nanohybrids. Int J Hydrogen Energy 2017;42(9):6425–34. https://doi.org/10.1016/j.ijhydene.2016.12.117. https://doi.org/10.1016/j.ijhydene.2016.12.117.
[21] Shelemin A, Kylián O, Hanuš J, Choukourov A, Melnichuk I, Serov A, et al. Preparation of metal oxide nanoparticles by gas aggregation cluster source. Vacuum 2015;120:162–9. https://doi.org/10.1016/j.vacuum.2015.07.008. https://doi.org/10.1016%2Fj.vacuum.2015.07.008.
[22] Shyjumon I, Gopinadhan M, Helm CA, Smirnov BM, Hippler R. Deposition of titanium/titanium oxide clusters produced by magnetron sputtering. Thin Solid Films 2006;500(1–2):41–51. https://doi.org/10.1016/j.tsf.2005.11.006. https://doi.org/10.1016%2Fj.tsf.2005.11.006.
[23] Kuzminova A, Beranová J, Polonskyi O, Shelemin A, Kylián O, Choukourov A, et al. Antibacterial nanocomposite coatings produced by means of gas aggregation source of silver nanoparticles. Surf Coating Technol 2016;294:225–30. https://doi.org/10.1016/j.surfcoat.2016.03.097. https://doi.org/10.1016%2Fj.surfcoat.2016.03.097.
[24] Polonskyi O, Solař P, Kylián O, Drábik M, Artemenko A, Kousal J, et al. Nanocomposite metal/plasma polymer films prepared by means of gas aggregation cluster source. Thin Solid Films 2012;520(12):4155–62. https://doi.org/10.1016/j.tsf.2011.04.100. https://doi.org/10.1016%2Fj.tsf.2011.04.100.
[25] Bai S, Guo W, Sun J, Li J, Tian Y, Chen A, et al. Synthesis of SnO 2 –CuO heterojunction using electrospinning and application in detecting of CO. Sensor Actuator B Chem 2016;226:96–103. https://doi.org/10.1016/j.snb.2015.11.028. https://doi.org/10.1016%2Fj.snb.2015.11.028.
[26] Marek A, Valter J, Kadlec S, Vyskočil J. Gas aggregation nanocluster source Reactive sputter deposition of copper and titanium nanoclusters. Surf Coating Technol 2011;205:S573–6. https://doi.org/10.1016/j.surfcoat.2010.12.027.
[27] Mašek K, Blumentrit P, Beran J, Skála T, Píš I, Libra J, et al. Pt-doped tungsten oxide surface: photoemission and RHEED study. Surf Interface Anal 2010;42(6–7):540–4. https://doi.org/10.1002/sia.3362.
[28] Mašek K, Libra J, Skála T, Cabala M, Matolín V, Cháb V, et al. SRPES investigation of tungsten oxide in different oxidation states. Surf Sci 2006;600(8):1624–7. https://doi.org/10.1016/j.susc.2005.11.048. https://doi.org/10.1016%2Fj.susc.2005.11.048.
[29] Parmigiani F, Sangaletti L. The Cu2p X-ray photoelectron core-lines in copper oxide based high temperature superconductors. J Electron Spectrosc Relat Phenom 1994;66:223–39.
[30] Akter N, Wang M, Zhong J-Q, Liu Z, Kim T, Lu D, et al. Stabilization of oxidized copper nanoclusters in confined spaces. Top Catal 2018;61(5–6):419–27. https://doi.org/10.1007/s11244-017-0879-9. https://doi.org/10.1007%2Fs11244-017-0879-9.
[31] Esfandiar A, Irajizad A, Akhavan O, Ghasemi S, Gholami MR. Pd-WO3/reduced graphene oxide hierarchical nanostructures as efficient hydrogen gas sensors. Int J Hydrogen Energy 2014;39(15):8169–79. https://doi.org/10.1016/j.ijhydene.2014.03.117. https://doi.org/10.1016/j.ijhydene.2014.03.117.
[32] Zhao M, Huang J, Ong C-W. Feasibility of H2 sensors composed of tungsten oxide nanocluster films. Int J Hydrogen Energy 2013;38(35):15559–66. https://doi.org/10.1016/j.ijhydene.2013.09.069. http://www.sciencedirect.com/science/article/pii/S0360319913022921.
[33] Jolly Bose R, Illyaskutty N, Tan KS, Rawat RS, Matham MV, Kohler H, et al. Hydrogen sensors based on Pt-loaded WO_3 sensing layers. EPL (Europhysics Letters) 2016;114(6):66002. https://doi.org/10.1209/0295-5075/114/66002. http://stacks.iop.org/0295-5075/114/i=6/a=66002?key=crossref.6cc057e93f38ad1030117307ce5f3674.
[34] De Marcellis A, Ferri G, Mantenuto P, Giancaterini L, Cantalini C. WO3 hydrogen resistive gas sensor and its wide-range current-mode electronic read-out circuit. IEEE Sensor J 2013;13(7):2792–8. https://doi.org/10.1109/JSEN.2013.2257732.
[35] Fardindoost S, Iraji zad A, Hosseini ZS, Hatamie S. Detecting hydrogen using graphene quantum dots/WO_3 thin films. Mater Res Express 2016;3(11):116407. https://doi.org/10.1088/2053-1591/3/11/116407. http://stacks.iop.org/2053-1591/3/i=11/a=116407?key=crossref.f7a59476370d880f4113048f7a144d7c.
[36] Mattoni G, de Jong B, Manca N, Tomellini M, Caviglia AD. Single-crystal Pt-decorated WO_3 ultrathin films: a platform for sub-ppm hydrogen sensing at room temperature. ACS Applied Nano Materials 2018. https://doi.org/10.1021/acsanm.8b00627. acsanm.8b00627, http://pubs.acs.org/doi/10.1021/acsanm.8b00627.
[37] Roy K, Gopinath CS. UV photoelectron spectroscopy at near ambient pressures: mapping valence band electronic structure changes from Cu to CuO. Anal Chem 2014;86(8):3683–7. https://doi.org/10.1021/ac4041026. http://pubs.acs.org/doi/10.1021/ac4041026.
[38] Álvarez-Falcón L, Viñes F, Notario-Estévez A, Illas F. On the hydrogen adsorption and dissociation on Cu surfaces and nanorows. Surf Sci 2016;646:221–9. https://doi.org/10.1016/J.SUSC.2015.08.005. https://www.sciencedirect.com/science/article/pii/S0039602815002253.

B

Nanostructured $CuWO_4/WO_{3-x}$ Films Prepared by Reactive Magnetron Sputtering for Hydrogen Sensing

N. Kumar, J. Čapek, S. Haviar

International Journal of Hydrogen Energy 45 (2020) 18066-18074

Available online at www.sciencedirect.com

ScienceDirect

journal homepage: www.elsevier.com/locate/he

Nanostructured $CuWO_4/WO_{3-x}$ films prepared by reactive magnetron sputtering for hydrogen sensing

Nirmal Kumar, Jiří Čapek, Stanislav Haviar *

Department of Physics and NTIS-European Centre of Excellence, University of West Bohemia, Univerzitni 8, 301 00, Pilsen, Czech Republic

HIGHLIGHTS

- Two-step reactive sputter deposition used for $CuWO_4/WO_{3-x}$ bilayer films synthesis.
- Nanostructured $CuWO_4$ islands were formed on top of WO_3 thin film.
- $CuWO_4/WO_{3-x}$ tested for the H_2 gas response for the first time.
- Sensing mechanism based on the formation of nano-sized *n-n* junction is proposed.
- Only dry techniques were employed for deposition → high-purity films were prepared.

GRAPHICAL ABSTRACT

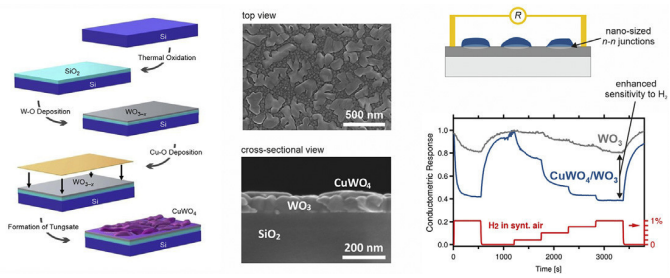

ARTICLE INFO

Article history:
Received 2 October 2019
Received in revised form
16 April 2020
Accepted 23 April 2020
Available online 29 May 2020

ABSTRACT

High-purity films consisting of copper tungstate ($CuWO_4$) and sub-stoichiometric tungsten oxide (WO_{3-x}) were prepared by reactive sputter deposition. An original two-step deposition process was applied for their synthesis. First, a tungsten oxide thin film was deposited by dc magnetron sputtering from a W target in an Ar + O_2 gas mixture, afterward, rf sputtering of a Cu target in an Ar + O_2 gas mixture was employed to form a discontinuous $CuWO_4$ layer at the top. This results in a formation of nanostructured branched islands of the tungstate. Bilayers with various layer thicknesses were investigated for the sensitivity to hydrogen gas as a conductometric sensor. The sensitivity changes remarkably with the thicknesses of individual layers. The maximum sensitivity was observed for the films with a layer thickness ratio of 5 nm/20 nm. The response was enhanced more than eight times compared to a 20 nm-thick tungsten oxide alone film. An explanation based on the formation of nano-sized *n-n* junctions is provided. In addition, a microscopy study of the bilayer growth is presented in detail.

* *Corresponding author.*
E-mail addresses: haviar@ntis.zcu.cz, stanislav.haviar@gmail.com (S. Haviar).
https://doi.org/10.1016/j.ijhydene.2020.04.203

Introduction

Rapidly growing hydrogen industry has stimulated research of new materials for sensing of the hydrogen gas. Mostly, metal oxide semiconductors (MOS) have been investigated as suitable sensing materials in the last decades. This is mainly due to a large variety of composition and band gap properties and, the possibility of forming nanostructured active surfaces [1]. The research has been mainly focused on binary oxides, either *n*-type (SnO_2, ZnO, TiO_2, WO_3, In_2O_3, …) or *p*-type semiconductors (CuO, NiO, …) [2]. However, rapidly developing hydrogen technologies demand new advanced materials exhibiting enhanced response characteristics, *i.e.*, sensitivity, selectivity, fast response and recovery time, good temperature and chemical stability, and low working temperature. This requires the application of new approaches and methods. Novel materials based on ternary oxides (*e.g.*, Bi_2WO_6, $ZnWO_4$, ZrW_2O_8, $NiWO_4$, and $CuWO_4$) or even their combination with other oxides (this work) are promising research directions in this field. Aforementioned tungstate materials are candidates of interest due to their suitable band gap (2.3 eV), and adequate thermal stability [3]. $CuWO_4$ is highly chemically stable due to the presence of hybrid Cu-3d and O-2p orbitals and it has a low cost of preparation and limited toxicity [4].

Tungsten trioxide (WO_3), as a prominent sensorial material that has attracted much attention [5–10] in last decades. Further improvement of its sensorial characteristics can be done by combining with other binary oxides [11] or by combining with ternary oxides, *e.g.*, copper tungstate $CuWO_4$.

The $CuWO_4/WO_3$ material system has been investigated in several works [3,12,13]. However, this system has been prepared by wet techniques with a relatively high level of impurities and limited control of the elemental composition, structure, and properties of the prepared materials. The used techniques also frequently produce bulk heterojunctions between $CuWO_4$ and WO_3 nanocrystalline particles rather than more suitable nano-sized heterojunctions. Besides, none of these studies has been investigated these materials for hydrogen sensing.

Reactive magnetron sputtering is versatile and environmentally friendly (no harmful chemicals and gases are used) technique suitable for the preparation of high-purity thin-film materials with a possibility to control their elemental composition and structures in a wide range. This technique is suitable for an integration of the prepared materials into micro-circuits.

In this work, we demonstrate the use of reactive magnetron sputtering for preparing nanostructured $CuWO_4/WO_{3-x}$ bilayer films, where the top discontinuous layer of copper tungstate partially covers the slightly sub-stoichiometric tungsten oxide (x~0.05). We investigated the sensorial behavior of as-prepared films with a changing structure and we explain the enhancement of the sensorial response of $CuWO_4/WO_{3-x}$ system based on detailed SEM imaging, X-ray diffraction analysis, and Raman spectroscopy. To our knowledge, this is the first work focused on hydrogen sensorial properties of the $CuWO_4/WO_{3-x}$ system.

Experimental details

Film preparation

To synthesize $CuWO_4/WO_{3-x}$ nanostructured bilayers, the tungsten oxide and cupric oxide thin films were deposited sequentially on 9 × 9 mm^2 thermally oxidized Si(100) substrates by reactive sputtering. For depositions of both films, the substrate temperature, working gas composition and applied power were optimized in order to achieve the desired crystalline structure.

The substrates were cleaned by sonification for 10 min in isopropyl alcohol and 5 min in deionized water and dried by nitrogen blow. A cylindrical sputtering chamber, parallel to the ground, with a volume of 25 l and diameter of 42 cm (Leybold-Heraeus LH Z400) was pumped by a turbomolecular pump (690 l/s for N_2) backed with a scroll pump. The base pressure before each deposition was lower than 2×10^{-3} Pa. As a working gas, the mixture of argon and oxygen was used. The pressure of 0.7 Pa of argon gas was set prior to the adding of the reactive gas for both depositions. For WO_3 and CuO thin film depositions, the ratio of O_2:Ar was set 1:3 and 1:4 respectively. The substrates were placed at a distance of 70 mm from the targets and the substrates were heated to 400 °C for both films.

Tungsten oxide was deposited using a 75-mm metallic target using a magnetron operated in dc mode at 60 W. CuO deposition was carried out using cathode sputtering (no magnets) in rf mode at 228 W (dc potential of 2.2 kV). The deposition rates of WO_{3-x} and CuO layers were 35 and 25 nm/min, respectively.

From now onwards, we denote the prepared films as the bilayer films with the thickness of individual layers indicated by the upper index. For example, the film formed by depositing of 10 nm of CuO on the top of 20 nm of WO_{3-x} is labeled as ^{10}Cu–O/^{20}W–O. Also, for the sake of clarity, where it is possible, we describe the reactive deposition of copper as the deposition of CuO, even if it would be more precise to distinguish the material added by reactive deposition (Cu–O) and formed solid film CuO.

Film characterization

The film thicknesses (and the corresponding deposition rate) were precisely determined by atomic force microscope (AFM) imaging on a steep step formed due to a partially covered substrate with a varnish during the deposition (available in Fig. A1 in Appendix).

X-ray diffraction (XRD) measurements of the films were carried out using a diffractometer (X'Pert PRO PANanalytical) with Cu K_α source of radiation in the Bragg-Brentano configuration. In addition to the XRD measurements, the phase composition was confirmed by Raman spectroscopy (Horiba Jobin Yvon LABRAM HR Evolution) using a 532 nm laser.

The top-view morphologies and the cross-sections of the films were studied using Scanning Electron Microscope (SEM, Horiba SU-70, secondary electron image at 5 kV). The cross-sections of the films were prepared by the simple breaking

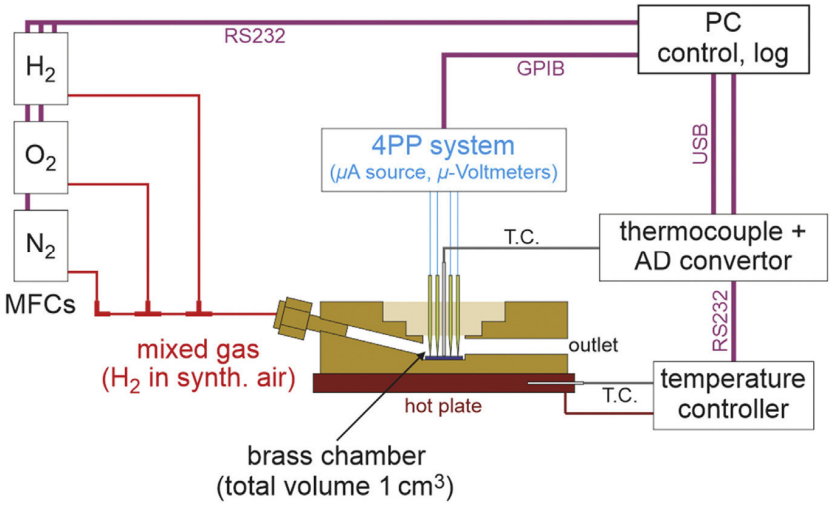

Fig. 1 – Schematic of the custom-built system for the measurement of gas response.

of the pre-scratched Si substrate with the deposited films. This allows to observe the structure of the films through the individual layers as well as to confirm the thickness of the deposited films measured by AFM.

The gas response was measured by a custom-built system utilizing the four-point probe technique for the measurement of the film resistivity in a defined gas mixture (H_2 + synthetic air) and at a precisely controlled temperature (as shown in Fig. 1). The measurements were carried out in a cylindrical reaction chamber (a total volume of 1 cm^3) in a flow-mode. Four gold-plated spring-loaded pins with 1-mm spacing were pressed to the specimen surface resulting in stable electrical contacts. The heating source under the chamber was used to measure the sensorial response at elevated temperatures. The temperature of the specimen surface was measured by an independent 0.3 mm thin thermocouple pressed to the top surface. Three mass flow controllers (Alicat Scientific) with ranges of 10, 100 and 200 sccm were used to mix H_2, O_2, and N_2 gases, respectively. The resulting gas mixture was introduced into the chamber in a flow mode at a total flow rate of 100 sccm. The electrical measurement was governed by a DC source (KEITHLEY 6220) and two electrometers (KEITHLEY 6514). The whole system was fully driven by a LabVIEW based control software which enables precise recording of the film resistance at various temperatures and H_2 concentrations.

In this text, we define the sensitivity S at a specified concentration c and temperature T as:

$$S(c,T) = \frac{\Delta R}{R_i} \quad (1)$$

$$\Delta R = |R_a - R_g| \quad (2)$$

Where R_a and R_g are the resistance in the presence of synthetic air and H_2 gas mixed with air, respectively. R_i corresponds to R_a or R_g for n-type materials or p-type material, respectively [1]. The values of R_a and R_g are obtained by fitting the data which fitted by a sum of two exponential decays in respect of Eq. (2) in Ref. [14].

Results and discussion

In this part, we first investigate the structure (Sec. Structure of films) and morphology (Sec. Morphology of films) of the prepared films. Subsequently, we discuss the growth process of $CuWO_4/WO_{3-x}$ films based on the presented findings (Sec. Growth process of $CuWO_4/WO_{3-x}$ films). Finally, we investigate (Sec. Sensorial behavior – measurement) and discuss (Sec. Sensorial behavior – discussion) the sensorial behavior of the prepared films.

Structure of films

XRD patterns of the WO_{3-x} and CuO layers alone (Fig. 2a) indicate that a tetragonal $WO_{2.95}$ (PDF Card No. 04-013-0875) and monoclinic (PDF Card No. 04-007-1375) phases are formed during the one-step deposition process, respectively.

In the case of the two-step deposition, the situation is more complex. During the second deposition, the added materials (Cu atoms and oxygen species) react with the pre-deposited WO_{3-x} layer that leads to a formation of a triclinic copper tungstate $CuWO_4$ phase (PDF Card. No 01-073-1823). As the amount of the added Cu–O increases the signal corresponding to the $CuWO_4$ phase rises, while the signal from the WO_{3-x} phase diminishes. Finally, for an appropriate ratio of both materials (^{20}Cu–O/^{20}W–O), the WO_{3-x} phases completely reform into the $CuWO_4$ phase. Further addition of the deposited Cu–O leads to the formation of the CuO phase on the top of the $CuWO_4$ phase (not presented here).

In Fig. 2c we demonstrate two important facts. First, the phase composition is very similar for the ^{5}Cu–O/^{20}W–O and ^{20}Cu–O/^{80}W–O films prepared with the same Cu–O/W–O

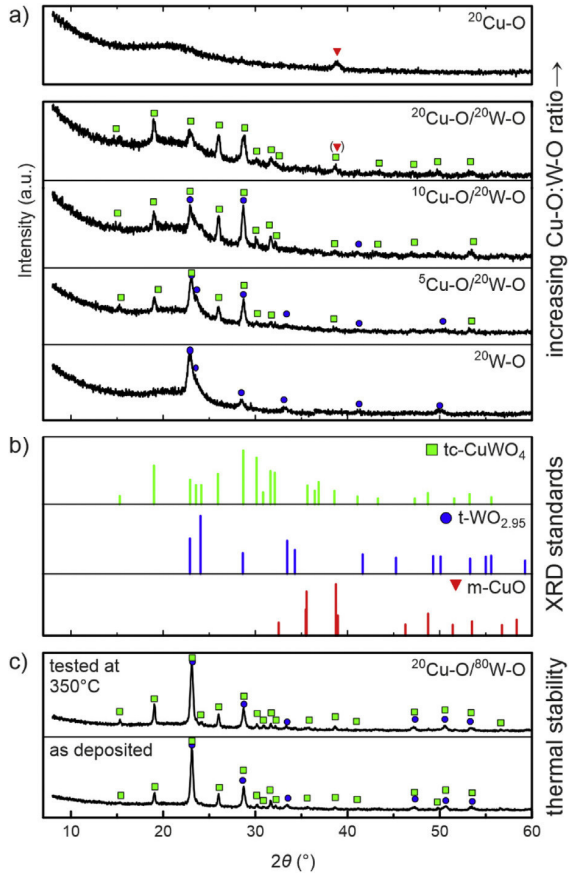

Fig. 2 – XRD patterns of W–O and Cu–O layers alone (a) and prepared bilayer films (c) used for sensorial behavior investigation, of the as-deposited and annealed ^{20}Cu–O/^{80}W–O films used for morphology investigation (b) and used XRD standards.

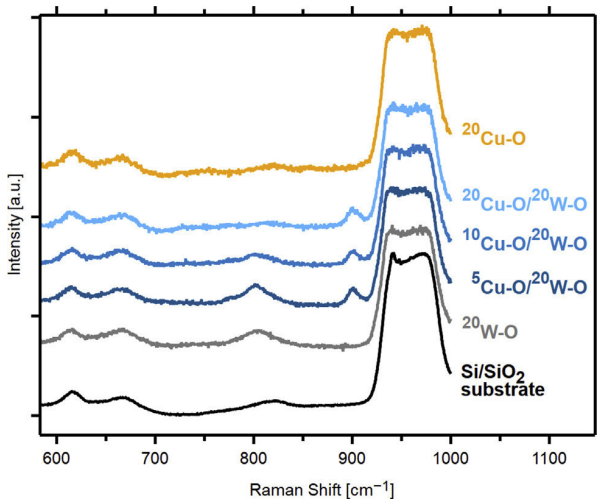

Fig. 3 – Raman spectra of prepared films and clean substrate. The main broad feature is attributed to the Si/SiO$_2$ substrate, see text for further comments.

ratio, but with a significantly different total film thickness (25 nm vs. 100 nm, respectively). Second, the phase structure of the film is stable at the working temperature of the sensor (tens of hours at 350 °C) as can be seen by comparing the as-deposited and tested, *i.e.* heated, films.

The grain size of the ^{80}W–O layer was calculated as 27 nm (pattern not shown) using the Debye-Scherrer formula and the grain size increases with adding of the CuO layer up to 37 nm for ^{20}Cu–O/^{80}W–O. In the case of thinner films (^{xx}Cu-O/^{20}W–O), the grain sizes of $CuWO_4$ were 46, 48 and 39 nm (FWHM = 0.183, 0.175 and 0.216°) for 5, 10 and 20 nm of Cu–O on 20 nm W–O, respectively. The changes in grain size are discussed later.

The evolution of the phase composition revealed by XRD analysis is in good agreement with the Raman spectroscopy measurements. In Fig. 3 the evolution of the spectra on prepared films is visible. The tungsten oxide monoclinic phase is indicated by a peak at 804 cm^{-1} attributed to the W–O mode [15]. The peak at 900 cm^{-1} corresponds to the symmetric stretching of W–O mode for regular octahedron (WO_6) confirming the $CuWO_4$ phase according to Refs. [4,15]. The other referenced exclusive peak of this phase (973 cm^{-1}) is difficult to observe due to the overlap with the broad intense spectral feature of the substrate. Other peaks visible in Fig. 3 (615, 666 and 819 cm^{-1}) are to be attributed to SiO_2. It is necessary to mention that no peaks are indicating the copper oxide on Cu–O/W–O films.

Morphology of films

The morphology of the prepared films is documented by SEM micrographs in Fig. 4. In the first row of micrographs (Fig. 4a), one can see an evolution of the topography and cross-section of 20 nm thick WO_{3-x} layers covered by gradually increased thickness of the Cu–O layers. The addition of Cu–O to the surface in the case of the ^{5}Cu–O/^{20}W–O film leads to a formation of clearly visible islands. These islands are branched-shaped with a typical width and length of individual branches of approximately 100 nm and several hundreds of nanometers, respectively. A further increase in the amount of the added material (^{10}Cu–O/^{20}W–O film) leads to more narrow gaps in between the islands. Finally, the surface is almost completely over-covered by the islands in the case of the ^{20}Cu–O/^{20}W–O film.

Interestingly, similar behavior is observed for 80 nm WO_{3-x} layers (see Fig. 4b). The cross-sectional views indicate a substantial gradual increase in the surface roughness due to the formation of the islands.

One can also notice that all the WO_{3-x} layers are characterized by visible grain boundaries and that the grain size of these layers increases with the addition of the Cu–O layer. This phenomenon can be attributed to the elevated

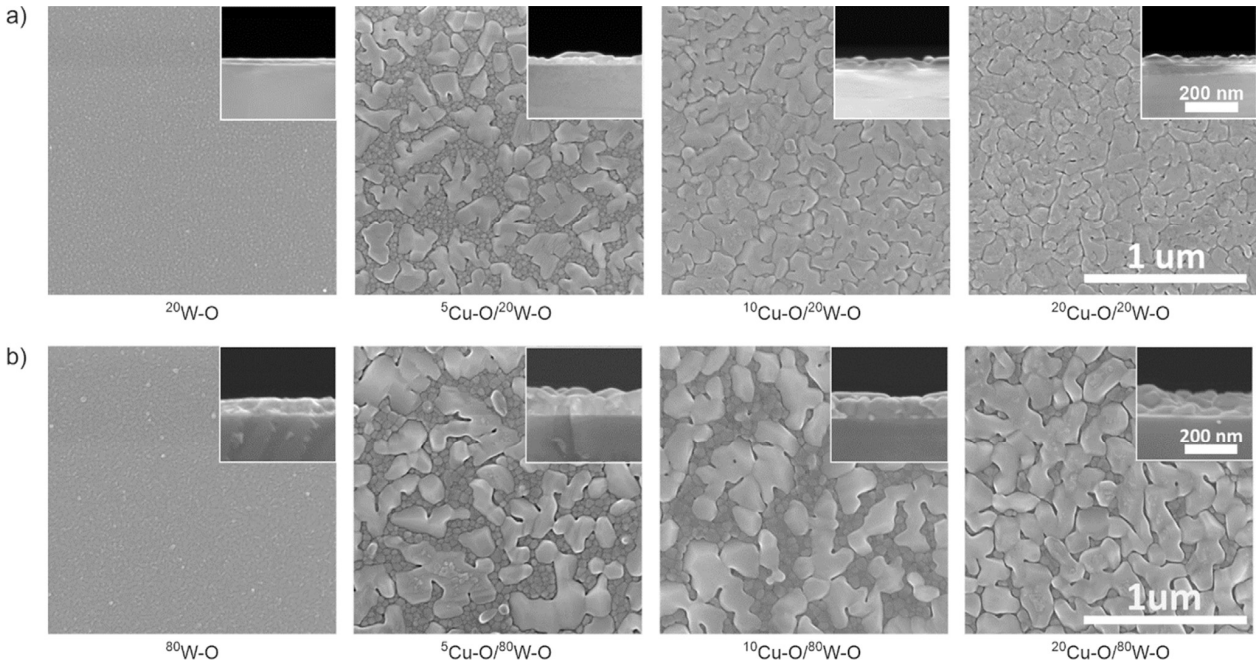

Fig. 4 – SEM top-view micrographs of prepared films with 20 nm (a) and 80 nm (b) of WO_{3-x} layers with an increasing (from left to the right) thickness of the Cu–O layer deposited on top. The cross-sectional views in the insets of micrographs were prepared by the simple breaking of the substrate.

temperature of 400 °C during the deposition of Cu–O layers. During this process, the WO_{3-x} layer is annealed under oxygen plasma and therefore the presumably crystalline grains grow in size. This rise in grain size was also confirmed by the analysis of the corresponding XRD patterns. However, a quantitative comparison of these two techniques is not possible since the XRD and the SEM techniques determine the vertical and horizontal dimensions of the grains, respectively. The cross-sectional SEM views, unfortunately, provide poor contrast and more importantly insufficient statistics for an evaluation of the grain size.

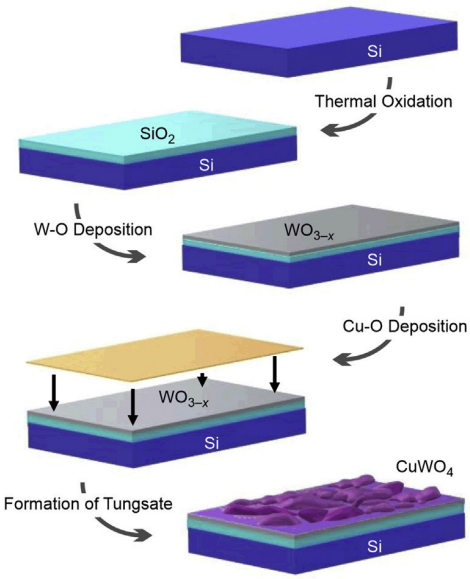

Fig. 5 – A sketch of the growth process of nanostructured $CuWO_4/WO_{3-x}$ bilayers. Description in the text.

Growth process of $CuWO_4/WO_{3-x}$ films

A simple description of the growth process can be formulated based on the results from the XRD and the SEM analyses. Sputtering of a W target in an Ar + O_2 working gas mixture leads to the deposition of a dense and smooth WO_{3-x} layer. Subsequently, the top-most part of this film reacts with the arriving adatoms during the sputtering of a Cu target in a similar gas mixture leading to the formation of the $CuWO_4$ islands. The sketch of the process is in Fig. 5.

The detailed SEM cross-sectional views in Fig. 6 clearly demonstrate the main features of the formed $CuWO_4/WO_{3-x}$ film. Here, the $CuWO_4$ phase forms wide (in planar plane) islands that overly the WO_{3-x} grains.

A simple estimation of an optimum CuO film thickness allowing the complete transformation of the WO_{3-x} into $CuWO_4$ follows. We can estimate that the amount of delivered Cu atoms during the reactive sputtering of Cu target on top of the WO_{3-x} layer is the same as while depositing the CuO layer onto a bare substrate. Then, we can consider the density of Cu and W atoms in CuO and WO_{3-x} layers to be 0.023 mol/cm^3 and 0.040 mol/cm^3, respectively. Since there is a 1:1 ratio of metallic cations in $CuWO_4$, the complete reformed layer of $CuWO_4$ would be formed by depositing a film with the appropriate ratio of corresponding layer thicknesses of 0.6. Such a bilayer would be denoted as ^{12}Cu–O/^{20}W–O. The XRD plots in Fig. 2a confirm that the film ^{10}Cu–O/^{20}W–O is not

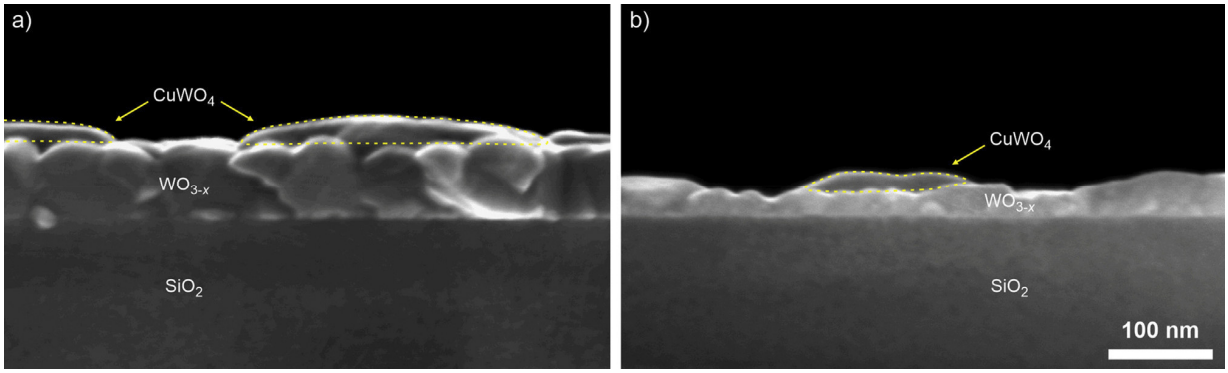

Fig. 6 – SEM cross-sectional micrographs of the a) ^{10}Cu–O/^{80}W–O film and b) ^{5}Cu–O/^{20}W–O. The morphology of the top $CuWO_4$ phase clearly does not follow the structure of the bottom tungsten oxide layer which helps to identify the other phase.

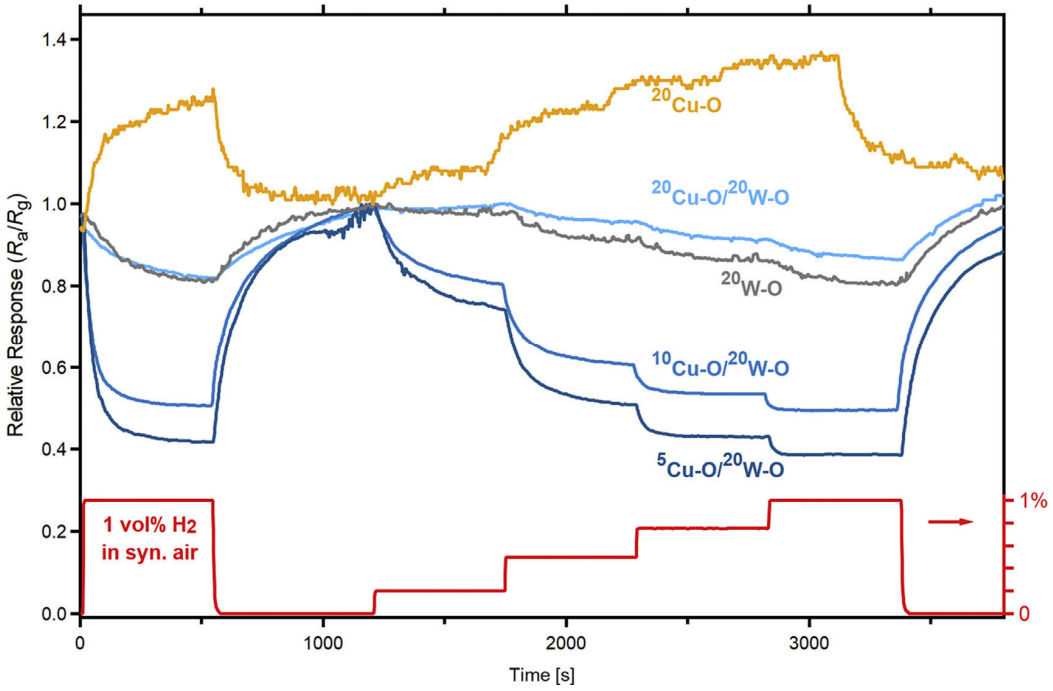

Fig. 7 – Relative response of the prepared films as a function of time for the concentration of hydrogen in the synthetic air modulated from 0.2 vol% up to 1.0 vol%. The temperature of the films was 350 °C.

completely reformed into $CuWO_4$. At the same time, the ^{20}Cu–O/^{20}W–O film does not exhibit any signal from the $WO_{2.95}$ phase. Since the ratio of the layer thicknesses is larger than the appropriate one, a small amount of the CuO phase can also be found in this case (a peak at 38.8°). These assumptions can be applied also to the thicker version of the bilayers on ^{80}W–O. The cross-sectional views in Fig. 4 and XRD results indicate that the deposition temperature of 400 °C helps to reform considerable portion material even though the bottom layer is of a thickness of 80 nm. It must be kept in mind, that these assumptions are based only on the crystalline part of the material. We assume that the XRD amorphous

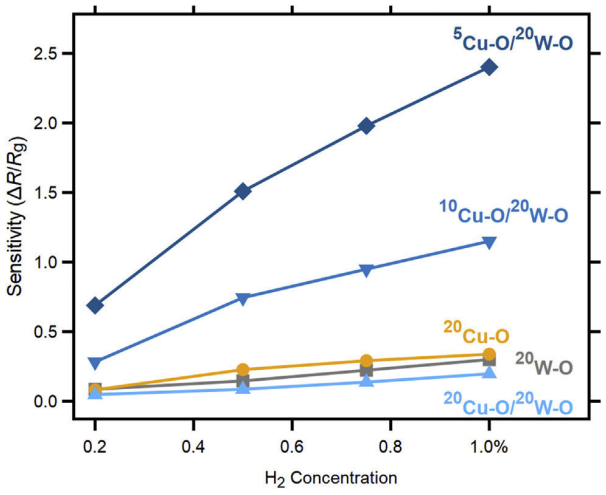

Fig. 8 – Sensitivity plot of selected films for various concentrations of H_2 at a working temperature of 350 °C.

portion of the material is negligible at the deposition temperature used. Therefore, the value of *x* can be assumed to be approximately 0.05 in WO_{3-x}.

Sensorial behavior – measurement

The deposited films were assembled as conductometric gas sensors in order to characterize the sensorial response. As-prepared bilayers were exposed to the hydrogen gas at various temperatures in the presence of synthetic air. Then, the concentration was varied from 0 to 1 vol%.

Since the resistivity differs by orders of magnitude for various bilayers (available in Table A1 in the Appendix), the relative response versus time (*i.e.*, $R(t)/R_a$) is plotted in Fig. 7. In this plot, the responses of films ^{xx}CuO/^{20}W–O (*i.e.*, the bilayers with 20 nm of WO_{3-x} and various thicknesses of CuO) are shown. These are the films imaged in Fig. 4a. Showed responses were acquired at 350 °C.

For WO_{3-x} alone film the response is poor. When a little of CuO is added, the response is enhanced dramatically. Further adding of CuO leads to diminishing the enhancing effect and finally the sample ^{20}Cu–O/^{20}W–O exhibits the lowest response.

In Fig. 7, there is also shown the response of pure cupric oxide film (^{20}Cu–O). Since CuO is a *p*-type semiconductor, the observed response in the opposite manner to WO_{3-x} film.

The numerical evaluation of the sensitivity quantity according to Eq. (1) is plotted for the described films in Fig. 8. It is clearly visible that the enhancement of the sensitivity from pure tungsten oxide film (^{20}W–O) to the most responsive film (^{5}Cu–O/^{20}W–O) from 0.3 to 2.5 (for 1 vol% of H_2 in the synthetic air). It should be noted that these sensitivity values were measured on as-deposited films after short heat-up to the working temperature. After 10-h stabilizing, the sensitivity of ^{5}Cu–O/^{20}W–O raised and settled to a value of 5.0 for the working temperature of 350 °C (shown Fig. A3 in Appendix).

The sensitivity values plot for various temperatures and concentrations for ^{5}Cu–O/^{20}W–O is in Fig. A2.

Table 1 – An overview of achieved results for various MOSs hetero-junction based hydrogen sensors.

Sensing Material and Morphology		Sensitivity S		Temperature [°C]	Concentration [ppm]	References	
		value	Definition				
WO_3	WO_3 thin film	5	R_a/R_{SENS}	150	250	A. De Marcellis et al. (2013)	[22]
WO_3	Pd loaded WO_3 nanocomposites	19	$(R_a-R_g)/R_g$	200	200	A. Boudiba et al. (2013)	[19]
WO_3	Pt loaded WO_3 thin film	~5	$(C_g-C_a)/C_a$	400	500	R. Jolly Bose et al. (2016)	[23]
WO_3	Graphene QDs (GQDs) on WO_3 thin film	1.12	$(R_a-R_g)/R_g$	150	3600	S. Fardindoost et al. (2016)	[5]
Cu-WO_3	Cu-doped WO_3 with photonic Structure	~2	R_a/R_g	290	10	S. Zhu et al. (2010)	[24]
La_2O_3-WO_3	Pd/La_2O_3-WO_3/SiC Schottky diode	8	$(R_a-R_g)/R_g$	200	10,000	Y. Liu et al. (2016)	[25]
CuO-WO_3	CuO nanoclusters on WO_3	2.4	$(R_a-R_g)/R_g$	300	10,000	S. Haviar et al. (2018)	[11]
CuO/ZnO	CuO–ZnO heterocontacts	2.3	I_{H2}/I_a	400	4000	S. Aygun et at. (2005)	[26]
CuO–TiO_2	CuO–TiO_2 Nanocomposites	2–3	$(R_g-R_a)/R_a$	200	1000	D. Barreca et al. (2011)	[27]
CuO/ZnO	CuO–ZnO heterojunction	~267	I_{H2}/I_a	300	3000	S. Mridha et al. (2006)	[28]
CuWO4/WO_{3-x}	CuWO4-WO_{3-x} heterojunction	5.0	$(R_a-R_g)/R_g$	350	10,000	– this work –	

Sensorial behavior – discussion

The general sensing mechanism of hydrogen with MOSs is well described in the literature [1,16–18]. Mainly, the resistance changes due to pre-adsorption of oxygen and subsequent reaction of target gas molecules at the surface. In the case of hydrogen, it reacts with the pre-adsorbed oxygen species such as O^-, O^{2-}, O_2^- and O_2^{2-} producing water. In the case of *n*-type, the interaction with hydrogen results in increasing the conductivity since the electron from the oxygen species is returned back to the material. Electrons are returned back to the semiconductor, the depletion zone is reduced and the conductivity is increased [1,11,19].

However, when the WO_{3-x} layer is overlayered by islands of $CuWO_4$, the mechanism becomes more complicated due to the formation of $CuWO_4$–WO_{3-x} *n*-*n* heterojunctions [3]. In this case, an electron depletion layer at the interface is formed [18,20]. This results in higher resistance of the film as compared to the WO_{3-x} alone as also observed in this work ($CuWO_4/WO_{3-x}$ has a higher resistance than the WO_{3-x} and the $CuWO_4$ layers alone, see Table A1). When the $CuWO_4/WO_{3-x}$ film is exposed to H_2, the gas reacts with the pre-adsorbed oxygen species (as described above), which leads to a change in the volume of the depletion zone. It is not important that the $CuWO_4$ films are discontinuous because the reduction of the conductive channel is present at the interface of the tungsten oxide and copper tungstate. The effective conductive channel is though reduced initially and changes stimulated by adsorption of hydrogen are then more profound. In fact, the non-percolating structure of copper tungstate is important, since the compact film of tungstate would form another parallel conductive channel and disable the sensorial reaction. This explanation is in good agreement with similar system [21] forming *n*-*n* heterojunctions (WO_3/ZnO) but tested towards oxidizing NO_2.

A quantitative comparison of the sensorial behavior of the prepared films with other related works is difficult due to frequently significantly dissimilar conditions during material testing. Therefore, an overview of similar architectures and combinations of MOS materials including their performances with respect to the hydrogen gas is presented in Table 1. The performance of the material presented in this paper is also listed.

Conclusions

In this paper, we demonstrated the possibility to prepare the nanostructured bilayer films composed of WO_{3-x} and $CuWO_4$ (on top) layers and we investigated the properties of these films with respect to hydrogen sensing.

The films were prepared by successive deposition of WO_{3-x} and CuO layers using a reactive sputtering technique. During the sputtering of the Cu target, Cu atoms from the deposition flux together with the reactive species (O_2 and O) reacted with the WO_{3-x} layer. This phenomenon led to a formation of the $CuWO_4$ phase on the top of the WO_{3-x} layer. A transition from Cu–O/W–O to $CuWO_4/WO_{3-x}$ occurred due to the heating at 400 °C during the second deposition of Cu–O. In addition, an appropriate amount of deposited Cu atoms allowed the formation of $CuWO_4$ islands with a typical size of about 100 nm.

The prepared films were further investigated as materials for the conductometric sensing of hydrogen. It was found that sensitivity of the WO_{3-x} film was significantly (more than eight times) enhanced by adding the nanostructured $CuWO_4$ material on the top. This improvement was attributed to the formation of *n*-*n* heterojunctions between the two materials and higher surface to volume ratio. In such a case, increment in the adsorption sites is occurred and enhanced the gas sensitivity.

For a better understanding of the sensing mechanism and the sensorial potential of examined materials, it is planned to perform cross-sensitivity measurements for other reducing gases, such as methane, CO_2, CO, acetone, methanol or ethanol. Without the information about the selectivity, one should consider the presented sensitivity to hydrogen as a demonstration of an ability of the $CuWO_4/WO_3$ system to sense reducing gases, yet we believe the system could be selective to hydrogen gas at certain temperatures or, typically, with use of a proper catalyst (Pd).

In this work, we focused on the synthesis of nanostructured $CuWO_4$. In our future work, we will focus also on further investigation of the sputtering deposition-specific possibilities of modifying the nanostructured MOSs with heterostructures. Currently, experiments in preparing other material combinations and various multilayer architectures using the described method are conducted.

Acknowledgements

The authors would like to thank dr. R. Čerstvý for conducting the XRD measurements. The authors also appreciate useful comments by prof. P. Zeman. This work was supported by the Czech Science Foundation under Project No. GA19-13174S.

Appendix A

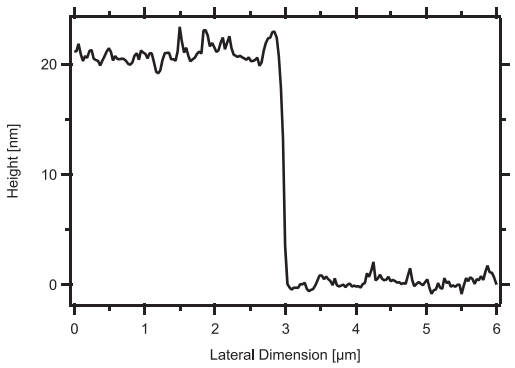

Fig. A1 – AFM scan over a step made in the deposited film in order to measure the thickness. Example of a ^{20}W–O sample.

Table A1 – Summary of properties of the investigated films measured at working temperature of 350 °C. Resistance R_a was measured in pure synthetic air, film sensitivity was evaluated for 1 vol% H_2 in synthetic air, response time of the films was obtained by fitting the reaction curve by a sum of two exponential decays. The resistivity ρ is calculated assuming a homogeneous thin film. Yet this is not true for presented films these approximate values can be used for further comparison of the specimens.

Film	R_a [× 10^6 Ω]	ρ [× 10^4 Ωm]	Sensitivity ($S = \Delta R/R_g$)	Response time [s]
^{20}W–O	1.17	1.62	0.30	354
^{20}Cu–O	0.0136	0.0188	0.34	224
^{20}Cu–O/^{20}W–O	1.22	3.38	0.20	586
^{10}Cu–O/^{20}W–O	6.24	12.97	1.2	120
^{5}Cu–O/^{20}W–O	11.0	17.57	2.5	122

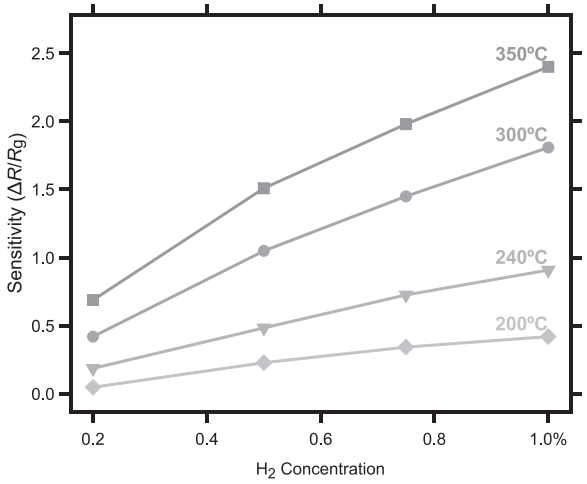

Fig. A2 – Sensitivity plot of the ^{5}CuO/^{20}WO$_3$ film for various concentrations of H_2 and temperatures.

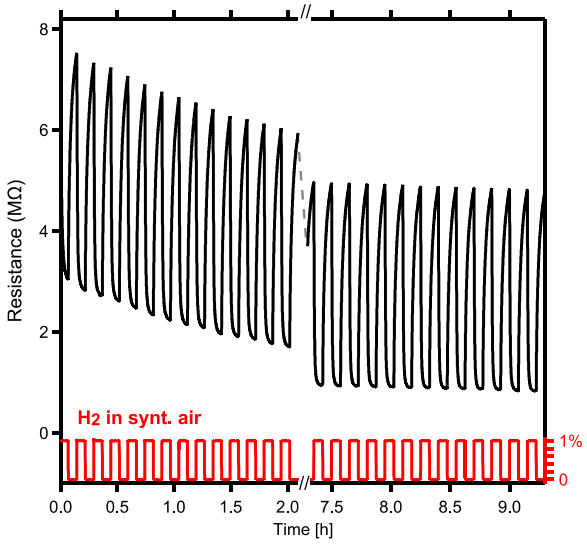

Fig. A3 – A long-term stability measurements of the ^{5}Cu–O/^{20}W–O specimen.

REFERENCES

[1] Moseley PT. Meas Sci Technol 2017;28.
[2] Maziarz W. Appl Surf Sci 2019;480:361–70.
[3] Zhan F, Li J, Li W, et al. Int J Hydrogen Energy 2015;40:6512–20.
[4] Salimi R, Sabbagh Alvani AA, Mei BT, et al. New J Chem 2019;43:2196–203.
[5] Fardindoost S, Iraji zad A, Hosseini ZS, et al. Mater Res Express 2016;3:116407.
[6] Ranjbar M, Fardindoost S, Mahdavi SM, et al. Sol Energy Mater Sol Cells 2011;95:2335–40.
[7] Kalanur SS, Heo J, Yoo IH, et al. Int J Hydrogen Energy 2017;42:16901–8.
[8] Al-Hardan NH, Abdullah MJ, Aziz AA. Int J Hydrogen Energy 2010;35:4428–34.
[9] Ahmad MZZ, Golovko VBB, Adnan RHH, et al. Int J Hydrogen Energy 2013;38:12865–77.
[10] Zappa D, Bertuna A, Comini E, et al. Anal. Methods 2015;7:2203–9.
[11] Haviar S, Čapek J, Batková Š, et al. Int J Hydrogen Energy 2018;43:22756–64.
[12] Yourey JE, Kurtz JB, Bartlett BM. J Phys Chem C 2012;116:3200–5.
[13] Chen H, Xu Y. RSC Adv 2015;5:8108–13.
[14] Haviar S, Chlupová Š, Kúš P, et al. Int J Hydrogen Energy 2017;42:1344–52.
[15] Thongpan W, Louloudakis D, Pooseekheaw P, et al. Mater Lett 2019;257:126747.
[16] Feng C, Li X, Ma J, et al. Sensor Actuator B Chem 2015;209:622–9.
[17] Xu H, Ju J, Li W, et al. Sensor Actuator B Chem 2016;228:634–42.
[18] Tomer VK, Devi S, Malik R, et al. Sensor Actuator B Chem 2016;229:321–30.
[19] Boudiba A, Roussel P, Zhang C, et al. Sensor Actuator B Chem 2013;187:84–93.
[20] Zhang J, Liu X, Xu M, et al. Sensor Actuator B Chem 2010;147:185–90.
[21] Sun J, Sun L, Han N, et al. Sensor Actuator B Chem 2019;285:68–75.
[22] De Marcellis A, Ferri G, Mantenuto P, et al. IEEE Sensor J 2013;13:2792–8.
[23] Jolly Bose R, Illyaskutty N, Tan KS, et al. Europhys Lett 2016;114:66002.
[24] Zhu S, Liu X, Chen Z, et al. J Mater Chem 2010;20:9126–32.
[25] Liu Y, Lai PT, Tang WM. In: IEEE international conference electron devices solid-state circuits. IEEE; 2016. p. 338–41.
[26] Aygün S, Cann D. Sensor Actuator B Chem 2005;106:837–42.
[27] Barreca D, Carraro G, Comini E, et al. J Phys Chem C 2011;115:10510–7.
[28] Mridha S, Basak D. Semicond Sci Technol 2006;21:928–32.

C

Three-Layer System PdO/$CuWO_4$/CuO for Hydrogen Gas Detection with Reduced Humidity Interference.

N. Kumar, S. Haviar, P. Zeman, P. Baroch

Nanomaterial 2021 MDPI (Submitted)

nanomaterials

MDPI

Article

Three-Layer PdO/$CuWO_4$/CuO System for Hydrogen Gas Sensing with Reduced Humidity Interference

Nirmal Kumar [1], Stanislav Haviar [1,*] and Petr Zeman [1]

[1] Department of Physics and NTIS—European Centre of Excellence, Faculty of Applied Sciences, University of West Bohemia, Univerzitní 8, 306 14 Plzeň, Czech Republic;
* Correspondence: haviar@ntis.zcu.cz; Tel.: +420 377 632 220

Abstract: The growing hydrogen industry stimulates an ongoing search for new materials not only for hydrogen production or storage but also for hydrogen sensing. These materials have to be sensitive to hydrogen, but also their synthesis should be compatible with microcircuit industry to enable seamless integration into various devices. In addition, the interference of air humidity remains an issue for hydrogen sensing materials. We approach these challenges using conventional reactive sputter deposition. Using three consequential processes we synthesized multilayer structures. A basic two-layer system composed of a base layer of cupric oxide (CuO) overlayered with a nanostructured copper tungstate ($CuWO_4$) exhibits higher sensitivity than individual materials. This is explained by formation of microscopic heterojunctions. The addition of a third layer of palladium oxide (PdO) in forms of thin film and particles resulted in a reduction of humidity interference. As a result, a sensing three-layer system working at 150°C with an equalized response in dry/humid air was developed.

Keywords: conductometric hydrogen sensor; copper tungstate; CuWO4; reactive sputtering; nano-heterojunction

Citation: Lastname, F.; Lastname, F.; Lastname, F. Title. *Nanomaterials* **2021**, *11*, x. https://doi.org/10.3390/xxxxx

Academic Editor: Firstname Lastname

Received: 2021-11-09
Accepted: date
Published: date

Publisher's Note: MDPI stays neutral with regard to jurisdictional claims in published maps and institutional affiliations.

1. Introduction

As a prominent clean source of energy, hydrogen plays an important role in power generation. The vast abundance, non-toxic nature, and high combustion efficiency make it a promising source of energy in the future. The highly flammability, wide explosive concentration, the blandness, the odorless and colorless character of hydrogen demand to develop sensors and detectors. Among many approaches, one of the most common are chemiresistors based on metal oxide semiconductors (MOS) [1–4].

Mostly binary oxides such as WO_3, TiO_2, SnO_2, CuO, NiO, etc. have been investigated as chemiresistors. Along with the demands for better performance, novel approaches have been employed such as the formation of heterojunctions by combining more than one MOS [5–7], the addition of catalytic metal particles onto MOS (Pt, Pd, Rh, etc.) [8–11], MOS nanostructuring [12–15], MOS doping or formation of ternary MOS [16,17].

Ternary oxides such as Zn_2SnO_4 [18], $ZnWO_4$ [16,19] $NiWO_4$ [20], and $CuWO_4$ [21,22] are attractive candidates for the research in this field. Copper tungstate ($CuWO_4$) is a promising chemiresistor due to chemical and thermal stability and the presence of metal cations Cu^{2+} and W^{6+} providing adsorption sites [23–25]. Only a few research works have been done on the combination of $CuWO_4$ with other materials. For example, $CuWO_4$/CuO heterojunctions were prepared using wet-based techniques [26–28]. However, these techniques limit the control of the purity and the composition of the final material. In our recent work [21], we have investigated the combination of $CuWO_4/WO_{3-x}$ layers prepared by reactive sputtering, which is a deposition technique compatible with thin-film industry and does not require high temperature for the synthesis.

In this work, we explore the possibility of synthesizing and using of a MOS thin-film system based on $CuWO_4$/CuO. This material system outperforms single-constituent materials in the hydrogen sensing. Moreover, to address the issue of the humidity influence, we added another layer formed by Pd particles and a nanostructured film of PdO. We show that this complex three-layer system can be operated at lower temperature and its response at various values of relative humidity is equalized. To the best of our knowledge, this is the first work dealing with the humidity influence on the $CuWO_4$–based system.

2. Materials and Methods

2.1 Material Synthesis

The investigated thin-film materials were prepared in a form of a layered structure by consecutive sputter depositions from metallic targets onto oxidized Si wafers (with several micrometers thick thermally grown SiO_2) with dimensions of 8.5×8.5×0.6 mm^3.

First, Cu–O layers were deposited in an Ar+O_2 mixture by RF sputtering using a Cu target (target diameter of 72 mm, target power of 228 W, Ar/O_2 flow ratio of 2:1, substrate temperature of 400 °C, working pressure of 0.75 Pa at Ar flow of 10 sccm). The consecutive deposition of W–O layers was done in an Ar+O_2 mixture by DC magnetron sputtering using a W target and (target diameter of 72 mm, target power of 60 W, Ar/O_2 ratio of 4:1, substrate temperature of 400 °C, working pressure of 0.60 Pa at Ar flow of 15 sccm). The depositions' conditions were preoptimized to prepare crystalline Cu–O and W–O layers. Finally, the selected bilayers were then decorated with a small amount of palladium. Pd was deposited in an Ar gas by RF sputtering using a Pd target (target diameter of 50 mm, target power of 37.5 W, no external heating, working pressure of 0.50 Pa at Ar flow of 10 sccm).

All depositions were carried out in a multitarget stainless steel vacuum chamber (Leybold-Heraeus LH Z400) pumped by a turbomolecular pump backed with a scroll pump and a cold trap (cooled by liquid nitrogen). The target-to-substrate distance was 70 mm. The base pressure was always lower than 5 mPa.

As will be shown later, the materials are not synthesized in the form of distinct layers. Anyway, we find it appropriate to denote them by individual layers separated by a slash (/). The superscripts then indicate the thicknesses of the layers as they would be deposited as single layers. For example, the film prepared by depositing 5 nm of tungsten oxide on the top of 20 nm copper oxide and finally decorated with 0.8 nm of Pd is labeled $^{0.8}$Pd/^{5}W–O/^{20}Cu–O. The dash (–) indicates that there could be more oxide phases present (even in the single layers).

2.2 Material Analyses and Sensing Measurements

To study the structural properties of the as-deposited films, X-Ray diffraction (XRD) analysis was performed using a diffractometer (X'Pert PRO PANanalytical) with Cu K_α source of radiation in the Bragg-Brentano configuration. Further understanding of the crystalline phases was achieved by employing Raman spectroscopy (Horiba Jobin Yvon LABRAM HR Evolution) using a 532-nm laser.

Morphological analysis of the specimens was carried out in scanning electron microscope (SEM) (Horiba SU70).

The gas response was measured using a four-point probe measurement technique in flow mode using a custom-built heated brass reaction chamber (total volume 9 cm^3) with gas inlet and outlet slots. Synthetic air was mixed from clean gases (N_2, O_2) in a 79:21 ratio using two flow controllers (Alicat Scientific). The tunable portion of the synthetic air can be humidified by bubbling through a warm water bath and then mixed again with the dry portion of the air. The resulting relative humidity is measured in the tube using a sensor (Sensirion, SHT 85). Close to the measuring chamber, hydrogen is introduced into the flow using another flow controller enabling to tune its final concentration. The total flow is maintained at 100 sccm. More details about the system can be found in our previous works

in [11,21]. The samples were stabilized directly under the measurement conditions. The electrical resistance, as well as the response, were stabilized after a few hours. Such stabilized material is denoted as 'measured' in the following text.

For the purpose of this paper, we define the sensitivity for the *n*-type material as:

$$S = \frac{R_g}{R_a}, \quad (1)$$

where R_a and R_g are the resistances in the presence of synthetic air and H_2 gas mixed with air, respectively. For the *p*-type, the reciprocal relation is used according to [29].

3. Results and Discussion

In this section, we describe the composition, structure, and surface morphology of the synthesized thin-film materials. Further, we move on to the description of the sensing behavior and differences between the prepared films. In the end, we discuss the influence of the structural differences on the sensing performance.

We prepared numerous combinations of layers, but in this paper we present only those that are interesting from the point of view of the structure and/or sensing performance. Therefore, all films presented here are based on a 20 nm thick layer of Cu–O which is then overlayered with 5, 10 or 20 nm thick layer of W–O. After stabilization at 300 °C and the measurement of the sensing performance, the films were finally decorated with Pd and stabilized at 200 °C. Let us note that for particular analyses only key results are presented.

3.1. Structure

The structure of the films was studied by XRD and Raman spectroscopy. Fig. 1a displays XRD patterns and Fig. 1b Raman spectra of both as-deposited (grey traces) and measured films (color traces).

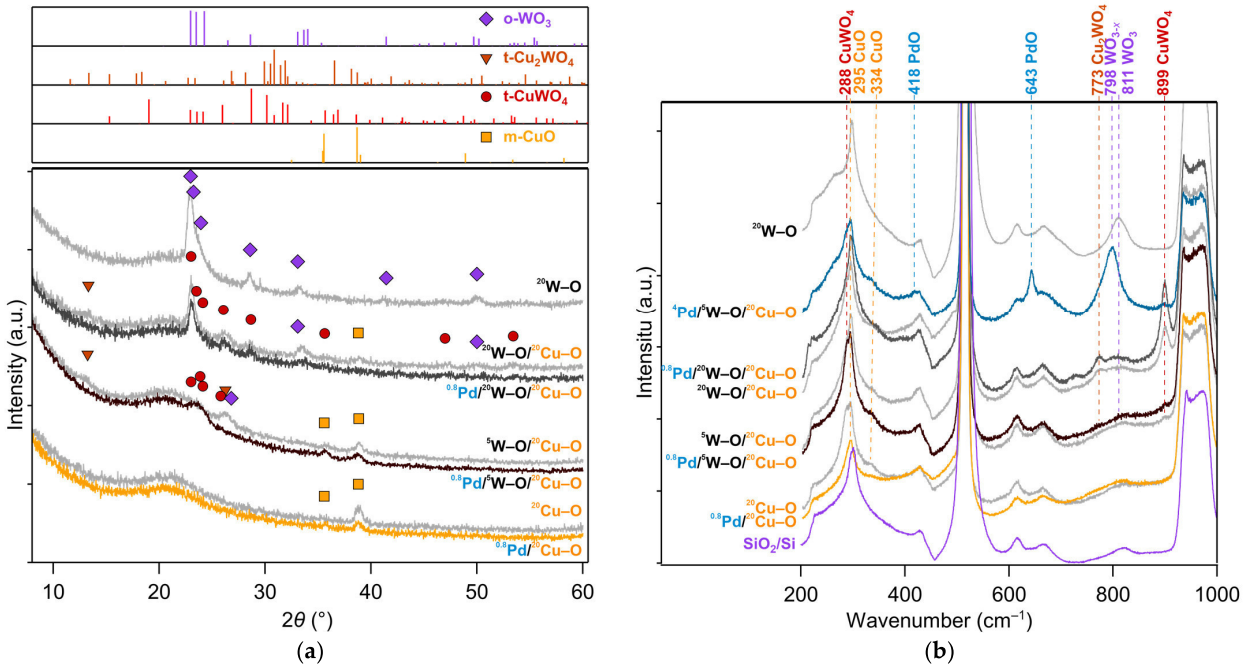

Fig. 1 XRD spectrograms (a) and Raman spectra (b) of the measured specimen. The gray traces are Pd-free films while the color traces are of measured (for gas sensitivity) films decorated with $^{0.8}$Pd.

As seen in Fig. 1a, the single layers of ^{20}Cu–O and ^{20}W–O exhibit the monoclinic CuO (PDF card No. 04-007-1375) and orthorhombic WO_3 (PDF card No. 04-007-2425) phases,

respectively. A broad peak in the range of 18–24° corresponds to an amorphous silica phase of the thermally oxidized Si.

Deposition of W–O species onto the CuO layer does not result in the formation of a distinct bilayer structure of CuO and WO_3, but rather leads to their intermixing and the formation of copper tungstates. The triclinic $CuWO_4$ (PDF Card No. 04-009-6293) and Cu_2WO_4 (PDF Card No. 04-041-0948) phases can be observed in the as-deposited W–O/^{20}Cu–O films. The more W–O species are deposited, the more clearly the tungstate phases are identified in the structure of the as-deposited films, compare XRD patterns for the ^{5}W–O/^{20}Cu–O and ^{20}W–O/^{20}Cu–O films. The intermixing of the pre-deposited CuO with the arriving W–O species occurs thanks to an energetic flux of the incoming species, which is also promoted by an elevated deposition temperature of 400 °C. Besides tungstates, CuO and WO_3 are also detectable in the structure of the as-deposited films but as minor phases, especially for the ^{20}W–O/^{20}Cu–O film.

Because we observed that the decoration of the films with a small amount of Pd has no effect on the XRD patterns, we present directly measured films with a 0.8 nm addition of Pd in Fig. 3 (colored traces). As can be seen in Fig. 1a, the sensing measurement performed at an elevated temperature leads to a further intermixing of the materials. This is accompanied by disappearing of diffraction peaks from Cu_2WO_4 and lowering intensities of diffraction peaks from CuO and WO_3. The dominant phase after the sensing measurement is then $CuWO_4$.

The state of Pd is hard to identify on the basis of XRD because of a negligible signal from really thin Pd-containing layers. However, we found that this can be overcome by using Raman spectroscopy when we analyzed a ^{4}Pd-decorated film that was synthesized with the aim of increasing the signal of the Pd-containing layer. In Fig. 1b, a Raman spectrum of this ^{4}Pd/^{5}W–O/^{20}Cu–O film is shown. Peaks at the positions of 418 and 643 cm^{-1} [30,31] can be well associated with the occurrence of PdO that forms islands on the surface as will be shown later.

Furthermore, Raman spectroscopy corroborates the results of XRD. Raman peaks observed in the as-deposited and measured multilayer films were identified by comparing them with literature data and spectra of the single ^{20}Cu–O and ^{20}W–O films, and of the thermally oxidized Si substrate. Peaks at 295 and 334 cm^{-1} are attributed to CuO [26,32] and can be found in the spectra of all multilayer films. However, when the amount of W–O is increased from ^{5}W–O to ^{20}W–O, the signal from CuO is reduced while the peak corresponding to $CuWO_4$ at the position of 899 cm^{-1} [33,34] gains distinctly in its intensity. This confirms a nearly complete intermixing of W–O with Cu–O. The other phase of tungstate (Cu_2WO_4) was also observed at the position of 773 cm^{-1} [34,35] but with a much lower peak intensity. Other distinguishable peaks at the positions of 300, 428, 513, 615, 664, 821 cm^{-1} and a broad feature at 936–974 cm^{-1} are attributed to the SiO_2/Si substrate.

3.2 Surface Morphology

The SEM micrographs in Fig. 2 illustrate the evolution of the surface morphology with the overlayering of ^{20}Cu–O by W–O in the as-deposited state and after the sensing measurements (stabilization) at 300 °C in both the dry and humid air. The surface morphology of a single ^{20}Cu–O layer in the as-deposited state in Fig. 2a is of uniform contrast and the surface consists of irregular fine features typical for sputtered films. The overlayering of this layer by ^{5}W–O results only in an increase in the size of the surface features (Fig. 2b). The sensing measurement at 300°C, however, causes changes in the surface morphology. The surface is then characterized by zones of different contrasts (Fig. 2c). This effect is more pronounced for the ^{20}W–O/^{20}Cu–O film (Fig. 2d). In agreement with our previously published work [21], where an inverse material combination (^{10}Cu–O/^{20}W–O) was synthesized, we may attribute the brighter zones to the formation of copper tungstate.

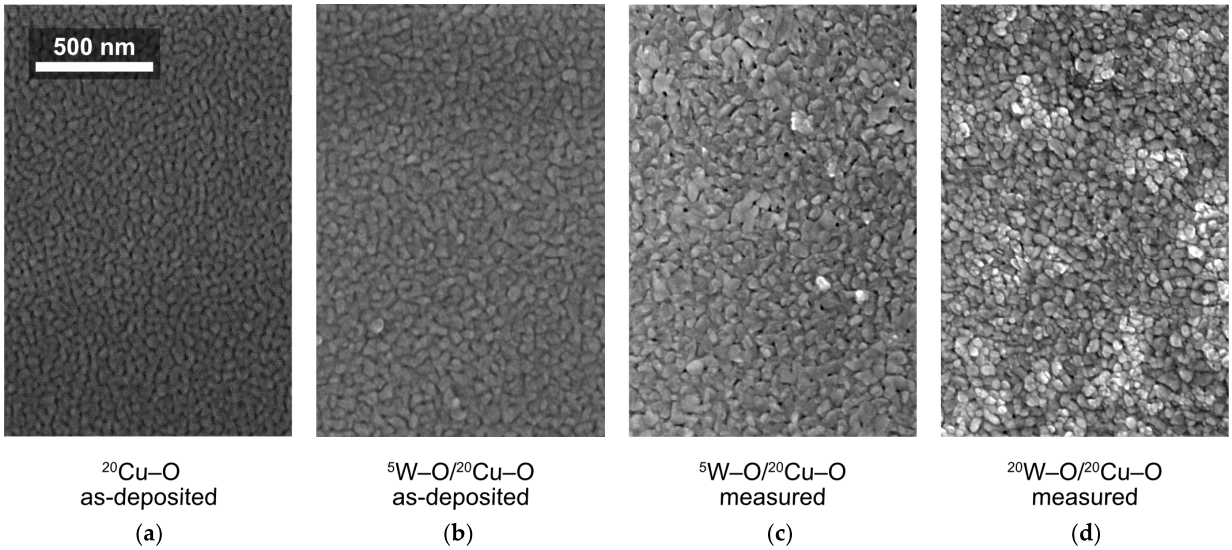

Fig. 2 SEM micrographs of the as-deposited (**a**,**b**) and measured films (**c**,**d**) (at 300°C in both dry and humid synthetic air.) The brighter zones, possibly formed by tungstate, are visible in (**c**,**d**).

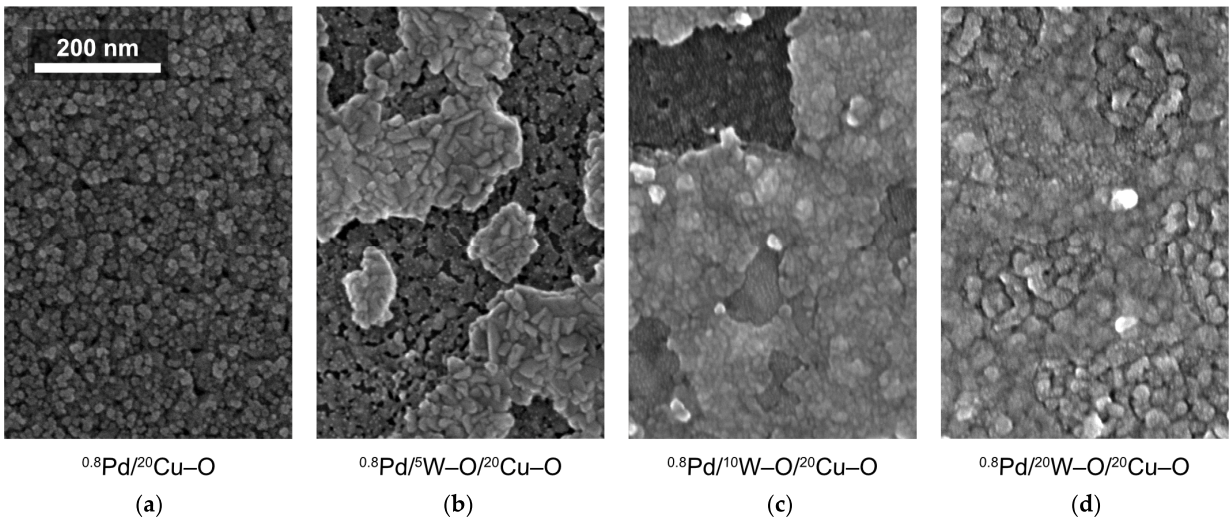

Fig. 3 SEM micrographs of measured films decorated with palladium. The Pd forms oxidized small particles (well visible in (**b**)) and bright zones on-top of base bilayer (**b–d**).

The evolution of the zones of a different contrast is demonstrated by SEM micrographs in Fig. 3. Here, films after the decoration with $^{0.8}$Pd and the subsequent sensing measurements (and the stabilization) at 200°C in both the dry and humid air are depicted. As shown in Fig. 3a, the addition of Pd covers the single ^{20}Cu–O layer uniformly and the sensing measurement does not initiate any pronounced changes in the surface morphology. However, a different situation is observed after the sensing measurements of the $^{0.8}$Pd/W–O/^{20}Cu–O Fig. 3b–d). The surface of all these films is characterized by two different zones. The darker one is like that observed on the single ^{20}Cu–O film (Fig. 3a) while the brighter one is represented by islands that occupy more area with increasing amount of added W–O (Fig. 3b–d). Furthermore, the surface of the islands is raised above the dark zone level as observed by AFM and shown in Fig. 4 for the $^{0.8}$Pd/^{5}W–O/^{20}Cu–O film. We suppose that since the films are subjected to further sensing measurement, i.e., annealed at 200 °C for several hours in humid air, the process of intermixing W–O with Cu–O continues, resulting in the formation of the islands of $CuWO_4$ that grow in size and height.

For the film with the highest amount of W–O ($^{0.8}$Pd/^{20}W–O/^{20}Cu–O), the surface is nearly all covered with $CuWO_4$.

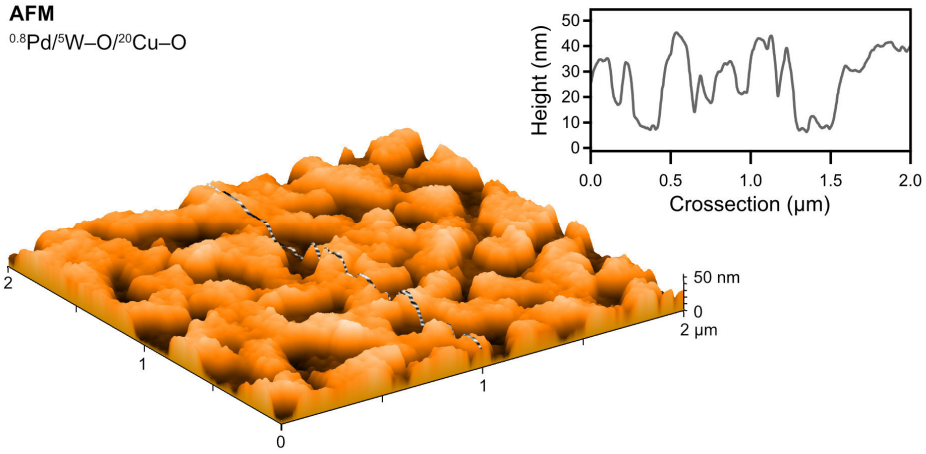

Fig. 4 AFM image and cross-section of measured $^{0.8}$Pd/^{5}W–O/^{20}Cu–O film. The height of features covered with PdO is approximately from 20 to 30 nm.

As proven by Raman spectroscopy, Pd oxidizes during the sensing measurement. While on the Cu–O surface it forms nanometer-sized particles (small white dots visible in Fig. 3), the $CuWO_4$ surface favors the formation of PdO [36] as a continuous layer. It is worth noting that an approximately 30 nm height of the islands (Fig. 4) excludes that these islands are formed by PdO only because there is simply not enough material for it. Interestingly, the appearance of the Pd particles in the dark zone is similar to that observed on ^{2}Pd/^{100}W–O films synthesized at similar parameters (published in our previous work [17]).

In summary, the consecutive deposition of the Cu–O and W–O layers does not lead to the formation of a distinct bilayer structure of binary oxides, but leads to the formation of a bilayer of copper tungstate and cupric oxide, or copper tungstate alone (depending on the amount of Cu–O). The decoration with Pd and the subsequent sensing measurement results in the formation of the $CuWO_4$ islands covered with the PdO film and nanoparticles of PdO on the Cu–O surface. According to the other works [37,38], it is reasonable to presume that the Pd particles are of a core-shell nature (a Pd core covered by PdO), yet XRD or Raman spectroscopy are not capable confirming it.

3.3. Sensing Response

The synthesized films were stabilized in the measuring chamber at elevated temperatures under the measuring conditions (300°C for the Pd-free films and 200°C for the Pd-decorated films). After several hours of the stabilization, the response curves were recorded, the films were exposed to various concentrations of H_2 in synthetic air. First, we demonstrate how the bilayer W–O/^{20}Cu–O system outperforms the response of the single-layer ^{20}CuO film. Then, we explain how the humidity in the air negatively affects the response and how this unwanted effect can be reduced by decorating the films with Pd and by tuning the working temperature.

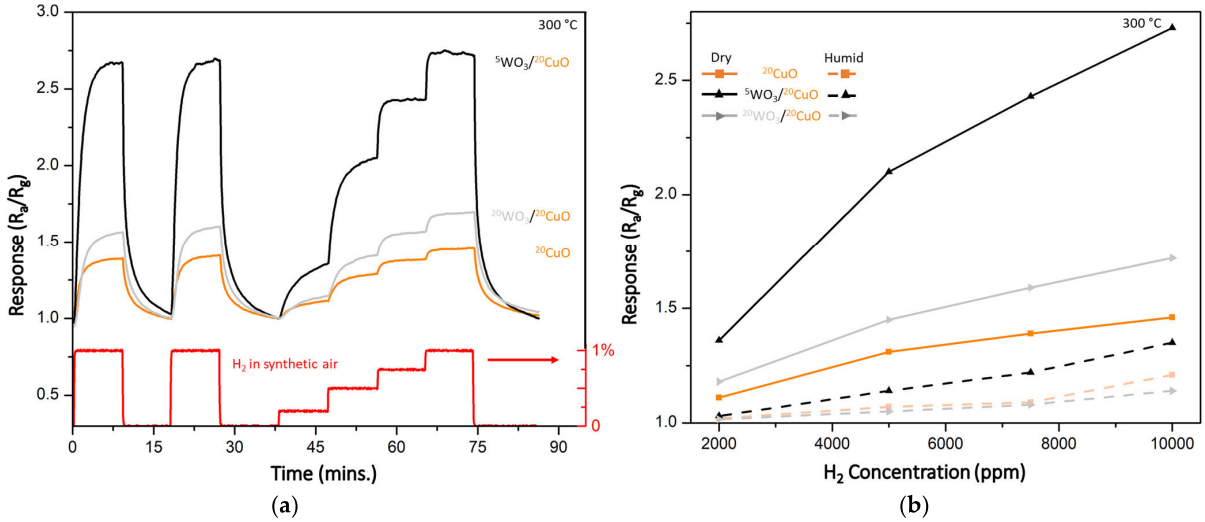

Fig. 5 (**a**) Response of synthesized films without decoration with Pd. The combination of layers enhances the response to the hydrogen. (**b**) The response of the films drops in humid air (90% RH) – dashed lines.

Response curves (measured in dry air at 300 °C) of the Pd-free films are illustrated in Fig. 5a where the response R_g/R_a vs time is plotted. The yellow curve shows the behavior of the single-layer ^{20}CuO film. The response of this film is enhanced nearly twice if ^{5}W–O is deposited on the top (^{5}W–O/^{20}Cu–O). However, a further addition of W–O (^{20}W–O/^{20}Cu–O) results in a decrease in the magnitude of the response, although it is still better than for ^{20}CuO alone. The enhancement for the ^{5}W–O/^{20}Cu–O film can be explained by the formation of $CuWO_4$ over the CuO layer leading to the development of *n-p* heterojunctions. A depletion layer is formed between *n*-type $CuWO_4$ and *p*-type CuO. The situation is depicted in Fig. 6a,b. Due to this, the conductive channel is reduced for the film and so the surface reactions with hydrogen cause a bigger change in the resistance. This is also in agreement with the shift of the resistance baseline from 300 kΩ to 550 kΩ for ^{20}Cu–O to ^{5}W–O/^{20}Cu–O, respectively. The trend and explanation are found to be similar to the previously studied structures, where $CuWO_4$ was grown on the top of a W–O layer forming *n-n* junctions [21] and is documented also in other works for similar materials [37,38].

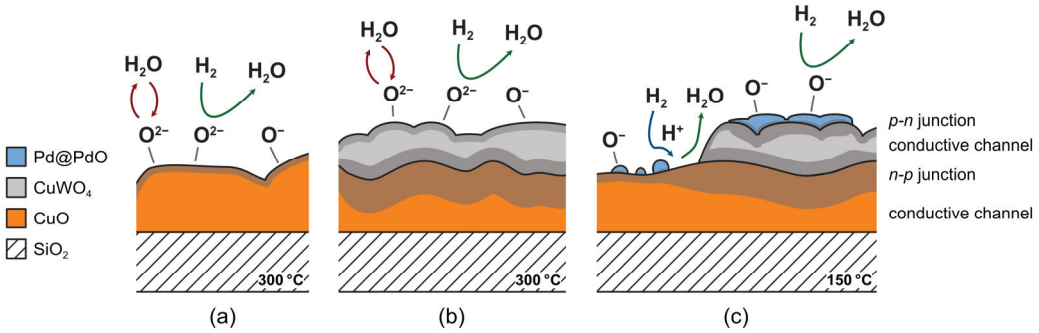

Fig. 6 Scheme of synthesized structures with indicated reactions on the surface. Detailed explanation in text.

The numerically calculated values of the sensitivity according to Eq. (1) for the described bilayers are plotted in Fig. 5b. The sensitivity values for various concentrations of H_2 in dry air are represented by solid lines while the dashed lines correspond to the sensing measurements in humid air.

The sensitivity decreases in the humid environment. The effect of reduced sensitivity in humid air is described in the literature [39,40]. The interference of humidity negatively affects the gas-sensing behavior of materials, mainly, for reducing gases such as H_2 and H_2S. A discussion of this effect follows.

In the dry condition, the sensing mechanism can be described by the following equations [41–43] (green arrows in Fig. 6):

$$\frac{1}{2}O_2 + 2e^- \rightarrow O^{2-}_{ads} \quad (2)$$

$$H_{2\,ads} + O^{2-}_{ads} \rightarrow H_2O + 2e^- \quad (3)$$

However, when the bilayers are exposed to gas in a humid environment, the water molecules react with adsorbed oxygen species on the surface, leading to an increase in the baseline resistance of the bilayer and a decrease in its sensitivity. At the same time, hydrogen cannot find the oxygen species to react with and the interchange of electrons, and thus the response is reduced [40,44] (red arrows in Fig. 6).

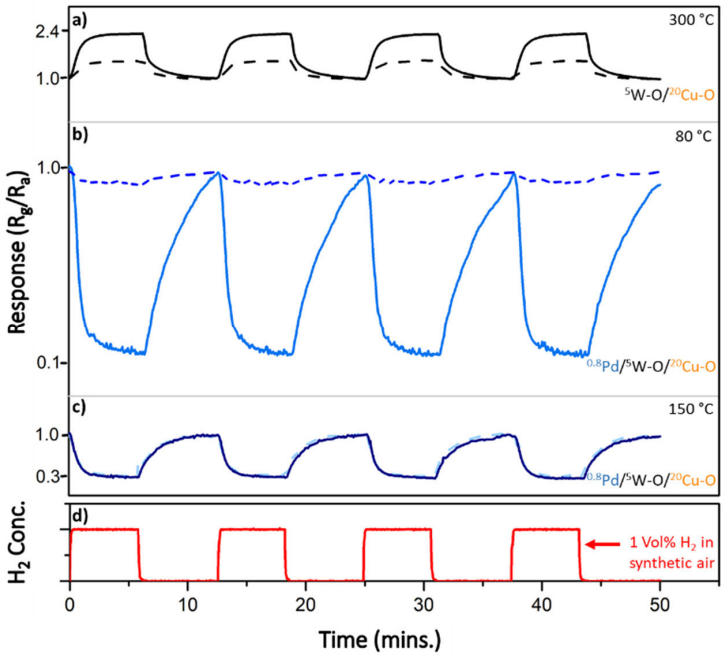

Fig. 7 Sensing response for Pd-decorated film ($^{0.8}$Pd/^{5}W–O/^{20}Cu–O) (**b, c**) and Pd-free film (**a**). The response at lower temperatures switches to *n*-type semiconductor. The solid lines represent response in dry air, dashed ones in humid air (96% RH)

The adsorption of water can be described by one of the two following mechanisms as

$$H_2O + M + O_O \rightarrow (M^+ - OH^-) + (OH)^+_O + e^- \quad (4)$$

or

$$H_2O + 2M + O_O \rightarrow 2(M^+ - OH^-) + V^{2+}_O + 2e^-. \quad (5)$$

Both involve the formation of OH^- groups on the surface that is bonded to the metal ion M^+. According to the first mechanism, Eq. (4), the other hydrogen from the water molecule forms a rooted hydroxyl group $(OH)^+_O$ with the lattice oxygen O_O. In the other proposed mechanism, Eq. (5), the lattice oxygen forms another adsorbed OH^- bonded to M^+ while leaving an oxygen vacancy V^{2+}_O.

To address the issue in the reduction of the response, the films were decorated with 0.8 nm of Pd. According to Raman spectroscopy, XRD, and other published works on the similar systems [38,45], Pd particles/objects are covered with PdO on their surfaces. Pd and PdO play several important roles in the reaction, see also Fig. 6c:

(i) Pd promotes the selectivity towards hydrogen and, at the same time, reduces the response temperature by facilitating the dissociation of H_2 [37] (blue arrow in Fig. 6c).
(ii) PdO favors the adsorption of oxygen over the hydroxyl groups [45].
(iii) PdO forms another heterojunction (*p–n)* with the topmost layer of copper tungstate.

Furthermore, the presence of Pd allowed us to reduce the response temperature and stabilize the films at only 200 °C. After stabilization, the response of the films was measured at various lower temperatures. The response curve in Fig. 7a is of the Pd-free film (^{5}W–O/^{20}Cu–O) measured at a temperature of 300°C where the sensitivity was the highest. In Fig. 7b, the response of the Pd-decorated film ($^{0.8}$Pd/^{5}W–O/^{20}Cu–O) measured at 80 °C only is shown. At this temperature, the sensitivity was the highest (~8.2). On the other hand, the effect of humidity is enormous and the responses in humid and dry conditions differ greatly; compare solid lines (dry air) and dashed lines (humid air, 90% RH). When the operating temperature was adjusted, we were able to equalize the response to hydrogen in dry and humid air. At 150 °C, the sensitivity is partially reduced (~3.4), but the response is the same regardless of humidity (Fig. 7c). This can be explained by the fact that the OH groups on the surface desorb at higher temperatures, which can partly eliminate the humidity effect [45,46].

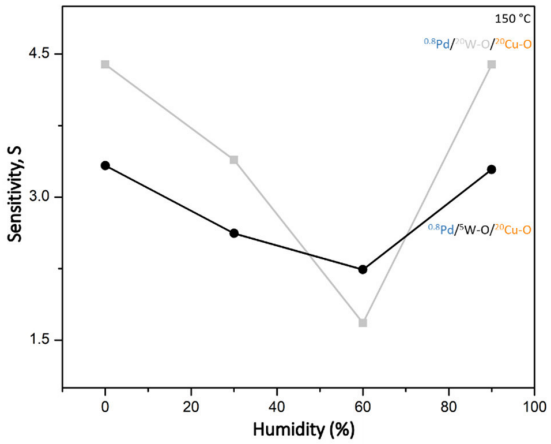

Fig. 8 Sensitivities of Pd-decorated films at low temperature. The film with more pronounced multilayer structure ($^{0.8}$Pd–^{5}W–O/^{20}Cu–O) exhibit more equalized response to hydrogen under various relative humidity levels.

It is important to note that the character of the response changes with going to the lower temperatures. The film responds as *n*-type (the resistance decreases with hydrogen) at lower temperatures (80°C and 150°C), while it behaves as *p*-type at 300°C. This can be explained by the layered architecture of the film. As the different types of semiconductors are synthesized on the top of each other, they can be imagined as parallelly connected resistors. At higher temperatures, the reaction on *p*-type CuO dominates. At lower temperatures, CuO does not respond at all, or its contribution is minor, and the resistance change in *n*-type $CuWO_4$ dominates.

Finally, let us explain why it is important to employ both the films and not only use a single-phase film decorated with Pd. The plot in Fig. 8 shows the response of the two $^{0.8}$Pd/^{5}W–O/^{20}Cu–O and $^{0.8}$Pd/^{20}W–O/^{20}Cu–O films to 1 vol.%. of H_2 at various levels of

humidity. According to the previous section, the architecture of the first one is copper tungstate on the top of CuO. The other one is mainly formed by a copper tungstate (with only a negligible remaining layer of CuO). The response trend is found to be similar for both films, but for the $^{0.8}$Pd/^{5}W–O/^{20}Cu–O film it is more stable over the humidity scale. Humidity shifts the baseline of the resistance of the materials. The $^{0.8}$Pd/^{5}W–O/^{20}Cu–O film exhibits more humidity-independent sensitivity because even if CuO does not contribute notably to the response to H_2, it compensates for the effect of humidity in the other direction. We believe, this is mainly because of the narrowed conduction channel formed by the *n-p* heterojunctions in between $CuWO_4$ and CuO. Thanks to that, the response at various levels of humidity is equalized.

4. Conclusions

We demonstrated a synthesis of a thin-film material consisting of three types of layers: cupric oxide, copper tungstate, and palladium oxide particles/film. The synthesis process consists of three consecutive steps: reactive sputtering from the copper target, reactive magnetron sputtering from the tungstate target, and sputtering of palladium. The stabilization of the films during the sensing measurements in dry and/or humid air is also crucial for the formation of individual phases. The structure and the surface morphology of the films were then described in detail.

The measurement of the conductometric response to hydrogen showed that the response of cupric oxide alone can be enhanced by depositing tungsten oxide on the top, which leads to an intermixing of both phases. As a result, a layer of copper tungstate is formed along with *n-p* heterojunctions in between the top *n*-type $CuWO_4$ layer and the bottom *p*-type CuO layer. These bilayers suffer from enormous interference of the relative humidity when detecting the hydrogen gas. This issue was resolved by adding Pd. After stabilization at 200 °C, a third layer consisting of a PdO film and nano-sized oxidized Pd particles is formed. Consequently, the response in dry and humid air is equalized at only 150 °C. This could be explained by a mutual compensation of the changes in humid environment by the *n-p* heterojunctions in between $CuWO_4$ and CuO.

This complex material is a good candidate for use in conductometric sensors. The relatively simple synthesis is compatible with thin-film technology and does not require high temperatures.

Author Contributions: Conceptualization, S.H.; methodology, S.H.; investigation, S.H and N.K.; resources, P.Z.; writing—original draft preparation, N.K.; writing—review and editing, S.H. and P.Z.; visualization, S.H. and N.K.; All authors have read and agreed to the published version of the manuscript.

Funding: This work was supported by the Czech Science Foundation under Project No. GA19-13174S.

Acknowledgments: Authors would like to express gratitude to prof. J. Čapek for his numerous consultations. Also authors thanks to Dr. R. Čerstvý for XRD measurements and analyses.

Conflicts of Interest: The authors declare no conflict of interest.

References

1. Liu, Y.; Xiao, S.; Du, K. Chemiresistive Gas Sensors Based on Hollow Heterojunction: A Review. *Adv. Mater. Interfaces* **2021**, *8*, 1–21, doi:10.1002/admi.202002122.
2. Steinhauer, S. Gas sensors based on copper oxide nanomaterials: A review. *Chemosensors* **2021**, *9*, 1–20, doi:10.3390/chemosensors9030051.
3. Nasiri, N.; Clarke, C. Nanostructured chemiresistive gas sensors for medical applications. *Sensors (Switzerland)* **2019**, *19*, 17–19, doi:10.3390/s19030462.

4. Srinivasan, P.; Ezhilan, M.; Kulandaisamy, A.J.; Babu, K.J.; Rayappan, J.B.B. Room temperature chemiresistive gas sensors: challenges and strategies—a mini review. *J. Mater. Sci. Mater. Electron.* **2019**, *30*, 15825–15847, doi:10.1007/s10854-019-02025-1.
5. Mridha, S.; Basak, D. Investigation of a p-CuO/n-ZnO thin film heterojunction for H 2 gas-sensor applications. *Semicond. Sci. Technol. Semicond. Sci. Technol* **2006**, *21*, 928–932, doi:10.1088/0268-1242/21/7/017.
6. Liu, Y.; Lai, P.T.; Tang, W.M. Improved hydrogen-sensing performance of Pd/WO<inf>3</inf>/SiC Schottky diode by La doping. In Proceedings of the 2016 IEEE International Conference on Electron Devices and Solid-State Circuits (EDSSC); IEEE, 2016; pp. 338–341.
7. Maziarz, W. TiO 2 /SnO 2 and TiO 2 /CuO thin film nano-heterostructures as gas sensors. *Appl. Surf. Sci.* **2019**, *480*, 361–370, doi:10.1016/j.apsusc.2019.02.139.
8. Moseley, P.T. Progress in the development of semiconducting metal oxide gas sensors: A review. *Meas. Sci. Technol.* **2017**, *28*, doi:10.1088/1361-6501/aa7443.
9. Boudiba, a; Roussel, P.; Zhang, C.; Snyders, R.; Debliquy, M.; Nova, M. Sensing mechanism of hydrogen sensors based on Pd loaded tungsten oxide (Pd-WO 3). **2012**, 795–797, doi:10.5162/IMCS2012/P1.0.16.
10. Ghasempour, R.; Mortazavi, S.Z.; Iraji zad, A.; Rahimi, F. Hydrogen sensing properties of multi-walled carbon nanotube films sputtered by Pd. *Int. J. Hydrogen Energy* **2010**, *35*, 4445–4449, doi:10.1016/j.ijhydene.2010.01.150.
11. Haviar, S.; Čapek, J.; Batková, Š.; Kumar, N.; Dvořák, F.; Duchoň, T.; Fialová, M.; Zeman, P. Hydrogen gas sensing properties of WO3 sputter-deposited thin films enhanced by on-top deposited CuO nanoclusters. *Int. J. Hydrogen Energy* **2018**, *43*, 22756–22764, doi:10.1016/j.ijhydene.2018.10.127.
12. Mattoni, G.; de Jong, B.; Manca, N.; Tomellini, M.; Caviglia, A.D. Single-Crystal Pt-Decorated WO 3 Ultrathin Films: A Platform for Sub-ppm Hydrogen Sensing at Room Temperature. *ACS Appl. Nano Mater.* **2018**, acsanm.8b00627, doi:10.1021/acsanm.8b00627.
13. Takahashi, H.; Okazaki, S.; Nishijima, Y.; Arakawa, T. Optimization of Hydrogen Sensing Performance of Pt / WO 3 Gasochromic Film Fabricated by Sol – Gel Method. **2017**, *29*, 1259–1268.
14. Jagadale, S.B.; Patil, V.L.; Vanalakar, S.A.; Patil, P.S.; Deshmukh, H.P. Preparation, characterization of 1D ZnO nanorods and their gas sensing properties. *Ceram. Int.* **2018**, *44*, 3333–3340, doi:10.1016/j.ceramint.2017.11.116.
15. Zappa, D. The influence of Nb on the synthesis of WO3 nanowires and the effects on hydrogen sensing performance. *Sensors (Switzerland)* **2019**, *19*, doi:10.3390/s19102332.
16. Wang, Y.; Cai, L.; Li, Y.; Tang, Y.; Xie, C. Structural and photoelectrocatalytic characteristic of ZnO/ZnWO 4/WO3 nanocomposites with double heterojunctions. *Phys. E Low-Dimensional Syst. Nanostructures* **2010**, *43*, 503–509, doi:10.1016/j.physe.2010.09.005.
17. Kumar, N.; Haviar, S.; Rezek, J.; Baroch, P.; Zeman, P. Tuning Stoichiometry and Structure of Pd-WO3−x Thin Films for Hydrogen Gas Sensing by High-Power Impulse Magnetron Sputtering. *Materials (Basel).* **2020**, *13*, 5101, doi:10.3390/ma13225101.
18. Zhang, D.; Wu, Z.; Zong, X.; Zhang, Y. Fabrication of polypyrrole/Zn2SnO4 nanofilm for ultra-highly sensitive ammonia sensing application. *Sensors Actuators, B Chem.* **2018**, *274*, 575–586, doi:10.1016/j.snb.2018.08.001.
19. Leonard, K.C.; Nam, K.M.; Lee, H.C.; Kang, S.H.; Park, H.S.; Bard, A.J. ZnWO4/WO3 composite for improving photoelectrochemical water oxidation. *J. Phys. Chem. C* **2013**, *117*, 15901–15910, doi:10.1021/jp403506q.
20. Mohamed, M.M.; Ahmed, S.A.; Khairou, K.S. Unprecedented high photocatalytic activity of nanocrystalline WO3/NiWO4 hetero-junction towards dye degradation: Effect of template and synthesis conditions. *Appl. Catal. B Environ.* **2014**, *150–151*, 63–73, doi:10.1016/j.apcatb.2013.12.001.
21. Kumar, N.; Čapek, J.; Haviar, S. Nanostructured CuWO4/WO3- films prepared by reactive magnetron sputtering for

hydrogen sensing. *Int. J. Hydrogen Energy* **2020**, *45*, 18066–18074, doi:10.1016/j.ijhydene.2020.04.203.

22. Zhan, F.; Li, J.; Li, W.; Liu, Y.; Xie, R.; Yang, Y.; Li, Y.; Chen, Q. In situ formation of CuWO<inf>4</inf>/WO<inf>3</inf> heterojunction plates array films with enhanced photoelectrochemical properties. *Int. J. Hydrogen Energy* **2015**, *40*, 6512–6520, doi:10.1016/j.ijhydene.2015.03.131.
23. Simion, C.E.; Somacescu, S.; Teodorescu, V.S.; Osiceanu, P.; Stanoiu, A. H2S sensing mechanism of SnO2-CuWO4 operated under pulsed temperature modulation. *Sensors Actuators, B Chem.* **2018**, *259*, 258–268, doi:10.1016/j.snb.2017.12.027.
24. Catto, A.C.; Fiorido, T.; Souza, É.L.S.; Avansi, W.; Andres, J.; Aguir, K.; Longo, E.; Cavalcante, L.S.; da Silva, L.F. Improving the ozone gas-sensing properties of CuWO4 nanoparticles. *J. Alloys Compd.* **2018**, *748*, 411–417, doi:10.1016/j.jallcom.2018.03.104.
25. Zhang, W.; Zhang, D.; Zhang, Y. High-performance NO2 gas sensor based on bimetallic oxide CuWO4 decorated with reduced graphene oxide. *J. Mater. Sci. Mater. Electron.* **2020**, *31*, 6706–6715, doi:10.1007/s10854-020-03227-8.
26. Polyakov, B.; Kuzmin, A.; Vlassov, S.; Butanovs, E.; Zideluns, J.; Butikova, J.; Kalendarev, R.; Zubkins, M. A comparative study of heterostructured CuO / CuWO 4 nanowires and thin films. *J. Cryst. Growth* **2017**, *480*, 78–84, doi:10.1016/j.jcrysgro.2017.10.011.
27. Zheng, J.Y.; Song, G.; Kim, C.W.; Kang, Y.S. Facile preparation of p-CuO and p-CuO/n-CuWO 4 junction thin films and their photoelectrochemical properties. *Electrochim. Acta* **2012**, *69*, 340–344, doi:10.1016/j.electacta.2012.03.011.
28. Andrade Neto, N.F.; Oliveira, Y.G.; Nascimento, J.H.O.; Bomio, M.R.D.; Motta, F. V. Influence of pH variation on CuWO4, CuWO4/WO3 and CuWO4/CuO structures stabilization: study of the photocatalytic properties under sunlight. *J. Mater. Sci. Mater. Electron.* **2020**, *31*, 18221–18233, doi:10.1007/s10854-020-04371-x.
29. Moseley, P. Solid state gas sensors. *Meas. Sci. Technol.* **1997**, *223*, 223–237.
30. Kumari, T.; Gopal, R.; Goyal, A.; Joshi, J. Sol–Gel Synthesis of Pd@PdO Core–Shell Nanoparticles and Effect of Precursor Chemistry on Their Structural and Optical Properties. *J. Inorg. Organomet. Polym. Mater.* **2019**, *29*, 316–325, doi:10.1007/s10904-018-1001-x.
31. Baylet, A.; Marécot, P.; Duprez, D.; Castellazzi, P.; Groppi, G.; Forzatti, P. In situ Raman and in situ XRD analysis of PdO reduction and Pd° oxidation supported on γ-Al2O3 catalyst under different atmospheres. *Phys. Chem. Chem. Phys.* **2011**, *13*, 4607–4613, doi:10.1039/c0cp01331e.
32. Sriyutha Murthy, P.; Venugopalan, V.P.; Das; Arunya, D.; Dhara, S.; Pandiyan, R.; Tyagi, A.K. Antibiofilm activity of nano sized CuO. *Proc. Int. Conf. Nanosci. Eng. Technol. ICONSET 2011* **2011**, 580–583, doi:10.1109/ICONSET.2011.6168037.
33. Chen, C.; Bi, W.; Xia, Z.; Yuan, W.; Li, L. Hydrothermal Synthesis of the CuWO4/ZnO Composites with Enhanced Photocatalytic Performance. *ACS Omega* **2020**, *5*, 13185–13195, doi:10.1021/acsomega.0c01220.
34. Thongpan, W.; Louloudakis, D.; Pooseekheaw, P.; Kumpika, T.; Kantarak, E.; Sroila, W.; Panthawan, A.; Thongsuwan, W.; Singjai, P. Porous CuWO4/WO3 composite films with improved electrochromic properties prepared by sparking method. *Mater. Lett.* **2019**, *257*, 126747, doi:10.1016/j.matlet.2019.126747.
35. Tayar Galante, M.; Živković, A.; Alvim, J.C.; Calchi Kleiner, C.C.; Sangali, M.; Taylor, S.F.R.; Greer, A.J.; Hardacre, C.; Rajeshwar, K.; Caram, R.; et al. Arc Synthesis, Crystal Structure, and Photoelectrochemistry of Copper(I) Tungstate. *ACS Appl. Mater. Interfaces* **2021**, *13*, 32865–32875, doi:10.1021/acsami.1c03928.
36. Gancheva, M.; Velinova, R.; Konova, P.; Stefanov, P.; Iordanova, R.; Naydenov, A. On the stabilization of the oxidized state of palladium by CuWO 4 for application as catalyst in abatement of C 1 –C 4 hydrocarbons emissions. *Mater. Res. Express* **2019**, *6*, 085554, doi:10.1088/2053-1591/ab2933.
37. Annanouch, F.E.; Roso, S.; Haddi, Z.; Vallejos, S.; Umek, P.; Bittencourt, C.; Blackman, C.; Vilic, T.; Llobet, E. p-Type PdO nanoparticles supported on n-type WO3 nanoneedles for hydrogen sensing. *Thin Solid Films* **2016**, *618*, 238–245, doi:10.1016/j.tsf.2016.08.053.

38. Cao, Y.; Zhou, C.; Chen, Y.; Qin, H.; Hu, J. Enhanced CO Sensing Performances of PdO/WO3Determined by Heterojunction Structure under Illumination. *ACS Omega* **2020**, *5*, 28784–28792, doi:10.1021/acsomega.0c04137.
39. Urasinska-Wojcik, B.; Gardner, J.W. H2S Sensing in Dry and Humid H2 Environment with p-Type CuO Thick-Film Gas Sensors. *IEEE Sens. J.* **2018**, *18*, 3502–3508, doi:10.1109/JSEN.2018.2811462.
40. Miao, J.; Chen, C.; Lin, J.Y.S. Humidity independent hydrogen sulfide sensing response achieved with monolayer film of CuO nanosheets. *Sensors Actuators, B Chem.* **2020**, *309*, 127785, doi:10.1016/j.snb.2020.127785.
41. Jolly Bose, R.; Illyaskutty, N.; Tan, K.S.; Rawat, R.S.; Matham, M.V.; Kohler, H.; Mahadevan Pillai, V.P. Hydrogen sensors based on Pt-loaded WO 3 sensing layers. *Europhys. Lett.* **2016**, *114*, 66002, doi:10.1209/0295-5075/114/66002.
42. De Marcellis, A.; Ferri, G.; Mantenuto, P.; Giancaterini, L.; Cantalini, C. WO3 hydrogen resistive gas sensor and its wide-range current-mode electronic read-out circuit. *IEEE Sens. J.* **2013**, *13*, 2792–2798, doi:10.1109/JSEN.2013.2257732.
43. Boudiba, A.; Roussel, P.; Zhang, C.; Olivier, M.-G.G.; Snyders, R.; Debliquy, M. Sensing mechanism of hydrogen sensors based on palladium-loaded tungsten oxide (Pd-WO3). *Sensors Actuators, B Chem.* **2013**, *187*, 84–93, doi:10.1016/j.snb.2012.09.063.
44. Wicker, S.; Guiltat, M.; Weimar, U.; Hémeryck, A.; Barsan, N. Ambient Humidity Influence on CO Detection with SnO2 Gas Sensing Materials. A Combined DRIFTS/DFT Investigation. *J. Phys. Chem. C* **2017**, *121*, 25064–25073, doi:10.1021/acs.jpcc.7b06253.
45. Ma, S.; Hu, M.; Zeng, P.; Li, M.; Yan, W.; Qin, Y. Synthesis and low-temperature gas sensing properties of tungsten oxide nanowires/porous silicon composite. *Sensors Actuators B Chem.* **2014**, *192*, 341–349, doi:10.1016/j.snb.2013.10.121.
46. Yamaguchi, Y.; Imamura, S.; Nishio, K.; Fujimoto, K. Influence of temperature and humidity on the electrical sensing of Pt/WO3 thin film hydrogen gas sensor. *J. Ceram. Soc. Japan* **2016**, *124*, 629–633, doi:10.2109/jcersj2.15246.

D

Synergy of Experiment and Model for Reactive HiPIMS: Effect of Discharge Parameters on WO_x Composition and Deposition Rate

J. Rezek, T Kozák, **N. Kumar**, and S. Haviar

Journal of Physics D: Applied Physics 54 (2021) 125202 (11 pgs)

OPEN ACCESS
IOP Publishing
Journal of Physics D: Applied Physics
J. Phys. D: Appl. Phys. **54** (2021) 125202 (11pp)
https://doi.org/10.1088/1361-6463/abd1a3

Synergy of experiment and model for reactive HiPIMS: effect of discharge parameters on WO_x composition and deposition rate

J Rezek, T Kozák, N Kumar and S Haviar

Department of Physics and NTIS, European Centre of Excellence, University of West Bohemia, Univerzitní 8, 306 14, Plzeň, Czech Republic

E-mail: jrezek@ntis.zcu.cz

Received 1 October 2020, revised 19 November 2020
Accepted for publication 8 December 2020
Published 19 January 2021

Abstract

Reactive high-power impulse magnetron sputtering of tungsten oxide films using metallic tungsten target (72 mm in diameter) in argon-oxygen atmosphere (total pressure of 0.75 Pa) was carried out. The effect of various discharge parameters on the deposition rate and film oxygen concentration was investigated. Moreover, a model combining a reactive high-power impulse magnetron sputtering model and a discharge plasma model for the ionization region was successfully used for deeper insight into the effect of particular discharge parameters such as voltage pulse length (from 100 –800 μs), oxygen partial pressure (from 0.25–0.50 Pa) or the value of pulse-averaged target power density (from 2.5–500 W cm^{-2}). The results of the presented model, most notably trends in the target- and substrate oxide fraction, composition of particle fluxes onto the substrate, degree of W atom ionization or degree of O_2 molecule dissociation are discussed and put into context with experimentally measured quantities.

Keywords: reactive HiPIMS model, deposition rate, tungsten oxide

(Some figures may appear in colour only in the online journal)

1. Introduction

In the field of thin-film research and development, reactive high-power impulse magnetron sputtering (r-HiPIMS) has become the centre of attention in recent years. This is thanks to the ability of this technique to produce densified, high-quality defect-free oxide, nitride and oxynitride coatings [1–6]. The maximization of the deposition rate during r-HiPIMS has also been studied intensively and many approaches allow one to produce thin films at high deposition rates without sacrificing film quality [7, 8]. Much attention is also devoted to the investigation of processes connected with the presence of reactive gas (RG, typically oxygen and/or nitrogen) in the gas mixture and its interaction with the target and substrate surface. There are a few theoretical models describing the complex behaviour of r-HiPIMS plasma discharge that have been developed. In order to be applicable to high-power impulse magnetron sputtering (HiPIMS) discharge conditions, the models of conventional reactive sputtering (e.g. [9–14]) were extended to account (especially) for the ionization and return of sputtered metal atoms onto the target [15–19] and the dissociation of RG in the discharge plasma [15, 16, 19]. Some of those models simulated mainly the composition of the reactive surfaces and the balance of RG in the discharge chamber and the hysteresis effect [17, 20], while another focused on the simulation of the

discharge plasma during the pulse for a fixed composition of the reactive surfaces [19].

However, there are a lack of publications focused on the deeper understanding of the effects responsible for different film stoichiometry under different discharge conditions (namely voltage pulse length, pulse-averaged target power density, RG partial pressure,etc). In this publication, we clarify the relation between the abovementioned discharge parameters and WO_x properties, namely the deposition rate and oxygen content in the film. We have chosen the W-O system since WO_3 is a material that is in demand due to its many potential applications such as the active layer of hydrogen gas sensors [21, 22] and as part of electrochromic [23, 24] or gasochromic [25] devices. Moreover, tungsten oxide is a convenient choice thanks to its relatively high electrical conductivity that provides fair discharge stability. A new model of the reactive sputtering process was used to calculate the oxide coverage of the target and substrate, the deposition rate of films and other discharge parameters based on the experimental current–voltage waveforms. For the first time, this model combines an r-HiPIMS model [15] and a discharge plasma model for the ionization region (IR) in front of the sputtered target [26]. By comparing the simulated and experimental results and by evaluating the discharge parameters that cannot be easily measured, we explain the observed experimental trends.

2. Methodology

2.1. Film preparation

The tungsten oxide films were deposited using HiPIMS sputtering from a tungsten target with a diameter of 72 mm in a stainless-steel vacuum chamber (Leybold-Heraeus LH Z400) pumped by a turbomolecular pump (backed with a scroll pump) and a cold trap (cooled by liquid nitrogen). The magnetron was powered by a unipolar HiPIMS power supply (SIPP2000_USB, Melec GmbH). The base pressure before each deposition was below 1 mPa. The substrate-to-target distance was 70 mm. The depositions were carried out in a mixture of argon and oxygen. The working pressure was set to a constant value of 0.75 Pa. The average target power density was kept constant for all experiments (2.35 W cm^{-2}). During the experiments, the values of the oxygen partial pressure, p_{ox}, voltage pulse length, t_{on}, and/or pulse-averaged target power density, S_{da}, were varied.

All specimens were prepared on 10×10 mm^2 Si (100) substrates (625 μm thick). Before the deposition, the substrates were cleaned by sonication for 5 min in demineralized water and then isopropyl alcohol. The thickness of the films was within the range of 800–1000 nm.

2.2. Film characterization

The elemental composition of WO_x films was measured by wavelength-dispersive spectroscopy (WDS, Magnaray ThermoScientific) conducted in the chamber of a scanning electron microscope (SEM, Horiba, SU-70). The used primary electron energy was 10 keV, the standards of pure tungsten metal (99.95% purity) and hematite (Fe_2O_3, 99.97 purity) (Astimex Standards) were used for the quantification of W and O, respectively. For comparison with the model, it is important that the precision of the WDS method can be considered below 1 at.% for both W and O content. The trueness of our measurement, though, can be accurately estimated to be about 3 at.%, but this does not affect the observed trends. The deposition rate was calculated as the film thickness to deposition time ratio. The thickness was evaluated from SEM cross-sectional images.

2.3. The r-HiPIMS model

An r-HiPIMS model was used to simulate the HiPIMS deposition processes to gain more insight into the process parameters that are difficult to measure experimentally and to explain the measured dependencies. The model has two parts: (a) a model describing the time evolution of RG partial pressure and the composition of relevant surfaces (target, substrate and chamber walls), and (b) an IR model describing the time evolution of relevant plasma species densities in the region in front of the magnetron (IR) where the electrons are trapped by the magnetic field of the magnetron. Thus, this region is most relevant for capturing the ionization and RG dissociation processes in the discharge plasma. A schematic representation of the model is shown in figure 1.

The composition of the target, substrate and chamber walls is described using compound fraction Θ, which is the fraction of surface covered by stoichiometric compound ($\Theta = 0$ for pure metal while $\Theta = 1$ for stoichiometric compound) as in the well-known Berg model [9]. The compound fraction is calculated from balance equations of the form:

$$n_0 h x_c \frac{d\Theta}{dt} = \sum_j \Gamma_j, \tag{1}$$

where n_0 is the atomic density of the target material (pure metal), h is the layer thickness for which its composition is simulated (~one monolayer), x_c is the stoichiometry of the compound, i.e. the number of oxygen atoms for each metal atom in the compound, Θ is the compound fraction in the layer and Γ_j is the flux of oxygen atoms to or from the layer. The right-hand side accounts for all the processes changing the compound fraction, such as sputtering, chemisorption and ion implantation for the target, and deposition of sputtered atoms and chemisorption on the substrate and chamber walls. The ionization of the sputtered atoms and subsequent return and implantation into the target is also included. This was confirmed to be critical in r-HiPIMS where the probability of ionization of sputtered atoms is high [27]. This part of the model is based on our previous work [15, 16] where you can find more details about the model description of the balance equations. In this work, the model was extended by (a) adding the balance equation for the RG partial pressure in the vacuum chamber and (b) including several equidistant target layers allowing us to improve the accuracy of modelling the ion implantation. The former accounts for all gains and losses of RG molecules

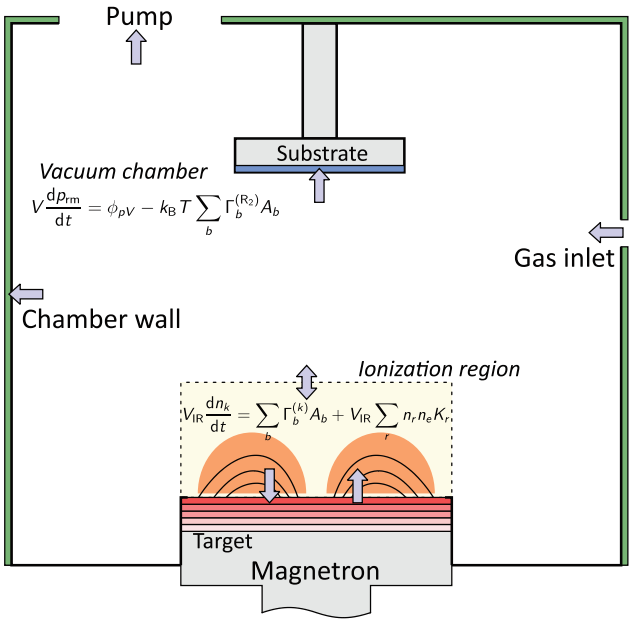

Figure 1. Scheme of the r-HiPIMS model. The model calculates (a) the fraction of reactive compound in several target layers (shown in red) and on the surface of the substrate (blue) and the chamber walls (green), (b) densities of plasma species (neutrals and ions) in the IR and (c) the partial pressure of RG in the vacuum chamber. The model also evaluates the fluxes of plasma species to and from the target and onto the substrate (indicated by arrows). Symbols are defined in the text.

in the vacuum chamber and allows us to calculate the RG partial pressure for a varying RG flow rate. The latter allows us to calculate a depth-resolved composition of the target. Strict mass conservation is enforced for the target layers that are coupled by the transport of material between them. As the target material is sputtered away from the target surface, the oxygen in the target is moved across the layers towards the target surface. On the other hand, when target material ions are implanted into the target, the oxygen in the target layers below the depth of implantation is moved deeper into the target.

The IR model calculates the plasma species densities in the IR during a period of the HiPIMS pulse. This is a volume-averaged model assuming constant densities in the IR, similar to our previous work [26]. The species include Ar, M, R_2, R, R_s, Ar^+, M^+, $R_2{}^+$ and R^+, where M stands for the sputtered metal atom, R_2 for the RG molecule, R for the RG atom and R_s for the (fast) RG atom sputtered from the target. The IR model equations have the form:

$$V_{IR}\frac{dn_k}{dt} = \sum_b \Gamma_b^{(k)} A_b + V_{IR} \sum_r n_r n_e K_r(T_e), \qquad (2)$$

where the left-hand side is the number change of species k in the IR, the first term on the right-hand side accounts for changes due to the transport of particles from the IR and the second term accounts for the change of particle density due to reactions (mainly, but not exclusively, those involving electrons). A necessary parameter of the IR model is the fraction of ions created in the IR that return onto the target. This return probability, β, is assumed to be constant and equal for all species. As the rate of ionization of neutral species depends on the electron temperature, T_e, and the ion density determines the ion current onto the target, the model uses a known (user input) target current waveform to calculate $T_e(t)$ assuming a known (constant) secondary electron emission yield. This $T_e(t)$ then determines all the electron reaction constants in the particle balance equations. The two parts of the simulation are coupled together as follows. The RG partial pressure and the compound fractions on the target, substrate and chamber walls calculated for a given time by the reacting surface model enter the IR model. They are assumed to be constant during a single HiPIMS pulse period, see [15, 28]. The IR model then provides the densities of species in the IR and the corresponding total fluxes of species onto the target, substrate and chamber walls, which are used in the model for the reactive surfaces. Thus, the two parts of the model are solved repeatedly with mutual exchange of data to integrate in time. It should be noted that due to the significantly different characteristic time scales of the two models (typically μs for the IR model compared to ms or longer for the reactive surface model), it is not reasonable to solve the coupled equations of both models simultaneously.

In the present paper, the model is used to simulate depositions of WO_3. The geometrical parameters of the model, such as the chamber volume, target diameter and target–substrate distance were set according to the experiments. The oxygen partial pressure is set constant as in the experiments, with the total pressure always 0.75 Pa. The necessary material parameters of the model were set according to table 1. The sputtering yield of W from a W target, Y_{mm}, and the implantation depth profiles for W and O atoms into a W target (not included in the table) were calculated by SDTrimSP [29] as a function of ion energy. Due to the lack of reliable data for sputtering yields from the compound targets, we assumed that the sputtering

Table 1. Parameters related to the target material (W) used by the reactive model. E is the energy of ions incident on the target, Θ_t is target oxide fraction.

Parameter	Value	Unit
W density	19.24	g cm^{-3}
WO_3 density	7.16	g cm^{-3}
O_2 sticking coefficient on W	0.03	
O sticking coefficient on W	1.0	
W sputtering yield from W, Y_{mm}, by Ar^+	$\frac{3.72\left(\frac{E}{71}-1\right)^{1.01}}{22.3+\left(\frac{E}{71}-1\right)^{1.01}}$	
W sputtering yield from W, Y_{mm}, by W^+	$\frac{4.12\left(\frac{E}{100}-1\right)^{1.3}}{27.0+\left(\frac{E}{100}-1\right)^{1.3}}$	
W sputtering yield from W, Y_{mm}, by O^+	$\frac{1.23\left(\frac{E}{78}-1\right)^{1.05}}{13.9+\left(\frac{E}{78}-1\right)^{1.05}}$	
W sputtering yield as function of Θ_t	$Y_{mm}\left(1-\Theta_t+\frac{\Theta_t}{7}\right)$	
O sputtering yield as function of Θ_t	$Y_{mm}\Theta_t$	
Ion return probability	0.6	
Gas temperature	300	K

Table 2. Summary of reactions implemented in the discharge plasma model for the IR.

Reaction	Rate constant ($m^{-3}s^{-1}$)	Reference
$e + Ar \rightarrow 2e + Ar^+$	$2.34 \times 10^{-14} T_e^{0.59} e^{-\frac{17.4}{T_e}}$	[34]
$e + W \rightarrow 2e + W^+$	$5.61 \times 10^{-14} T_e^{0.58} e^{-\frac{9.82}{T_e}}$	Calculated from the cross-section from [35]
$e + O_2 \rightarrow 2e + O_2^+$	$2.34 \times 10^{-15} T_e^{1.03} e^{-\frac{12.3}{T_e}}$	[36]
$e + O_2 \rightarrow e + 2O$	$6.86 \times 10^{-15} e^{-\frac{6.29}{T_e}}$	[34]
$e + O_2^+ \rightarrow 2O$	$2.2 \times 10^{-14} T_e^{-0.5}$	[37]
$e + O_2 \rightarrow 2e + O + O^+$	$1.88 \times 10^{-16} T_e^{1.70} e^{-\frac{16.8}{T_e}}$	[36]
$e + O \rightarrow 2e + O^+$	$9.0 \times 10^{-15} T_e^{0.7} e^{-\frac{13.6}{T_e}}$	[38]

yield of W from WO_3, $Y_{mc} = Y_{mm}/7$, and the sputtering yield of O from WO_3, $Y_{rc} = 7\ Y_{mc}$, to take into account preferential sputtering of O from WO_3 [30]. These fixed values were estimated based on a comparison of experimental and simulated deposition rates of WO_3 and W. The sputtering yield at arbitrary compound fraction Θ_t, is calculated by linear interpolation between the sputtering yields from W and WO_3. The ion return probability is an unknown parameter for the simulated discharge setup. We tested a broad range of values from 0.3–0.9 based on the paper [31] where possible values of the ion return probability span this range depending on the target voltage. The value of 0.6 was used for the final series of calculations in the hope that this is a reasonable mean value suitable for all analyzed regimes, although [32, 33] suggest values closer to our upper limit of 0.9. As will be shown in the results, the particular value of the ion return probability has a weak effect on the modelling results.

The reactions in the discharge plasma and the corresponding reaction rate constants are summarized in table 2. The model is calculated from initial conditions until a steady state is reached that corresponds to the deposition-averaged conditions obtained in the experiments.

To summarize, the model uses experimental geometry, current and voltage waveforms, Ar and oxygen flow rate or partial pressure, ion return probability and other material parameters (densities, sticking coefficients, sputtering yields, implantation profiles) as input. It solves balance equations for several plasma species in the IR of the discharge plasma and balance equations for oxygen in the target, substrate, chamber walls and chamber volume. Most notably, the model takes into account (a) the ionization of sputtered atoms and the dissociation of oxygen in the discharge plasma and calculates those based on the electron density and temperature, (b) the dissociation of oxygen in the discharge and different sticking coefficients for oxygen atoms and molecules, (c) chemisorption as well as implantation of oxygen into the target and (d) the return of ionized sputtered atoms onto the target and their implantation into subsurface layers of the target. The model is used to calculate the composition of the target and substrate, deposition rate of films and densities of species in the discharge plasma.

Finally, we mention the limitations of the current model. The model is based on the volume-averaged approach (assumes homogeneous density in the IR and homogeneous oxide fraction in the studied surfaces). Thus, it does not resolve spatial inhomogeneities of the calculated quantities and is inherently less accurate than any spatially resolved simulation. Therefore, negative ions are not included now, although their role in r-HiPIMS has been studied [39]. Some of the material parameters such as sputtering yields and sticking coefficients are not well known and can vary significantly based on fine details of the experimental system. Therefore, the absolute values of the calculated quantities should be taken with a pinch of salt. Instead, we focus on observing the trends and make conclusions based on the comparison of model results among different regimes. The oxide fraction Θ is inherently limited to values $\Theta < 1$, and for oxygen-rich conditions, Θ slowly approaches unity. Therefore, in contrast to reality, the model cannot give over-stoichiometric composition of a surface, and, for compositions close to the stoichiometric oxide, the corresponding Θ is likely to be underestimated. The deposition rate of films was calculated from the flux of W atoms onto the substrate assuming a fixed density of the film equal to the density of the stoichiometric oxide, while in reality the density of films is expected to vary with the exact film composition. These limitations of the model will be considered in the ongoing discussion.

3. Results and discussion

In the following, we present the experimentally measured and calculated deposition rate and oxygen content in the film obtained under different deposition conditions. Phenomena determining the observed trends are explained using different model output quantities, such as target- and substrate oxide fraction, degree of O_2 dissociation, degree of W atom ionization, composition of particle flux onto the substrate or time evolution of particle densities in front of the target. First, we discuss the different behaviour of the reactive DC and HiPIMS processes. Next, we report on the effect of pulse-averaged target power density on the abovementioned quantities. In the last section, we discuss the effect of the voltage pulse length at a constant pulse-averaged target power density.

3.1. Comparison of DC and HiPIMS discharge regimes

In figure 2, a comparison of the deposition rate (a) and oxygen content in the film (b) as a function of p_{ox} is shown. In the case of DC, the deposition rate decreases with increasing p_{ox}, which is the expected behaviour observed for many target materials. This is explained by the fact that the oxide coverage of the target surface increases with the increasing oxygen partial pressure and, consequently, the sputtering rate of the metal atoms decreases [30, 40]. This is confirmed by the model (not shown), which implements a pre-set dependence of the sputtering yield on the target oxide coverage, Θ_t. This

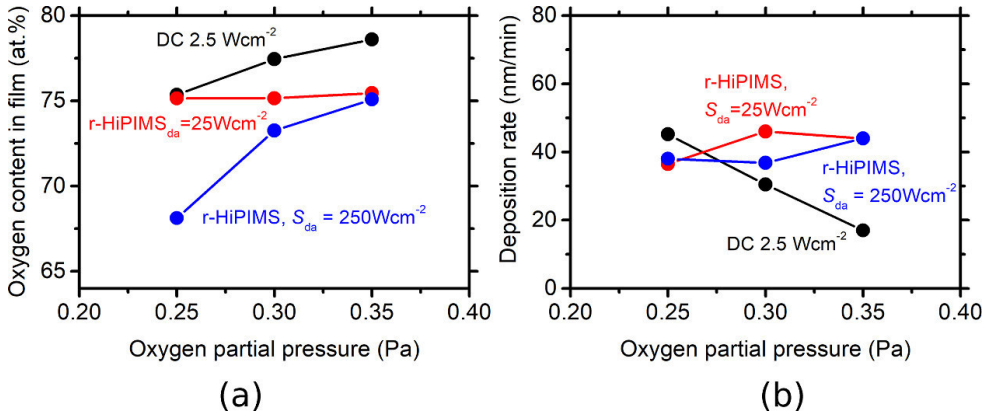

Figure 2. Deposition rate (a), and oxygen content in the film (b) as a function of oxygen partial pressure for three different discharge regimes ($t_{on} = 800$ μs in the case of r-HiPIMS deposition).

is also qualitatively in agreement with the increasing oxygen content in the film, C_{ox}, 75.4 at.% at $p_{ox} = 0.25$ Pa to 78.6 at.% at $p_{ox} = 0.35$ Pa, which is correlated with Θ_s calculated by the model.

In the case of r-HiPIMS, the situation is more complicated. Higher $S_{da} = 250$ W cm^{-2} ('high-power regime') leads to a gradual increase of C_{ox} from 68.1 at.% to 75.1 at.% with increasing p_{ox} (similar to the DC regime), whereas, C_{ox} is almost constant (~75.2 at.%) for the low value of $S_{da} = 25$ W cm^{-2} ('low-power regime'). This is not observed in the model results where Θ_s monotonously increases with the oxygen partial pressure for both $S_{da} = 25$ W cm^{-2} and 250 W cm^{-2}. In contrast to the DC case, there is no decrease in deposition rate for both the low- and high-power regime. Moreover, for p_{ox} of 0.30 and 0.35 Pa, the deposition rate in the HiPIMS case is higher than in the DC case. This potentially surprising result is not entirely unusual. It was also reported by Hemberg *et al* for tungsten oxide [41] and Hála *et al* for niobium oxide [42]. This is primarily caused by a lower oxide fraction on the target (see figure 3). The model results indicate that the oxide coverage of the target decreases with increasing target power density (in a pulse in the case of HiPIMS). Moreover, in figure 3, one of the r-HiPIMS benefits is clearly seen; the Θ_s/Θ_t ratio (at given p_{ox}) increases with increasing S_{da}. This means for higher S_{da} the discharge is close to the desired regime; production of stoichiometric films, while the target is as metallic as possible.

There are several processes that affect Θ_t and they all change simultaneously when the pulse-averaged target power density in a pulse is changed. Figure 4 shows the effect of the ion return probability on the oxide coverage for the DC and high-power regime. It should be noted that realistic values of the ion return probability probably lie in the range of 0.5–0.9 [31, 32]. Overall, for the given conditions, the effect of pre-selected ion return probability is weak and does not change the trends observed, especially the fundamental difference between the DC and HiPIMS case. More specifically, the calculated oxide fraction changes by a few percentage points and the calculated deposition rate (not shown) decreases by 5% in the DC case and 15% for the HiPIMS high-power case

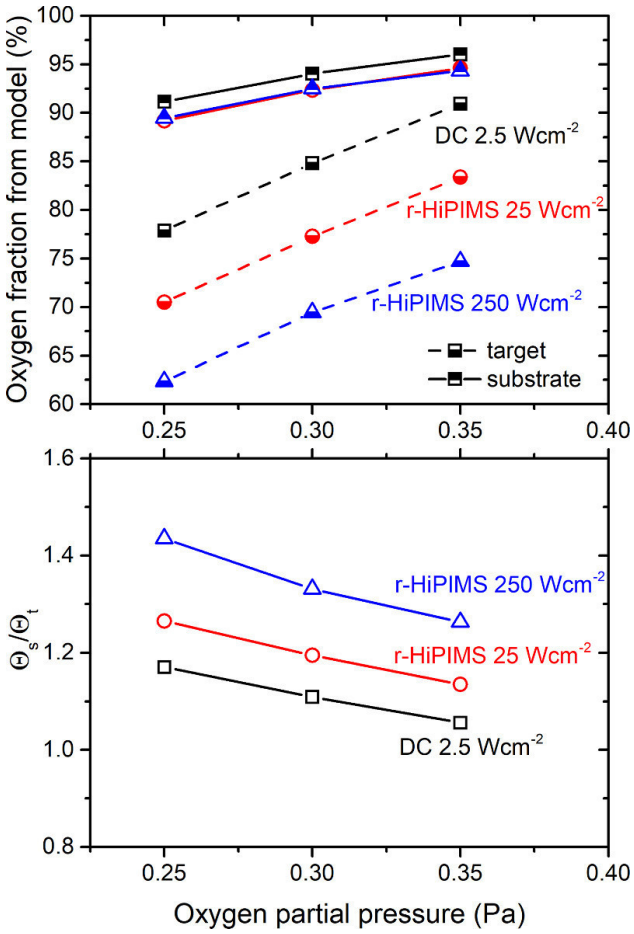

Figure 3. Top panel: calculated oxide fraction on the substrate (half-up symbols) and the target (half-down symbols) as a function of oxygen partial pressure for three different discharge regimes. Bottom panel: calculated ratio of the substrate and target oxide fraction as a function of oxygen partial pressure for three different discharge regimes ($t_{on} = 800$ μs in the case of r-HiPIMS).

when the ion return probability increases from 0.6 to 0.9. In the DC case, Θ_t slightly increases and Θ_s slightly decreases

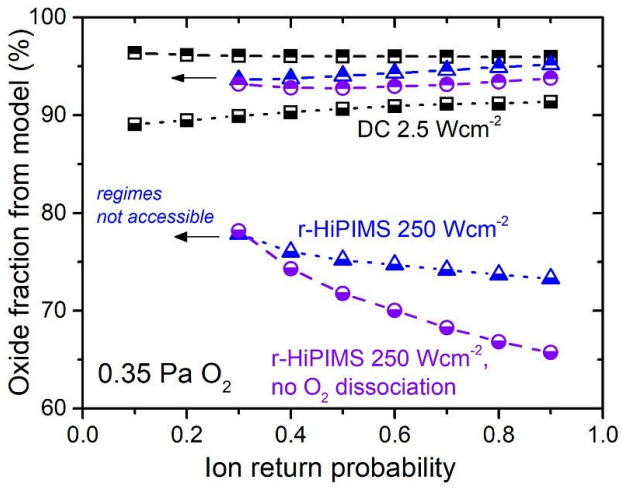

Figure 4. Calculated oxide fraction on the substrate (half-up symbols) and the target (half-down symbols) as a function of the ion return probability calculated for the DC regime (2.5 W cm^{-2}, black symbols) and the high-power regime ($S_{da} = 250$ W cm^{-2}, $t_{on} = 800$ μs, blue symbols) and the O_2 partial pressure of 0.35 Pa. In addition, simulation results for the high-power regime with no O_2 dissociation are shown by purple symbols.

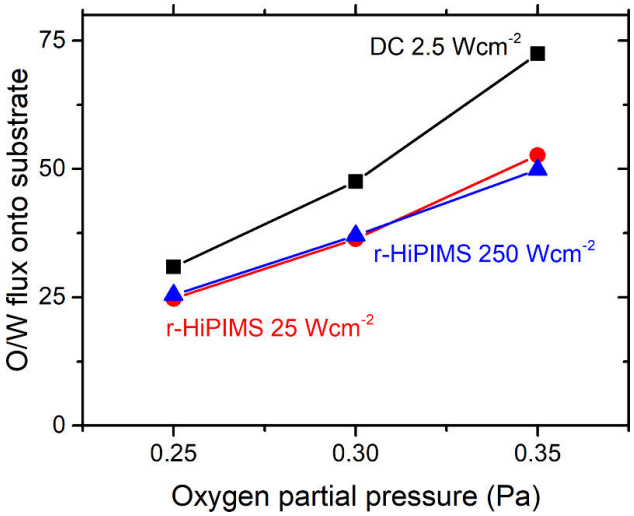

Figure 5. Calculated ratio of oxygen and tungsten particle fluxes (atoms and ions) onto the substrate as a function of oxygen partial pressure for three different discharge regimes ($t_{on} = 800$ μs in the case of r-HiPIMS deposition).

with an increasing ion return probability. As the sputtering rate of W and its ionization are low in this case, this trend can be explained by the increased attraction of O_2^+ ions and their implantation into the target. On the other hand, in the HiPIMS case, Θ_t decreases and Θ_s increases with the increasing ion return probability, see the blue curves. In this case, the degree of ionization of W in the discharge is high (~70% for $S_{da} = 250$ W cm^{-2} resulted from the model, not shown) and W^+ ions reimplanted into the target effectively decrease the oxide coverage of the target.

If oxygen dissociation was neglected (see the violet curve), the decrease of Θ_t would be even more pronounced. However, O_2 dissociation increases the reactivity of O atoms generated in the high-density plasma during the pulse and, thus, increases Θ_t and partly compensates the effect of target metallization by W^+ ion implantation (see again the blue curve, which includes both W^+ implantation and O_2 dissociation). Overall, the return of W ions onto the target is a significant factor causing the decrease in Θ_t in r-HiPIMS discharges in agreement with recent studies [27].

As mentioned, a fraction of the sputtered metal atoms returns onto the target as ions. However, there is considerable increased flux left on the substrate, which is not complemented by a sufficiently high flux of O atoms. This leads to a slightly lower Θ_s when compared to the DC case. Figure 5 shows that the ratio of O/W fluxes onto the substrate decreases when the discharge regime is changed from DC to HiPIMS. Here, the difference between the low- and high-power regime is negligible.

As can be observed in figure 6, the current waveform for the high-power regime has a typical shape indicating gas rarefaction [43, 44] in front of the target. Note that this effect is difficult to calculate accurately with a volume-averaged model of the discharge plasma [45] and it cannot be adequately implemented in the present model. In the case of reactive sputtering, not only argon but also RG (oxygen in our case) particles (molecules, atoms and ions) are pushed away from the volume between the target and the substrate and, thus, a lower amount of oxygen particles reacts with the arriving W species on the substrate surface. Therefore, it is suggested that gas rarefaction in r-HiPIMS (especially in the high-power regime) also contributes to the lower oxygen concentration in the films, which is in agreement with the measured film elemental composition, see figure 2(b).

3.2. *Pulse-averaged target power density effect*

In this section, the effects of pulse-averaged target power density (ranged from 100–500 W cm^{-2} at constant $t_{on} = 100$ μs) on oxygen content in the film and deposition rate will be discussed. Depositions and model calculations were carried out under two different oxygen partial pressures: 0.25 Pa ('low-oxygen regime') and 0.50 Pa ('high-oxygen regime').

Experimentally determined oxygen content in the film, C_{ox}, and model calculations for oxide fraction formed on the substrate and target surface are presented in figure 7. As can be expected, C_{ox} is significantly higher for the high-oxygen regime compared to the low-oxygen regime. With increasing S_{da}, C_{ox} slightly decreases for both low- and high-oxygen regimes, i.e. the film becomes more metallic. In accordance with that, the target surface is also more metallic with increasing S_{da}, as confirmed by the calculated oxide fraction on the target surface (Θ_t), see top panel of figure 7. As expected, the calculated Θ_t is also systematically higher for the high-oxygen regime. On the other hand, the trend for C_{ox} is not fully confirmed by the model; Θ_s is practically constant for the high-oxygen regime, but it slightly increases for the low-oxygen regime. This indicates that the model overestimates

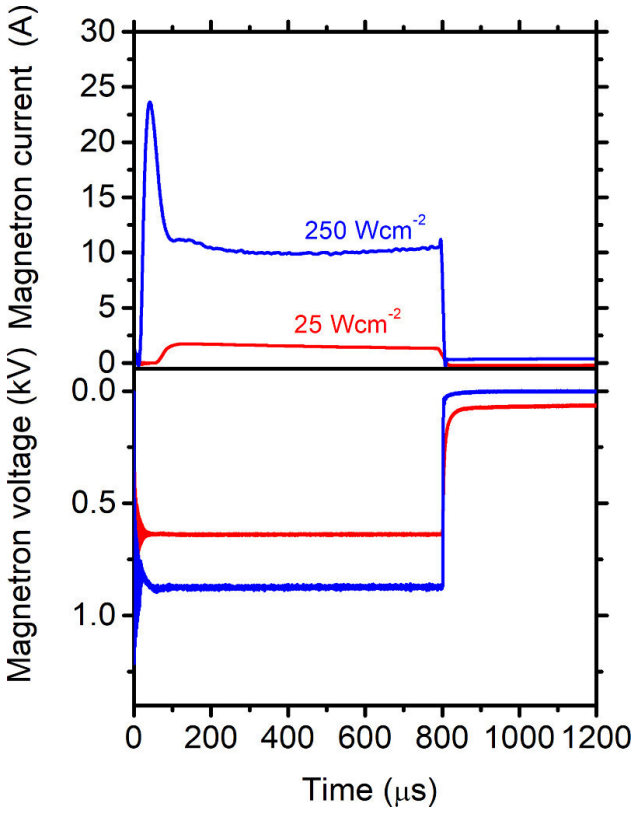

Figure 6. Magnetron current and voltage waveforms for low- and high-power regimes at constant $p_{ox} = 0.35$ Pa.

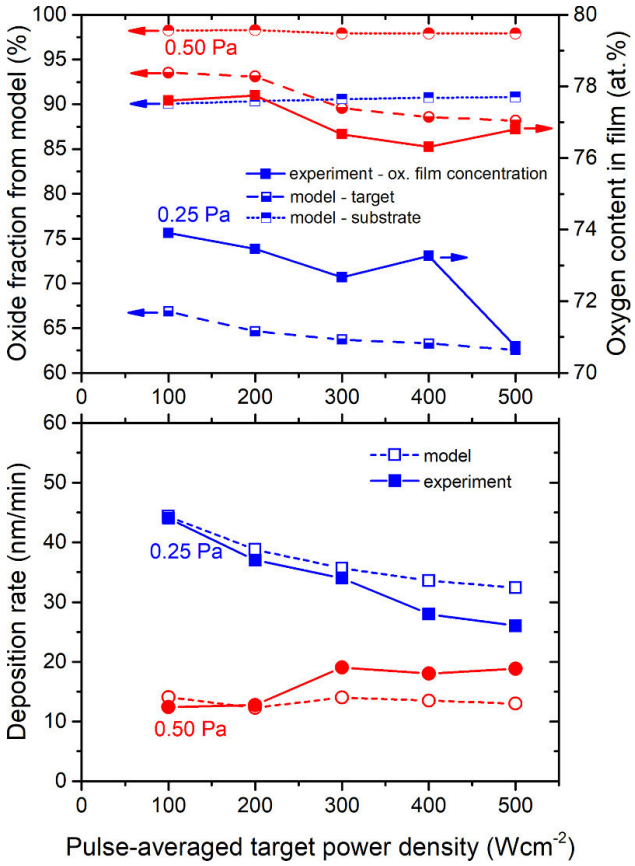

Figure 7. Top panel: calculated oxide fraction (dashed lines) on the substrate (half-up symbols) and the target (half-down symbols) and experimentally measured oxygen content in the film (solid lines) as a function of S_{da} for two values of p_{ox} (0.25 and 0.50 Pa). Bottom panel: calculated (dashed lines) and experimentally measured (solid lines) deposition rate as a function of S_{da} for two values of p_{ox} (0.25 and 0.50 Pa).

the flux of oxygen with respect to the flux of W particles towards the substrate. The bottom panel in figure 7 depicts trends in deposition rate and also shows qualitative compliance between experimentally measured and calculated deposition rates. For the low-oxygen regime, the deposition rate decreases with increasing S_{da}, which is mainly caused by increased ion return onto the target, while the sputtering rate of metals from the target is constant (indicated by the model results, not shown). For the high-oxygen regime, the experimental deposition rate slightly increases with increasing S_{da}, while the calculated deposition rate remains practically constant. This can be explained by the decrease in Θ_t, see figure 7 (top panel), which results in a slight increase in the sputtering rate of metals from the target. At the same time, the change in ion return flux is less pronounced in the presented range of S_{da} values (indicated by the model results, not shown). Figure 8 shows the calculated flux of W and O particles (atoms and ions) onto the substrate. For the high-oxygen regime, the flux of O decreases with increasing S_{da}, while the flux of W remains practically constant. Thus, the O/W flux ratio decreases and, therefore, Θ_s decreases with increasing S_{da}. On the other hand, for the low-oxygen regime, both O and W fluxes decrease and the O/W flux ratio slightly increases leading to the observed increase in Θ_s.

Figure 9 shows the degree of O_2 dissociation and W ionization in front of the target as calculated by the IR model. As expected, we observe an increase in both quantities as S_{da} increases. It is interesting to note that for the high-oxygen regime, the W ionization degree between 200–500 W cm^{-2} does not increase as fast as for the low-oxygen regime. It could be explained by the fact that for the high-oxygen regime, the high fraction of O_2 in the discharge is dissociated ($E_{diss} = 5.15$ eV) and/or ionized, which consumes part of the energy delivered during the pulse, which cannot be used for W ionization ($E_{iz} = 7.86$ eV). Thus, the lower amount of W atoms in the high-oxygen regime (because fewer W atoms are sputtered from the target, see higher Θ_t in figure 7) and the not so high ionization of W leads to lower losses of sputtered W by the ion return effect, resulting in the non-decreasing dependence of the flux of W onto the substrate on S_{da} (figure 8).

The experimentally measured deposition rate decreases from 44 to 26 nm min^{-1}, while it slightly increases from 12 to 19 nm min^{-1} with increasing S_{da} for the low- and high-oxygen regime, respectively. These trends are in very good agreement with the model calculations. The decrease in deposition rate for the low-oxygen regime is well known in non-reactive HiPIMS [46]. Here, it can be mainly attributed to the return of ionized metal atoms onto the target as the degree of ionization

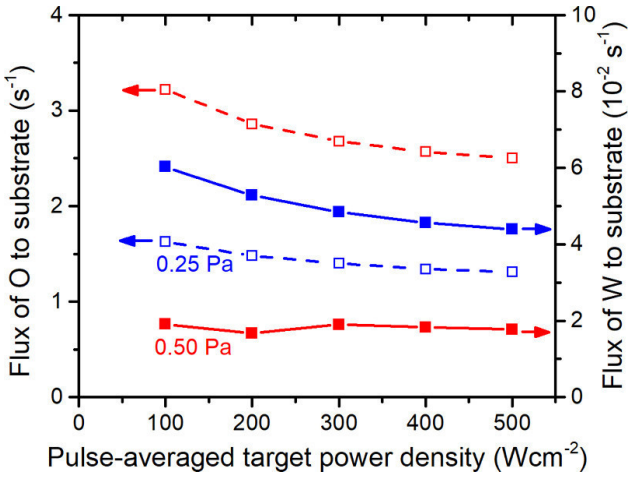

Figure 8. Calculated fluxes of O (dashed lines, empty symbols) and W (solid lines, full symbols) particles (atoms and ions) onto the substrate as a function of the pulse-averaged target power density for the O_2 partial pressure of 0.25 Pa (blue) and 0.50 Pa (red).

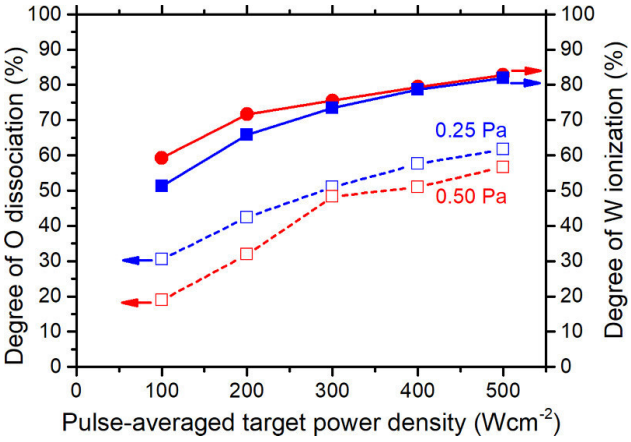

Figure 9. Calculated degree of oxygen molecule dissociation (dashed lines) and tungsten atom ionization (solid lines) as a function of S_{da} for two values of p_{ox} (0.25 and 0.50 Pa).

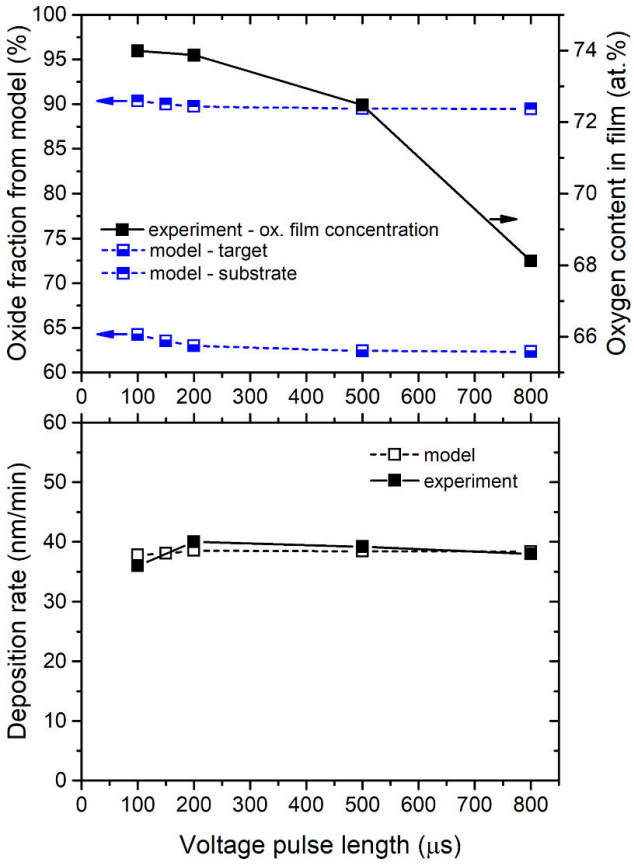

Figure 10. Top panel: calculated oxide fraction (dashed lines) on the substrate (half-up symbols) and the target (half-down symbols) and experimentally measured oxygen content in the film (solid lines) as a function of t_{on} at constant $p_{ox} = 0.25$ Pa. Bottom panel: calculated (dashed line) and experimentally measured (solid line) deposition rate as a function of t_{on} at constant $p_{ox} = 0.25$ Pa.

of metal atoms increases with increasing target power density, see figure 9. The model estimates the degree of W ionization in the discharge plasma during the pulse to increase from 50% to 80% when S_{da} increases from 100 to 500 W cm^{-2}.

Although this ion return effect is also present in r-HiPIMS, the situation is more complicated. First, the film density depends on the film composition and, thus, the deposition rate of metal atoms does not exactly correspond to the deposition rate of films measured in nm/min. Second, the sputtering rate of metal atoms from the target is affected by its oxide coverage which can, in principle, be either increasing or decreasing with the increase in S_{da}, depending on the complex balance between metal sputtering and oxygen implantation.

It is interesting that both the deposition rate and film oxygen concentration decrease with increasing S_{da} simultaneously. In other words, despite the fact that films (as well as the target, according to the model – see target oxide fraction in figure 7) are more metallic for higher S_{da}, the deposition rate is lower compared with lower S_{da}. This is in contrast to the situation in conventional DC, RF or mid-frequency reactive magnetron sputtering where the decrease in oxygen content in the film is always connected with an increase in deposition rate [47]. Again, this is a consequence of the increased return of W^+ ions onto the target, which effectively lowers the flux of W atoms onto the substrate.

As mentioned above, the deposition rate in the case of the high-oxygen regime slightly increases with increasing S_{da}, which is the opposite behaviour to that observed in the low-oxygen regime. The calculated deposition rate remains practically constant with increased S_{da}, in general. This is also related to the above-discussed fact that the flux of W onto the substrate is practically constant for the increasing S_{da}. However, there is a momentary increase in the calculated deposition rate for S_{da} increasing from 200 to 300 W cm^{-2}, which is also observed in the experimental results. For the target power density of 300 W cm^{-2}, the model shows a slight increase in the W flux onto the substrate, which leads to a decrease in the oxide fraction on the substrate and a small increase in the deposition rate.

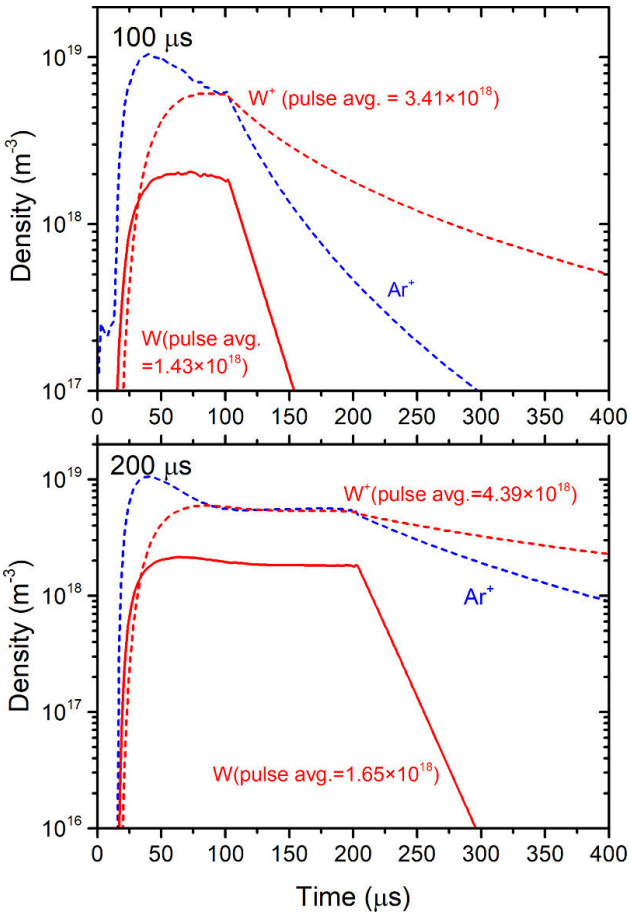

Figure 11. Calculated time evolutions of Ar^+, W and W^+ densities in the IR in front of the target for $t_{on} = 100$ μs (upper box) and $t_{on} = 200$ μs (bottom box) at $p_{ox} = 0.25$ Pa. Calculated pulse-averaged density for W and W^+ is given.

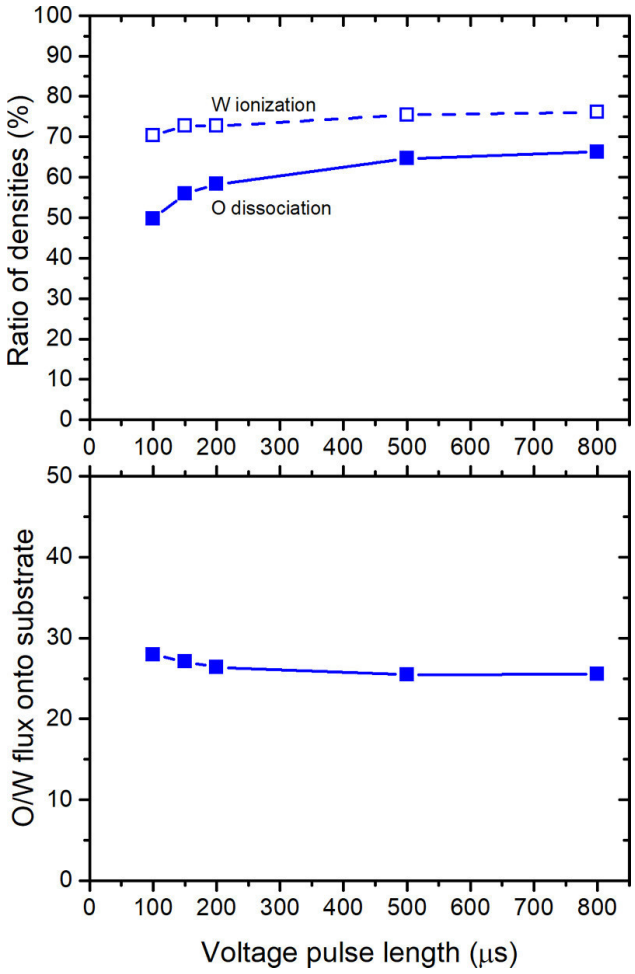

Figure 12. Top panel: calculated degree of W atom ionization (dashed line) and O_2 dissociation (solid line) as a function of t_{on} at $p_{ox} = 0.25$ Pa. Bottom panel: calculated ratio of oxygen and tungsten particle fluxes (atoms and ions) onto the substrate as a function of t_{on} at $p_{ox} = 0.25$ Pa.

3.3. Voltage pulse length effect

Finally, we report on the effect of voltage pulse length, t_{on}, (at constant $p_{ox} = 0.25$ Pa, constant $S_{da} \sim 250$ W cm^{-2} and constant period-averaged target power density of 2.35 W cm^{-2}). Thus, we have varied the repetition frequency to keep both pulse- and period-averaged target power densities constant. This complements the previous section where S_{da} was varied at constant t_{on}. The main results are presented in figure 10. The deposition rate slightly increases from 35 to 40 nm min^{-1} when t_{on} increases from 100 to 200 μs. The same trends were presented, for example, by [48, 49] in r-HiPIMS depositions of HfO_2 and WO_3 when t_{on} increases from 80 to 200 μs. This is also in very good agreement with the deposition rate calculated by the model. This could be caused by the lower total amount of W and W^+ particles produced during the pulse for $t_{on} = 100$ μs (see values of mean particle densities in figure 11). There is always a time delay between the start of the voltage pulse and the production of sputtered/ionized target particles. In our case, this delay is approximately 20 μs for all voltage pulse lengths, so there is practically no sputtering up to 20 μs into the pulse, i.e. up to 20% of the pulse-on time is 'wasted' for $t_{on} = 100$ μs, while it is only 10% for $t_{on} = 200$ μs and it further decreases for longer pulse lengths. The slight decrease in deposition rate from 40 to 38 nm min^{-1} when t_{on} is increased from 200 to 800 μs (also visible in the calculated trend, see figure 10 bottom panel) is caused mostly by a higher degree of ionization of sputtered W atoms (see figure 12 top panel) and thus more pronounced ion return of W^+ onto the target.

A monotonous decrease in C_{ox} from 74.0 at.% to 68.1 at.% is observed (figure 10) with increasing t_{on} from 100 to 800 μs. Presumably, this increases the film mass density, which might also explain the abovementioned decrease in the deposition rate for voltage pulse length increasing up to 800 μs.

For the increasing voltage pulse length, the simulations predict a slightly decreasing oxide fraction (figure 10 top panel) on the target and substrate, i.e. the films tend to be more metallic. This is in qualitative agreement with the experiment, although the decrease in oxide fraction in the substrate is not nearly as pronounced as the experimental oxygen content in

the film. We suggest that (reactive) gas rarefaction in front of the target due to the sputtering wind effect can cause this more pronounced decrease in film stoichiometry. This effect is not included in the simulation due to its spatial complexity.

The pulse-averaged degree of W ionization and O dissociation, as calculated by the model, are shown in figure 12 (top panel). The increase in W ionization facilitates increased metallization of the target as a result of more ions returning to the target. The bottom panel of the figure shows that the ratio of O/W atoms arriving onto the substrate decreases with increasing t_{on}, which results in the observed decrease of O content in the films.

4. Conclusion

The presented results show the successful application of a model combining an r-HiPIMS model with a discharge plasma model for the IR. It was used in conjunction with experimental results obtained for r-HiPIMS of WO_x films. The main results could be summarized as follows. It was found that there is a fundamental difference between reactive DC and HiPIMS of WO_x films. In the case of DC, the deposition rate decreases with oxygen partial pressure (as expected) whereas it is almost constant for HiPIMS deposition. A higher value of pulse-averaged target power density (at constant voltage pulse length) leads to a decrease in oxygen content in the film for both low- and high-oxygen regime. The deposition rate slightly decreases for the low-oxygen regime whereas it slightly increases for the high-oxygen regime (confirmed by the model quantitatively), mostly due to the lower amount of W^+ and thus lower losses caused by the ion return effect. Finally, it was found that longer voltage pulses lead to lower oxygen content in the film, probably due to more effective oxygen rarefaction caused by the sputtering wind. For short pulse (<100 μs), the deposition rate is lowered due to a significant role of 'wasted' time (~20 μs; time delay between creation of the plasma discharge and release of a significant amount of W atoms from the target). For longer pulses (>200 μs), there is a higher degree of W atom ionization and thus the deposition rate is lowered due to a more pronounced ion return effect.

Acknowledgments

This work was supported by the Czech Science Foundation under Project No. 19-14011S.

ORCID iDs

J Rezek https://orcid.org/0000-0002-2698-8753
S Haviar https://orcid.org/0000-0001-6926-8927

References

[1] Belosludtsev A, Houška J, Vlček J, Haviar S, Čerstvý R, Rezek J and Kettner M 2017 Structure and properties of Hf-O-N films prepared by high-rate reactive HiPIMS with smoothly controlled composition *Ceram. Int.* **43** 5661–7
[2] Vlček J, Belosludtsev A, Rezek J, Houška J, Čapek J, Čerstvý R and Haviar S 2016 High-rate reactive high-power impulse magnetron sputtering of hard and optically transparent HfO_2 films *Surf. Coat. Technol.* **290** 58–64
[3] Rezek J, Vlček J, Houška J and Čerstvý R 2014 High-rate reactive high-power impulse magnetron sputtering of Ta-O-N films with tunable composition and properties *Thin Solid Films* **566** 70–7
[4] Rezek J, Novák P, Houška J, Pajdarová A D and Kozák T 2019 High-rate reactive high-power impulse magnetron sputtering of transparent conductive Al-doped ZnO thin films prepared at ambient temperature *Thin Solid Films* **679** 35–41
[5] Hovsepian P E and Ehiasarian A P 2019 Six strategies to produce application tailored nanoscale multilayer structured PVD coatings by conventional and high power impulse magnetron sputtering (HIPIMS) *Thin Solid Films* **688** 137409
[6] Hovsepian P E, Ehiasarian A P, Purandare Y P, Mayr P, Abstoss K G, Mosquera Feijoo M, Schulz W, Kranzmann A, Lasanta M I and Trujillo J P 2018 Novel HIPIMS deposited nanostructured CrN/NbN coatings for environmental protection of steam turbine components *J. Alloys Compd.* **746** 583–93
[7] Vlček J, Rezek J, Houška J, Čerstvý R and Bugyi R 2013 Process stabilization and a significant enhancement of the deposition rate in reactive high-power impulse magnetron sputtering of ZrO_2 and Ta_2O_5 films *Surf. Coat. Technol.* **236** 550–6
[8] Rezek J, Houška J, Procházka M, Haviar S, Kozák T and Baroch P 2018 In-Ga-Zn-O thin films with tunable optical and electrical properties prepared by high-power impulse magnetron sputtering *Thin Solid Films* **658** 27–32
[9] Berg S, Blom H-O, Larsson T and Nender C 1987 Modeling of reactive sputtering of compound materials *J. Vac. Sci. Technol.* A **5** 202
[10] Berg S and Nyberg T 2005 Fundamental understanding and modeling of reactive sputtering processes *Thin Solid Films* **476** 215–30
[11] Kubart T, Kappertz O, Nyberg T and Berg S 2006 Dynamic behaviour of the reactive sputtering process *Thin Solid Films* **515** 421–4
[12] Güttler D, Abendroth B, Grötzschel R, Möller W and Depla D 2004 Mechanisms of target poisoning during magnetron sputtering as investigated by real-time *in situ* analysis and collisional computer simulation *Appl. Phys. Lett.* **85** 6134–6
[13] Depla D, Heirwegh S, Mahieu S and De Gryse R 2007 Towards a more complete model for reactive magnetron sputtering *J. Phys. D: Appl. Phys.* **40** 1957–65
[14] Strijckmans K, Schelfhout R and Depla D 2018 Tutorial: hysteresis during the reactive magnetron sputtering process *J. Appl. Phys.* **124** 241101
[15] Kozák T and Vlček J 2016 A parametric model for reactive high-power impulse magnetron sputtering of films *J. Phys. D: Appl. Phys.* **49** 055202
[16] Kozák T and Vlček J 2017 Dynamics of processes during the deposition of ZrO_2 films by controlled reactive high-power impulse magnetron sputtering: a modelling study *J. Appl. Phys.* **122** 043304
[17] Kadlec S and Čapek J 2017 Return of target material ions leads to a reduced hysteresis in reactive high power impulse magnetron sputtering: model *J. Appl. Phys.* **121** 171910
[18] Strijckmans K, Moens F and Depla D 2017 Perspective: is there a hysteresis during reactive high power impulse magnetron sputtering (R-HiPIMS)? *J. Appl. Phys.* **121** 080901
[19] Lundin D, Gudmundsson J T, Brenning N, Raadu M A and Minea T M 2017 A study of the oxygen dynamics in a

reactive Ar/O_2 high power impulse magnetron sputtering discharge using an ionization region model *J. Appl. Phys.* **121** 171917
[20] Kubart T and Andersson J 2012 Modelling of target effects in reactive HIPIMS *IOP Conf. Ser.: Mater. Sci. Eng.* **39** 012008
[21] Haviar S, Čapek J, Batková Š, Kumar N, Dvořák F, Duchoň T, Fialová M and Zeman P 2018 Hydrogen gas sensing properties of WO_3 sputter-deposited thin films enhanced by on-top deposited CuO nanoclusters *Int. J. Hydrog. Energy* **43** 22756–64
[22] Kumar N, Čapek J and Haviar S 2020 Nanostructured $CuWO_4/WO_{3-x}$ films prepared by reactive magnetron sputtering for hydrogen sensing *Int. J. Hydrog. Energy* **45** 18066–74
[23] Kumar K U, Bhat S D and Subrahmanyam A 2019 Electrochromic device with magnetron sputtered tungsten oxide (WO_3) and nafion membrane: performance with varying tungsten oxide thickness- a report *Mater. Res. Express.* **6** 045513
[24] Wang W Q, Wang X L, Xia X H, Yao Z J, Zhong Y and Tu J P 2018 Enhanced electrochromic and energy storage performance in mesoporous WO_3 film and its application in a bi-functional smart window *Nanoscale* **10** 8162–9
[25] Kalanur S S, Heo J, Yoo I H and Seo H 2017 2D WO_3 decorated with Pd for rapid gasochromic and electrical hydrogen sensing *Int. J. Hydrog. Energy* **42** 16901–8
[26] Kozák T and Pajdarová A D 2011 A non-stationary model for high power impulse magnetron sputtering discharges *J. Appl. Phys.* **110** 103303
[27] Čapek J and Kadlec S 2017 Return of target material ions leads to a reduced hysteresis in reactive high power impulse magnetron sputtering: experiment *J. Appl. Phys.* **121** 171911
[28] Kubart T and Aijaz A 2017 Evolution of sputtering target surface composition in reactive high power impulse magnetron sputtering *J. Appl. Phys.* **121** 171903
[29] Mutzke A, Schneider R, Eckstein W and Dohmen R 2011 SDTrimSP Version 5.00
[30] Houska J and Kozak T 2020 Distribution of O atoms on partially oxidized metal targets, and the consequences for reactive sputtering of individual metal oxides *Surf. Coat. Technol.* **392** 125685
[31] Kozák T, Vlček J and Kos Š 2013 Transport and ionization of sputtered atoms in high-power impulse magnetron sputtering discharges *J. Phys. D: Appl. Phys.* **46** 105203
[32] Huo C, Lundin D, Gudmundsson J T, Raadu M A, Bradley J W and Brenning N 2017 Particle-balance models for pulsed sputtering magnetrons *J. Phys. D: Appl. Phys.* **50** 354003
[33] Hajihoseini H, Cada M, Hubička Z, Ünaldi S, Raadu M A, Brenning N, Gudmundsson J T and Lundin D 2019 The effect of magnetic field strength and geometry on the deposition rate and ionized flux fraction in the HiPIMS discharge *Plasma* **2** 201–21
[34] Gudmundsson J T 2002 Notes on the electron excitation rate coefficients for argon and oxygen discharge (http://raunvisindastofnun.hi.is/sites/raunvisindastofnun.hi.is/files/rh-21-2002.pdf)
[35] Blanco F, da Silva F F, Limão-Vieira P and García G 2017 Electron scattering cross section data for tungsten and beryllium atoms from 0.1–5000 eV *Plasma Sources Sci. Technol.* **26** 085004
[36] Krishnakumar E and Srivastava S K 1992 Cross-sections for electron impact ionization of O_2 *Int. J. Mass Spectrom. Ion Process.* **113** 1–12
[37] Gudmundsson J T 2004 A critical review of the reactions set for a low pressure oxygen processing discharge (https://raunvisindastofnun.hi.is/sites/raunvisindastofnun.hi.is/files/rh-17-2004.pdf)
[38] Lee C 1994 Global model of plasma chemistry in a high density oxygen discharge *J. Electrochem. Soc.* **141** 1546
[39] Bowes M and Bradley J W 2014 The behaviour of negative oxygen ions in the afterglow of a reactive HiPIMS discharge *J. Phys. D: Appl. Phys.* **47** 265202
[40] Behrish R 1983 *Sputtering by Particle Bombardment II* (Berlin: Springer) (https://doi.org/10.1007/3-540-12593-0)
[41] Hemberg A, Dauchot J-P, Snyders R and Konstantinidis S 2012 Evaporation-assisted high-power impulse magnetron sputtering: the deposition of tungsten oxide as a case study *J. Vac. Sci. Technol.* A **30** 040604
[42] Hala M, Capek J, Zabeida O, Klemberg-Sapieha J E and Martinu L 2012 Hysteresis-free deposition of niobium oxide films by HiPIMS using different pulse management strategies *J. Phys. D: Appl. Phys.* **45** 055204
[43] Anders A, Andersson J and Ehiasarian A 2007 High power impulse magnetron sputtering: current-voltage-time characteristics indicate the onset of sustained self-sputtering *J. Appl. Phys.* **102** 113303
[44] Gudmundsson J T, Brenning N, Lundin D and Helmersson U 2012 High power impulse magnetron sputtering discharge *J. Vac. Sci. Technol.* A **30** 030801
[45] Kozák T and Lazar J 2018 Gas rarefaction in high power impulse magnetron sputtering: comparison of a particle simulation and volume-averaged models *Plasma Sources Sci. Technol.* **27** 115012
[46] Anders A 2010 Deposition rates of high power impulse magnetron sputtering: physics and economics *J. Vac. Sci. Technol.* A **28** 783–90
[47] Musil J, Baroch P, Vlček J, Nam K H and Han J G 2005 Reactive magnetron sputtering of thin films: present status and trends *Thin Solid Films* **475** 208–18
[48] Ganesan R, Murdoch B J, Treverrow B, Ross A E, Falconer I S, Kondyurin A, McCulloch D G, Partridge J G, McKenzie D R and Bilek M M M 2015 The role of pulse length in target poisoning during reactive HiPIMS: application to amorphous HfO_2 *Plasma Sources Sci. Technol.* **24** 035015
[49] Ganesan R, Akhavan B, Partridge J G, McCulloch D G, McKenzie D R and Bilek M M M 2017 Evolution of target condition in reactive HiPIMS as a function of duty cycle: an opportunity for refractive index grading *J. Appl. Phys.* **121** 171909

E

Tuning Stoichiometry and Structure of Pd-WO_{3-x} Thin Films for Hydrogen Gas Sensing by High-Power Impulse Magnetron Sputtering

N. Kumar, S. Haviar, J. Rezek, P. Baroch, P, Zeman

Materials 13 (2020) 5101

materials

Article

Tuning Stoichiometry and Structure of Pd-WO_{3-x} Thin Films for Hydrogen Gas Sensing by High-Power Impulse Magnetron Sputtering

Nirmal Kumar, Stanislav Haviar *, Jiří Rezek, Pavel Baroch and Petr Zeman

Department of Physics and NTIS—European Centre of Excellence, Faculty of Applied Sciences, University of West Bohemia, Univerzitní 8, 306 14 Plzeň, Czech Republic; kumarn@kfy.zcu.cz (N.K.); jrezek@ntis.zcu.cz (J.R.); pbaroch@kfy.zcu.cz (P.B.); zemanp@kfy.zcu.cz (P.Z.)

* Correspondence: haviar@ntis.zcu.cz

Received: 4 October 2020; Accepted: 6 November 2020; Published: 12 November 2020

Abstract: By tuning the deposition parameters of reactive high-power impulse magnetron sputtering, specifically the pulse length, we were able to prepare WO_{3-x} films with various stoichiometry and structure. Subsequently, the films were annealed in air at moderate temperature (350 °C). We demonstrate that the stoichiometry of the as-deposited films influences considerably the type of crystalline phase formed in the annealed films. The appropriate sub-stoichiometry of the films (approx. $WO_{2.76}$) enabled crystallization of the monoclinic phase during the annealing. This phase is favorable for hydrogen sensing applications. To characterize the sensory behavior of the films, the tungsten oxide films were decorated by Pd nanoparticles before annealing and were assembled as a conductometric gas sensor. The sensory response of the films that crystallized in the monoclinic structure was proven to be superior to that of the films containing other phases.

Keywords: tungsten oxide; WO_3; hydrogen sensing; conductometric gas sensor; HiPIMS; stoichiometry

1. Introduction

Hydrogen is a reliable and prospective source of energy because of its clean and renewable essence. The growing hydrogen industry puts pressure to develop new hydrogen sensors associated mainly with hydrogen mobility and energy storage. Cheap, reliable, and greenway syntheses are desired as well as well-performing materials which include applications not only to hydrogen storage and production but also to hydrogen sensing for security and/or performance monitoring.

Metal oxide semiconductors (MOSs) are the most used class of sensing materials due to their diverse composition, tunable bandgap properties, possible nanostructuring, and high chemical stability. They have been widely studied for being used as conductometric sensors, where the change of resistivity upon hydrogen presence was monitored [1,2]. Among MOSs, tungsten oxide (WO_3) has attracted attention for the last few decades because of its interesting electrical, structural, and chemical properties [3,4]. Pure WO_3 can easily detect oxidizing gases such as NO_2, SO_2, O_3, etc. [5–10], but more challenging is an enhancement of its sensitivity towards reducing gases (H_2, CO, NH_3, etc.). This can be done by the loading of WO_3 material by noble catalysts such as Au, Pt, and Pd [1,3,11–13].

Magnetron sputtering is a deposition technique that enables the microstructure to be controlled and the physical properties of the films to be tuned [14]. Reactive magnetron sputtering is popular because it is capable of producing compound films (including MOSs) with various stoichiometries and structures [15–17]. Among a wide variety of magnetron sputtering techniques, reactive high-power impulse magnetron sputtering (HiPIMS) is a prominent technique for the preparation of high-quality compound films. During the process, a reactive gas (e.g., O_2) is dissociated, which improves its

reactivity [18,19] and allows for the tuning of the stoichiometry and structure to be easier. Using HiPIMS, it is possible to alter the optical and electrical properties of thin films by varying the target power density [20]. At the same time, crystalline films can be synthesized at lower deposition temperatures compared to traditional sputtering techniques. Concerning the demands of applications to sensors, there are also a few disadvantages of HiPIMS, mainly the fact that most of the prepared films are dense and smooth.

Despite the aforementioned advantages, the preparation of tungsten oxide films by HiPIMS has rarely been reported [21,22]. In this work, we demonstrate a low-temperature (200 °C) synthesis of sub-stoichiometric WO_{3-x} films with a diverse structure by controlling the deposition parameters during reactive HiPIMS. We decorate the deposited films with Pd nanoparticles, which is a common way to increase the selectivity towards hydrogen; the catalytic behavior of Pd lowers the activation energy and thus the operating temperature range, as explained in the sensing mechanism [1,23,24]. We investigate and discuss the influence of the stoichiometry and structure on the hydrogen sensing performance of the prepared films in detail. The films are not subjected to high-temperature post-annealing and are annealed and stabilized only at the measurement temperature (below 350 °C) of the response of the sensor.

2. Experimental Section

2.1. Material Synthesis

Pd-WO_{3-x} films were prepared by a two-step deposition process onto 9 × 9 mm^2 thermally oxidized Si substrates cleaned in an ultrasound bath in acetone, isopropyl alcohol, and deionized water for 10, 10, and 5 minutes, respectively.

The depositions were carried out in a cylindrical stainless-steel chamber (Z400, Leybold-Heraeus LH, Cologne, Germany, with a volume of 25 L and diameter of 42 cm, target-to-substrate distance of 70 mm) pumped by a turbomolecular pump (690 L/s for N_2) supported by a scroll pump. The base pressure for all depositions was below 4×10^{-3} Pa.

In the first step, WO_{3-x} films were deposited using a metallic W target (99.95% purity) with a diameter of 72 mm connected to a high-power pulsed DC power supply (SIPP2000 USB, Melec, Baden-Baden, Germany) run at a fixed average power of 100 W with a pulse length in the range of 50–800 μs. The waveforms of the target voltage and current were recorded by a digital oscilloscope (TBS 2104, Tektronix Inc., Beaverton, OR, USA). A deposition temperature of 200 °C was kept constant for all depositions. Before the deposition, the pumping speed was adjusted (by a throttle valve) to achieve a pressure of 0.5 Pa at Ar flow rate of 15 sccm. Then, the oxygen gas was introduced as a reactive gas and its flow was automatically controlled to maintain a total pressure of 0.75 Pa.

One of the presented films was also deposited in the DC regime at the same average target power (100 W) but slightly changed the gas composition (i.e., O_2:Ar was 1:2 for HiPIMS and 1:4 for DC). These are optimized conditions from the point of view of achieving a good crystallinity via DC sputtering at a substrate temperature of 200 °C.

The deposition rate was measured ex situ for each set of parameters by scanning a profile of a partially covered substrate by a profilometer. Then, the deposition time was adjusted to prepare films of a fixed thickness of 100 nm.

In the second step, the Pd deposition was carried out by using diode sputtering in RF mode at a power of 294 W (DC potential of 2.4 kV). The deposition time was 2 s, and the substrates were kept at room temperature.

2.2. Film Characterization

The morphology and topography of the films were examined by scanning electron microscopy (SEM; SU-70, Horiba Ltd., Kyoto, Japan) acquiring secondary electron image at 5 kV. The cross-sectional views of as-deposited films were used to verify the thickness of the films. For such imaging,

the prescratched specimens were broken at ambient temperature. The aforementioned SEM system was used to investigate the elemental composition (stoichiometry) of the films by means of wavelength dispersive spectroscopy (WDS; Magnaray, Thermofisher Scientific, Waltham, MA, USA) done using standard reference samples of pure W and Fe_2O_3 (hematite) (Astimex Scientific Ltd.). Since it is difficult to precisely quantify the composition of thin films by employing WDS, thick films (thicker than 600 nm) were deposited deliberately to measure the composition of tungsten oxide films. These thicker films were deposited immediately after the deposition of the 100 nm thin films, while keeping the same deposition parameters.

The structure of the as-deposited films was analyzed by X-ray diffraction (XRD) using a diffractometer (X'Pert PRO, PANanalytical, Malvern, UK) with Cu K_α source of radiation in the Bragg–Brentano configuration with an ω-offset of 1.5°. The ω-offset was used to eliminate a strong reflection of the single-crystalline Si(100) substrate at 2θ angle of 69.17°. The Raman spectroscopy (LABRAM HR Evolution, Horiba Jobin Yvon, Palaiseau, France), using a 532 nm laser, was also employed to confirm the phase composition.

A custom-built system was used to measure the gas response employing the four-point probe technique to calculate the change in the film electrical resistance in a time-varying gas mixture (H_2 + synthetic air) and at a controlled temperature. For stable electrical contacts, four gold-plated spring-loaded pins with a 1 mm separation were pressed to the specimen surface placed in a cylindrical brass chamber (total volume of 3 cm^3) heated by a hot plate. An independent thin thermocouple (0.3 mm thick) was pressed to the top surface to measure the temperature at the surface of the specimen. The flow of the gases was controlled by three separate mass flow controllers (Alicat Scientific Ltd., Tucson, AZ, USA). The resulting gas mixture was let to flow into the chamber with a total flow rate of 100 sccm. A DC source (KEITHLEY 6220, Keithley, Solon, OH, USA) and two electrometers (KEITHLEY 6514) were used for the electrical measurement. More details can be found in Ref. [25].

In this work, the sensitivity (S) at a specified concentration of H_2 gas (c) and temperature (T) is defined as:

$$S(c, T) = \frac{R_a}{R_g} \quad (1)$$

where R_a and R_g are the steady electrical resistances in the presence of synthetic air and H_2 gas mixed with air, respectively. The values of R_a and R_g are obtained by fitting the resistance $R(t)$ data by a sum of two exponential decays (in time t) with respect to Equation (2) in Reference [26].

3. Results and Discussion

To study the influence of the stoichiometry and structure of WO_{3-x} on the sensory response of Pd-WO_{3-x} films, a series of these films was prepared and studied. The presented results come from a set of specimens, where the average target power in a period during the deposition of tungsten oxide was kept constant and equal to 100 W, but the pulse length (T_{on}) was varied from 50 to 800 µs. The duty cycle was also kept constant (1%), and therefore the average pulse target power density was 245.6 W/cm^2 for all specimens. In addition to the discussion on the influence of the HiPIMS method, we also included one tungsten oxide film deposited in the DC regime. In this case, the average target power density was 2.46 W/cm^2. From this point on, the films are referred to with respect to T_{on}, e.g., "200 µs" film or "DC" film.

After the deposition of all WO_{3-x} films in this series, a thin film (equivalent thickness lower than 1 nm) of Pd was deposited as a second deposition step. The coalescence of palladium on the surface occurs and Pd forms spherical nanoparticles. The appearance of the particles after stabilization of the films is shown in SEM micrographs in Figure 1. Despite the surface morphology of various films differing, we observed a comparable size of Pd particles formed by coalescence on all WO_{3-x}. A discussion of the influence of the size of the Pd particles on the sensitivity of the films is out of the scope of this work. For further discussion, it is important only that the number of Pd particles varies in a range of approx. 60%, but the particles are similar in shape and size. See Supplementary

Material containing an image analysis (Figure S1) and particle statistics (Figure S2) for the micrographs presented in Figure 1c,d. The changes are most probably connected to a different time of stabilization of different specimens. However, the same total amount of Pd material is guaranteed by its deposition onto all WO_{3-x} films at one run.

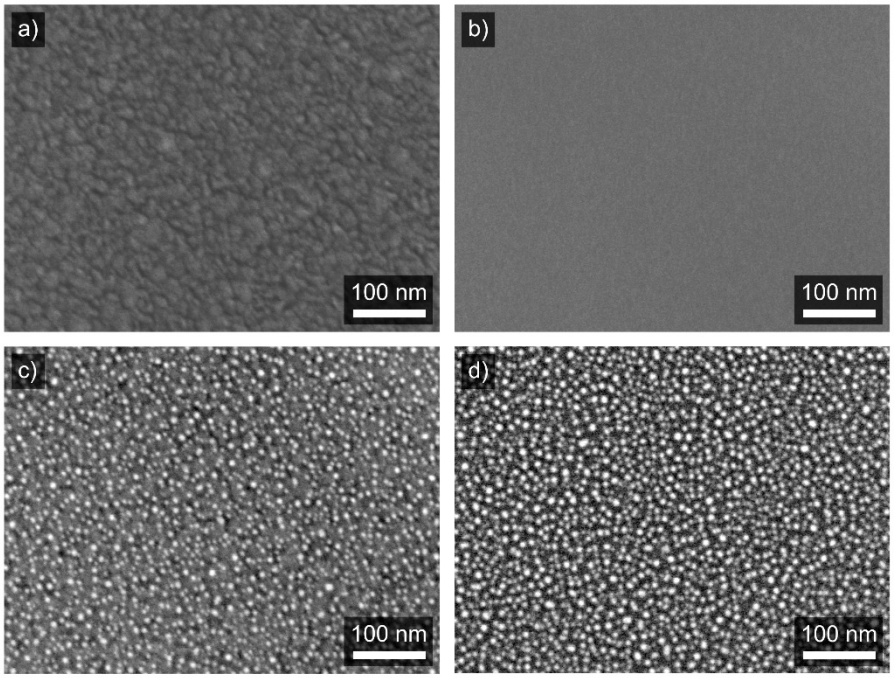

Figure 1. SEM micrographs of as-deposited (**a**,**b**) and Pd decorated tungsten oxide films after stabilization (**c**,**d**) for 100 µs and 800 µs films, respectively. It is clearly visible in (**c**,**d**) that the Pd particles in different films exhibit similar nature (shape and size).

In the following sections, we describe the influence of the deposition parameters on the stoichiometry of the as-deposited films. Then, we compare the structure of the films in the as-deposited state with those which were stabilized during the sensory measurements at an elevated temperature (350 °C) by means of XRD and Raman spectroscopy. Finally, the hydrogen sensory response is presented and completed with a general discussion.

3.1. Deposition Parameters and Composition

Target current density and voltage waveforms for different values of T_{on} are shown in Figure 2. The shape of the current density waveforms is typical for reactive HiPIMS under these discharge conditions: a current density peak in the beginning of the pulse and a gradual decrease of the current density towards the end of the pulse due to the rarefaction of the sputtering gas [27]. The peak values of the current density values are 0.55, 0.43, 0.32, 0.31, and 0.49 A/cm^{-2} at a 800, 500, 200, 100, and 50 µs pulse length, respectively. The unexpected high value and different shape of the current density for T_{on} = 50 µs can be explained by two effects. Mainly, the pulse ends after 50 µs, where other pulses achieve their maxima. Secondly, the deposition was carried out lastly after numerous experiments, and the target was more eroded, resulting in a stronger magnetic field and thus increasing plasma conductivity.

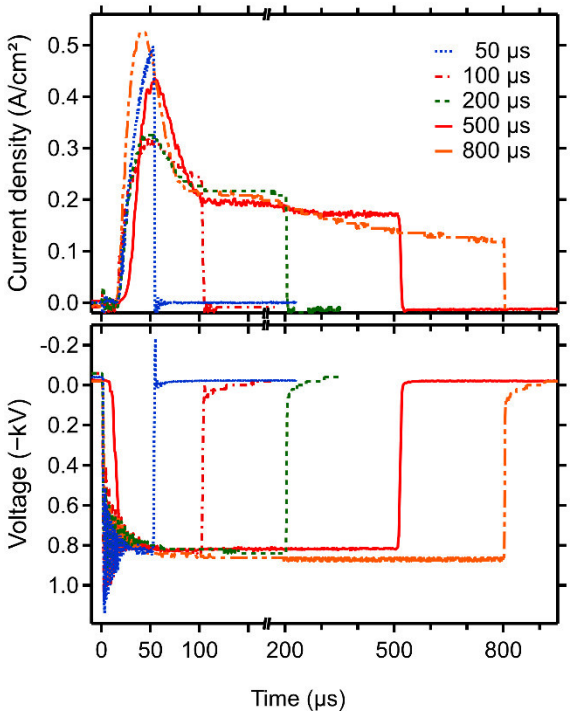

Figure 2. Voltage and current waveforms from deposition of high-power impulse magnetron sputtering (HiPIMS) films.

The effect of the HiPIMS parameters on the elemental composition of the deposited films is demonstrated in Figure 3, where WDS results are shown. The stoichiometry of the films calculated as a ratio of the atomic concentration of oxygen and tungsten is displayed in the tags in Figure 3 as well. A decrease in the oxygen concentration with increasing T_{on} from 50 to 800 µs was observed. In reactive HiPIMS, there is target poisoning that is crucial at a shorter T_{on}. It means that the reactive gas (O_2) easily produces a compound layer on the target surface and the sputtering yield decreases. This affects the amount of oxygen in the deposited material, which results in changes in the stoichiometry of the films. However, the target poisoning is moderate at higher pulse lengths, which reduces the thickness of the compound layer and produces an excessive amount of metal ions [28,29].

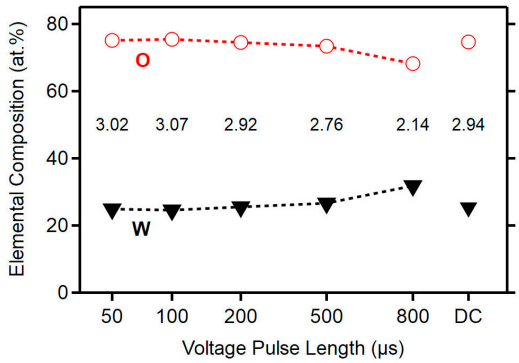

Figure 3. Elemental composition of films and stoichiometry. The stoichiometry ([W]/[O] ratio) decreases with an increasing voltage pulse length; the DC film is slightly sub-stoichiometric.

3.2. Structure

A comparison of XRD patterns of as-deposited films and annealed films (stabilized during the sensory measurements at 350 °C) is shown in Figure 4. As for the deposited films (grey traces), 500 µs and 800 µs films are found to be amorphous, while 50 µs, 100 µs, 200 µs, and DC films are crystalline or

nanocrystalline. Due to the overlapping of relatively broad diffraction peaks, it is, however, unfavorable to unambiguously determine a dominant phase in each film. Only the pattern of DC film corresponds well to that of the tetragonal WO_3 phase (PDF Card No. 04-007-0954). In the case of 50 μs and 100 μs films, it seems that the major phase is tetragonal, but the presence of triclinic/anorthic (PDF Card No. 01-073-6498) and monoclinic (PDF Card No. 01-083-0950) phases cannot be unambiguously excluded (see the powder diffraction standards in the figure).

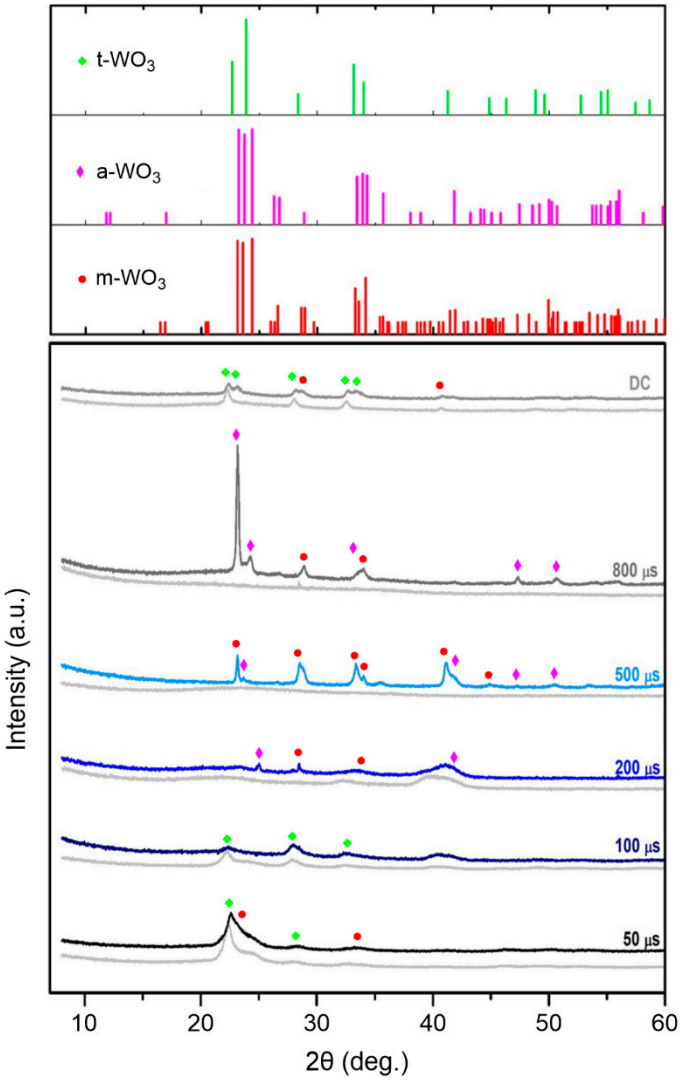

Figure 4. XRD patterns of as-deposited films (light grey) and annealed/stabilized films (color traces) after sensory measurements at 350 °C.

During measuring the sensory response to hydrogen (mixed with ambient air) at 350 °C, the crystalline/nanocrystalline structure of some films is changed (color patterns in Figure 4). The structure of the 50 μs and 100 μs films does not change significantly (very small changes in the pattern for the 50 μs film can imply the occurrence of the monoclinic phase). The relatively high stability of their structure can be attributed to their stoichiometry close to 3.0, i.e., no significant reaction with ambient oxygen occurs. Similar situation is also observed for the 200 μs film, where no pronounced changes in the structure are detected, and only a few crystallites of triclinic and/or monoclinic phase are formed. The situation is completely different in the case of the 500 μs and 800 μs films with the amorphous structure and low stoichiometry in the as-deposited state. These films in the as-deposited state exhibit the stoichiometry of 2.76 and 2.14, respectively. A possible reaction with ambient oxygen

results in a crystallization and stabilization of their structure with a dominant monoclinic WO_3 phase in the case of 500 µs film and a triclinic one in the case of 800 µs film. The patterns are very close to each other and the presence of both phases in each film cannot also be ruled out only based on XRD. In the case of the DC film, new diffraction peaks corresponding to the monoclinic phase appear, and this phase thus coexists with the tetragonal one after stabilization. It should be noted that no phases corresponding to the presence of Pd particles on the surface were detected.

The findings of XRD are supported by the results of Raman spectroscopy. The spectra of the as-deposited and annealed films are shown in Figure 5. Raman peaks at 263, 322, and 368 cm^{-1} are attributed to the deformation vibrations of W–O bonds, while the bands at 685, 704, and 797–803 cm^{-1} are the characteristics of stretching modes of O–W–O bonds [30–32]. Other features visible in the spectra are to be attributed to silicon substrate (mainly Si–Si peaks at 301, 616, 670 cm^{-1} and a broad feature at 935–975 cm^{-1}; Si–O peaks at 428 and 950 cm^{-1}).

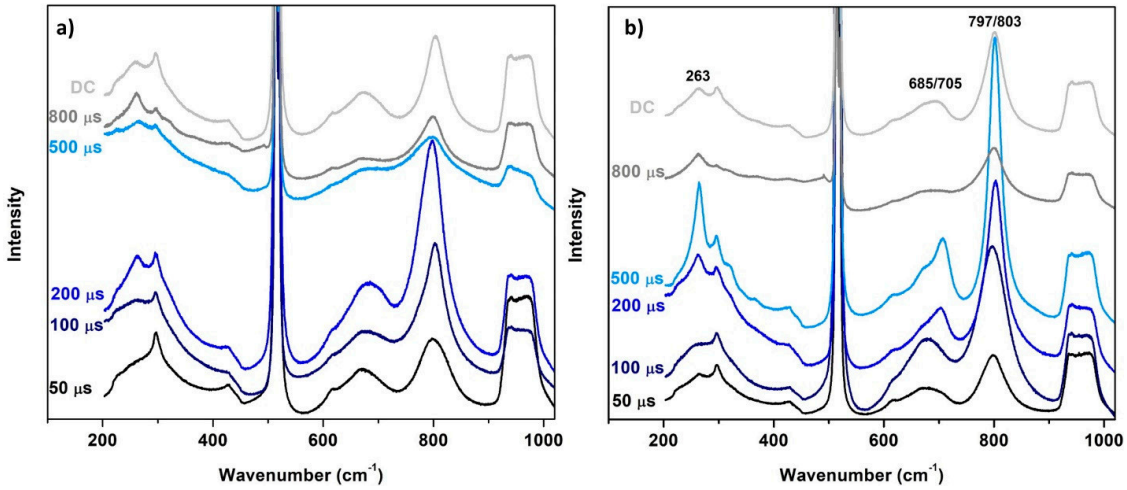

Figure 5. Raman spectra of (**a**) as-deposited films and (**b**) annealed films after sensory measurements at 350 °C.

The peaks appearing at approx. 685 and 797 cm^{-1} can imply several phases such as triclinic, tetragonal, or orthorhombic and therefore cannot be used to distinguish among them. However, the peak observed at 704 cm^{-1} in annealed 200 µs, 500 µs, and DC films corresponds exclusively to the monoclinic phase [32–34]. The monoclinic phase is also indicated by the shift of the peak at 797 cm^{-1} towards 803 cm^{-1}, which can also be observed for the 200 µs and 500 µs films. The spectrum of the annealed 500 µs film also shows peaks at 322 and 368 cm^{-1} which can be attributed to lower stretching modes of the triclinic phase [31,35]. These two peaks are also visible in the spectrum of the 800 µs film.

3.3. Sensory Response and Discussion

To characterize the sensory characteristics of the prepared films, the specimens were assembled as conductometric gas sensors and exposed to various concentrations of hydrogen gas in synthetic air at various temperatures. Firstly, the films were kept and measured at the highest examined temperature (350 °C) until the response was stable. This was demonstrated for the 500 µs film in Figure 6a where the response is stabilized after approx. 5 h (reaching 99% of the steady value) of the cycling of clean air and 1% of hydrogen. After the stabilization, the lower working temperatures were tested. The dependency of the sensitivity of selected films on working temperature is plotted in Figure 6b. The highest stable response was achieved at around 190 °C for all films. For the temperature at 350 °C, there is a visible increase of sensitivity for all films, which can be attributed to the onset of the thermal dissociation of hydrogen. The optimal temperatures (with the highest response) for particular specimens vary slightly

but do not differ much from 190 °C. Therefore, it is possible to compare the response of the investigated films at 190 °C, where the response approaches the maximum values for all investigated films.

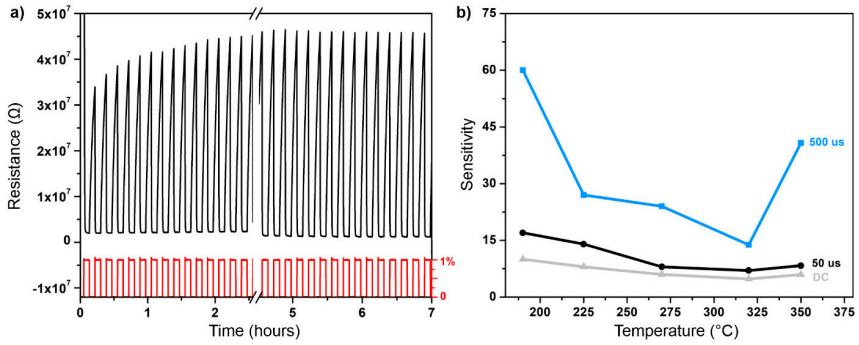

Figure 6. (**a**) Stabilization of the 500 µs film at 350 °C. The hydrogen in the concentration of 1% was cycled with a period of 5 min until the response was stable after approx. 5 h. (**b**) Sensitivity to 1% of H_2 for selected films at various temperatures.

A time dependence of the relative response (R_a/R_g) to a sequence of various hydrogen concentrations at a temperature of 190 °C is displayed in Figure 7. Here, one can compare the response of all films to the same amount of hydrogen. The highest response is plotted for 500 µs, 50 µs, and DC films; 100 µs and 200 µs films exhibit lower responses, and 800 µs film does not respond to hydrogen at all.

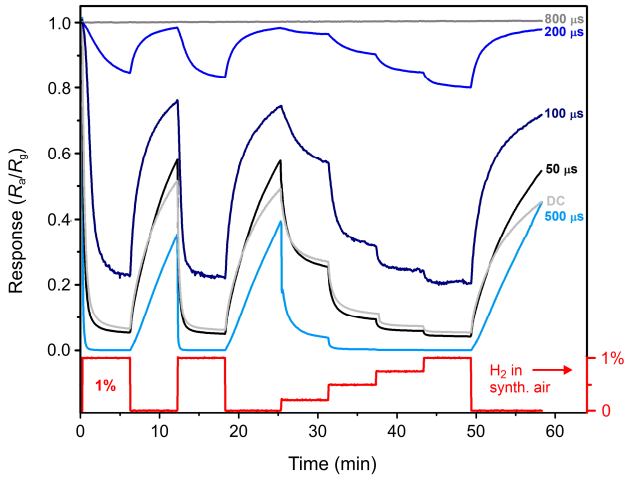

Figure 7. Relative response of all investigated films to the sequence of various hydrogen concentrations.

The presented data in Figure 7 corresponding to expositions to 1% of hydrogen were fitted with a sum of two exponential decays [26], and the sensitivity was calculated according to Equation (1). The obtained numerical values are summed up in Table 1.

Table 1. Important properties of the prepared films sorted by the acquired sensitivity to 1% of hydrogen. The stoichiometry of as-deposited films [O]/[W] is to be considered with an absolute error of 0.09 (based on the estimated errors of EDS analysis). The sheet resistance was measured at 190 °C in synthetic air.

Film	Sensitivity R_a/R_g	Crystallinity after Annealing	Crystalline Phases	Sheet Resist. (Ω/sq)	As-Deposited Stoichiometry	Response Time (s)
500 µs	60	moderate	monoclinic (triclinic)	3.4×10^8	2.76	10
50 µs	17	moderate	tetragonal + monoclinic	7.3×10^6	3.01	38
DC	10	moderate	tetragonal + monoclinic	1.2×10^6	2.94	70
100 µs	3.8	low	tetragonal + triclinic	1.7×10^5	3.07	113
200 µs	2.0	low	triclinic (monoclinic)	2.0×10^5	2.92	106
800 µs	–	high	triclinic (monoclinic)	6.3×10^2	2.15	–

The largest sensitivity is found for the 500 μs film, which exhibits almost pure monoclinic structure. The other two well-performing films (50 μs and DC) also show an evidence of the presence of the monoclinic phase, but the major phase remains tetragonal. One can identify a trend that the more crystalline is the film (and the more monoclinic), the higher sensitivity is achieved. This trend is also corroborated by poorly responding 100 μs and 200 μs films, whose crystallinity is low. Finally, the 800 μs film is well crystalline but of a very high conductivity. A possible explanation is that only the upper part of the material (most probably the very surface) oxidizes into crystalline trioxide. The rest of the material remains sub-stoichiometric and so with a high conductivity. Since the material is measured as a thin film, the total resistance is low, and the trioxide portion of the material does not affect the resistance and so the sensitivity of the film considerably.

The findings concerning crystalline phases are in good agreement with the works in References [36,37], where different crystalline structures of tungsten trioxide lead to considerably different responses. Here, the advantage is that the films were prepared just by a small variation of the power supply settings, which ends up in a possibility to control the stoichiometry.

One may also correlate the sensory response with the electrical resistance of the films. In Table 1, it is seen that the best-performing films are those with the highest resistance. A variation of resistance in oxides such as WO_3 is strongly connected with the concentration of oxygen vacancies. It has been shown that the oxygen vacancies play an important role in enhancing the performance of tungsten oxide material based sensors [38,39]. Nevertheless, the amount of oxygen vacancies must not prevent the proper crystallization, which is also important for the sensory response.

In our case, it was impossible to prepare the monoclinic phase directly in the as-deposited state. However, the prepared stoichiometry ([O]/[W] = 2.76 ± 0.09) of the 500 μs film was shown to be appropriate for providing a possibility to evolve the monoclinic structure during the stabilization and oxidization of the film at 350 °C in air and thus to form a film with a high resistance. In contrast, the 800 μs film was too sub-stoichiometric (2.15 ± 0.09) to reform completely into a trioxide crystalline film. The over-stoichiometry (3.07 ± 0.09) of the 100 μs film prevented it from transforming the crystalline structure at a relatively low annealing temperature. The stoichiometry (3.01 ± 0.09) of the 50 μs film and the light sub-stoichiometry (2.94 ± 0.09) of DC film provided a possibility for the formation of the monoclinic phase, but still the major phase remained tetragonal (see Figure 4). In the case of the 200 μs film, there is probably only a small portion of the material that can be reformed to the monoclinic phase, so the material responds to hydrogen, but not ideally.

Since the amount of the Pd particles and their shape are similar for all films, we deliberately exclude it from the discussion on the differences in the sensory behavior of individual films. However, it is indisputable and should not be forgotten that the catalytic effect of palladium is crucial for the sensory response of the films (Pd-free films do not sense, not shown), and Pd is fully responsible for lowering of the working temperature.

The focus of this work was to present a possibility of preparing hydrogen sensing films using the benefits of an environmentally friendly magnetron sputtering technique such as HiPIMS at low temperature. To conclude the discussion, we append Table 2 including similar architectures combining tungsten trioxide and noble metals (Pd or Pt) published in the literature. Most of the works have similar values of sensitivity but, for a few times, a lower hydrogen concentration. However, the sensitivity cannot be evaluated as a single parameter, and the table is presented to show that the response of our films is in a similar order. It should be noted that all of these materials were prepared mostly by wet processes such as sol-gel [40], screen-printing [3], etc. As one can see, the sensitivity of our best films is comparable to those that were usually prepared at higher temperatures. In our case, it was not necessary to sinter and/or anneal the material at higher temperatures and the best results were achieved when the specimens were deposited at 200 °C and stabilized at 350 °C. These conditions are closer to the application of hydrogen sensing films on temperature-sensitive substrates such as plastics.

Table 2. Comparison table of published materials combining tungsten trioxide with palladium or platinum. The appropriate definitions of sensitivity are noted for individual works.

Material	Response	Sensitivity Definition	Temperature, °C	Concentration, ppm	References
WO_3 thin film	5	$S = R_a/R_g$	150	250	[40]
Pd-WO_3 nanocomposites	19	$S = (R_a - R_g)/R_g$	200	200	[41]
Pt-WO_3 thin film	~5	$S = (R_a - R_g)/R_g$	400	500	[42]
Pd-Graphene QDs on WO_3 thin film	1.12	$S = (R_a - R_g)/R_g$	150	3600	[4]
Pt-WO_3 nanowires	20	$S = R_a/R_g$	200	100	[43]
Pd-WO_3 nanolamellae	69	$S = (R_a - R_g)/R_g$	180	200	[3]
Pd-WO_3	12	$S = R_a/R_g$	190	2000	This work
Pd-WO_3	60	$S = R_a/R_g$	190	10,000	This work

4. Conclusions

In this work, we demonstrated the suitability of a low-temperature (200 °C) synthesis of WO_{3-x} films by using the reactive high-power impulse magnetron sputtering technique. By changing the pulse length only, we were able to prepare the films with various stoichiometry and structure. Subsequently, the WO_{3-x} films were decorated by Pd particles and stabilized at 350 °C in air.

We showed that the stoichiometry affects not only the as-deposited structure but plays an important role in the structure of the stabilized films. While the crystalline or nanocrystalline films with the stoichiometry close to 3.0 are relatively thermally stable without significant changes in the structure during the stabilization, the amorphous films with the higher level of the sub-stoichiometry further oxidize and form well crystalline structures during the stabilization. The type of WO_3 phase is then a key factor determining the performance of the sensor to hydrogen. Particularly, the film with a stoichiometry of 2.76 ± 0.09 deposited under proper conditions by reactive HiPIMS crystallizes into the monoclinic structure during the stabilization at 350 °C in air and exhibits enhanced sensory ability to hydrogen than other crystalline phases (higher sensitivity).

A further development of this synthesis approach would lead to the application of tungsten trioxide based thin films on various substrates (such as plastics), which cannot withstand common techniques of synthesis at high temperatures. A further improvement of a direct deposition of the sensing film with the monoclinic WO_3 phase is desirable.

Supplementary Materials: The following are available online at http://www.mdpi.com/1996-1944/13/22/5101/s1, Figure S1: Binarized SEM micrograph. The Pd particles were masked by Otsu's method. Figure S2: Histogram of equivalent radius of Pd particles gained from SEM image analysis.

Author Contributions: N.K. carried out the deposition, material characterization, and sensitivity measurements and wrote the manuscript. J.R. designed and supervised the deposition. S.H. designed and supervised the deposition and material characterization, and reviewed the manuscript. P.B. provided consultation on the strategy. P.Z. provided consultation on the strategy and reviewed the manuscript. All authors have read and agreed to the published version of the manuscript.

Funding: This work was supported by the Czech Science Foundation under Project No. GA19-13174S.

Acknowledgments: The authors would like to thank R. Čerstvý for conducting the XRD measurements.

Conflicts of Interest: The authors declare no conflict of interest.

References

1. Moseley, P.T. Progress in the development of semiconducting metal oxide gas sensors: A review. *Meas. Sci. Technol.* **2017**, *28*, 082001. [CrossRef]
2. Phanichphant, S. Semiconductor Metal Oxides as Hydrogen Gas Sensors. *Procedia Eng.* **2014**, *87*, 795–802. [CrossRef]
3. Boudiba, A.; Roussel, P.; Zhang, C.; Olivier, M.-G.; Snyders, R.; Debliquy, M. Sensing mechanism of hydrogen sensors based on Pd loaded tungsten oxide (Pd-WO 3). *Sens. Actuators B Chem.* **2013**, *187*, 84–93. [CrossRef]
4. Fardindoost, S.; Zad, A.I.; Hosseini, Z.S.; Hatamie, S. Detecting hydrogen using graphene quantum dots/WO_3 thin films. *Mater. Res. Express* **2016**, *3*, 116407. [CrossRef]

5. Hübner, M.; Simion, C.E.; Haensch, A.; Barsan, N.; Weimar, U. CO sensing mechanism with WO_3 based gas sensors. *Sens. Actuators B Chem.* **2010**, *151*, 103–106. [CrossRef]
6. Prajapati, C.S.; Bhat, N. Ppb level detection of NO_2 using a WO_3 thin film-based sensor: Material optimization, device fabrication and packaging. *RSC Adv.* **2018**, *8*, 6590–6599. [CrossRef]
7. Shimizu, Y.; Matsunaga, N.; Hyodo, T.; Egashira, M. Improvement of SO_2 sensing properties of WO_3 by noble metal loading. *Sens. Actuators B Chem.* **2001**, *77*, 35–40. [CrossRef]
8. Susanti, D.; Perdana, A.S.; Purwaningsih, H.; Noerochim, L.; Kusuma, G.E. Preparation of CO gas sensor from WO_3 nanomaterial synthesized via sol-gel method followed by hydrothermal process. *AIP Conf. Proc.* **2014**, *1586*, 14–19.
9. Kaur, N.; Zappa, D.; Poli, N.; Comini, E. Integration of VLS-Grown WO_3 Nanowires into Sensing Devices for the Detection of H_2S and O_3. *ACS Omega* **2019**, *4*, 16336–16343. [CrossRef]
10. Godbole, R.; Vedpathak, A.; Godbole, V.; Bhagwat, S. Tungsten oxide thin films: Detection and trapping of hazardous gases. *Mater. Res. Express* **2017**, *4*, 076401. [CrossRef]
11. Hübert, T.; Boon-Brett, L.; Black, G.; Banach, U. Hydrogen sensors—A review. *Sens. Actuators B Chem.* **2011**, *157*, 329–352. [CrossRef]
12. Haviar, S.; Čapek, J.; Batková, Š.; Kumar, N.; Dvořák, F.; Duchoň, T.; Fialová, M.; Zeman, P. Hydrogen gas sensing properties of WO_3 sputter-deposited thin films enhanced by on-top deposited CuO nanoclusters. *Int. J. Hydrog. Energy* **2018**, *43*, 22756–22764. [CrossRef]
13. Ghasempour, R.; Mortazavi, S.; Zad, A.I.; Rahimi, F. Hydrogen sensing properties of multi-walled carbon nanotube films sputtered by Pd. *Int. J. Hydrog. Energy* **2010**, *35*, 4445–4449. [CrossRef]
14. Liang, Y.C.; Chang, C.W. Preparation of orthorhombic WO_3 thin films and their crystal quality-dependent dye photodegradation ability. *Coatings* **2019**, *9*, 90. [CrossRef]
15. Safi, I. Recent aspects concerning DC reactive magnetron sputtering of thin films: A review. *Surf. Coat. Technol.* **2000**, *127*, 203–218. [CrossRef]
16. Vlček, J.; Rezek, J.; Houška, J.; Kozák, T.; Kohout, J. Benefits of the controlled reactive high-power impulse magnetron sputtering of stoichiometric ZrO_2 films. *Vacuum* **2015**, *114*, 131–141. [CrossRef]
17. Musil, J.; Baroch, P.; Vlček, J.; Nam, K.H.H.; Han, J.G.G. Reactive magnetron sputtering of thin films: Present status and trends. *Thin Solid Films* **2005**, *475*, 208–218. [CrossRef]
18. Vlček, J.; Rezek, J.; Houška, J.; Čerstvý, R.; Bugyi, R. Process stabilization and a significant enhancement of the deposition rate in reactive high-power impulse magnetron sputtering of ZrO_2 and Ta_2O_5 films. *Surf. Coat. Technol.* **2013**, *236*, 550–556. [CrossRef]
19. Vlček, J.; Belosludtsev, A.; Rezek, J.; Houška, J.; Čapek, J.; Čerstvý, R.; Haviar, S. High-rate reactive high-power impulse magnetron sputtering of hard and optically transparent HfO_2 films. *Surf. Coat. Technol.* **2016**, *290*, 58–64. [CrossRef]
20. Rezek, J.; Houška, J.; Procházka, M.; Haviar, S.; Kozák, T.; Baroch, P. In-Ga-Zn-O thin films with tunable optical and electrical properties prepared by high-power impulse magnetron sputtering. *Thin Solid Films* **2018**, *658*, 27–32. [CrossRef]
21. Hemberg, A.; Dauchot, J.-P.; Snyders, R.; Konstantinidis, S. Evaporation-assisted high-power impulse magnetron sputtering: The deposition of tungsten oxide as a case study. *J. Vac. Sci. Technol. A Vac. Surf. Film.* **2012**, *30*, 040604. [CrossRef]
22. Ganesan, R.; Akhavan, B.; Partridge, J.G.; McCulloch, D.G.; McKenzie, D.R.; Bilek, M.M.M. Evolution of target condition in reactive HiPIMS as a function of duty cycle: An opportunity for refractive index grading. *J. Appl. Phys.* **2017**, *121*, 171909. [CrossRef]
23. Korotcenkov, G.; Cho, B.K.; Han, S.H.; Cho, B.K. Metal oxide composites in conductometric gas sensors: Achievements and challenges. *Sens. Actuators B Chem.* **2017**, *244*, 182–210. [CrossRef]
24. Wang, Y.; Liu, B.; Xiao, S.; Li, H.; Wang, L.; Cai, D.; Wang, D.; Liu, Y.; Li, Q.; Wang, T. High performance and negative temperature coefficient of low temperature hydrogen gas sensors using palladium decorated tungsten oxide. *J. Mater. Chem. A* **2015**, *3*, 1317–1324. [CrossRef]
25. Kumar, N.; Čapek, J.; Haviar, S. Nanostructured $CuWO_4/WO_3$-films prepared by reactive magnetron sputtering for hydrogen sensing. *Int. J. Hydrog. Energy* **2020**. submitted. [CrossRef]
26. Haviar, S.; Chlupová, Š.; Kúš, P.; Gillet, M.; Matolín, V.; Matolínová, I. Micro-contacted self-assembled tungsten oxide nanorods for hydrogen gas sensing. *Int. J. Hydrog. Energy* **2017**, *42*, 1344–1352. [CrossRef]

27. Hála, M.; Čapek, J.; Zabeida, O.; Klemberg-Sapieha, J.E.; Martinu, L. Pulse management in high power pulsed magnetron sputtering of niobium. *Surf. Coat. Technol.* **2012**, *206*, 4186–4193. [CrossRef]
28. Kozák, T.; Vlček, J. Dynamics of processes during the deposition of ZrO_2 films by controlled reactive high-power impulse magnetron sputtering: A modelling study. *J. Appl. Phys.* **2017**, *122*, 1–9. [CrossRef]
29. Kozák, T.; Vlček, J. A parametric model for reactive high-power impulse magnetron sputtering of films. *J. Phys. D. Appl. Phys.* **2016**, *49*, 055202. [CrossRef]
30. Szilágyi, I.M.; Fórizs, B.; Rosseler, O.; Szegedi, Á.; Németh, P.; Király, P.; Tárkányi, G.; Vajna, B.; Varga-Josepovits, K.; László, K.; et al. WO_3 photocatalysts: Influence of structure and composition. *J. Catal.* **2012**, *294*, 119–127. [CrossRef]
31. Kuzmin, A.; Purans, J.; Cazzanelli, E.; Vinegoni, C.; Mariotto, G. X-ray diffraction, extended X-ray absorption fine structure and Raman spectroscopy studies of WO[sub 3] powders and (1−x)WO[sub 3−y]·xReO[sub 2] mixtures. *J. Appl. Phys.* **1998**, *84*, 5515. [CrossRef]
32. Vinh, T.C.; Thinh, N.D.; Dat, H.T.; Tuan, T.; Phuong, D.A. Survey of WO_3 thin film structure built on ito/glass substrates by the Raman and xrd spectroscopies. *J. Sci. Math. Phys.* **2009**, *25*, 47–55.
33. Garcia-Sanchez, R.F.; Ahmido, T.; Casimir, D.; Baliga, S.; Misra, P. Thermal effects associated with the Raman spectroscopy of WO_3 gas-sensor materials. *J. Phys. Chem. A* **2013**, *117*, 13825–13831. [CrossRef] [PubMed]
34. Boulova, M.; Rosman, N.; Bouvier, P.; Lucazeau, G. High-pressure Raman study of microcrystalline WO_3 tungsten oxide. *J. Phys. Condens. Matter* **2002**, *14*, 5849–5863. [CrossRef]
35. Cazzanelli, E. Raman study of the phase transitions sequence in pure WO_3 at high temperature and in $HxWO_3$ with variable hydrogen content. *Solid State Ion.* **1999**, *123*, 67–74. [CrossRef]
36. Staerz, A.; Berthold, C.; Russ, T.; Wicker, S.; Weimar, U.; Barsan, N. The oxidizing effect of humidity on WO_3 based sensors. *Sens. Actuators B Chem.* **2016**, *237*, 54–58. [CrossRef]
37. Szilágyi, I.M.; Saukko, S.; Mizsei, J.; Tóth, A.L.; Madarász, J.; Pokol, G. Gas sensing selectivity of hexagonal and monoclinic WO_3 to H_2S. *Solid State Sci.* **2010**, *12*, 1857–1860. [CrossRef]
38. Yu, W.; Shen, Z.; Peng, F.; Lu, Y.; Ge, M.; Fu, X.; Sun, Y.; Chen, X.; Dai, N. Improving gas sensing performance by oxygen vacancies in sub-stoichiometric WO_3−x. *RSC Adv.* **2019**, *9*, 7723–7728. [CrossRef]
39. Gali, P.; Sapkota, G.; Syllaios, A.J.; Littler, C.; Philipose, U. Stoichiometry dependent electron transport and gas sensing properties of indium oxide nanowires. *Nanotechnology* **2013**, *24*, 225704. [CrossRef]
40. De Marcellis, A.; Ferri, G.; Mantenuto, P.; Giancaterini, L.; Cantalini, C. WO_3 hydrogen resistive gas sensor and its wide-range current-mode electronic read-out circuit. *IEEE Sens. J.* **2013**, *13*, 2792–2798. [CrossRef]
41. Boudiba, A.; Zhang, C.; Umek, P.; Bittencourt, C.; Snyders, R.; Olivier, M.G.; Debliquy, M. Sensitive and rapid hydrogen sensors based on Pd-WO_3 thick films with different morphologies. *Int. J. Hydrog. Energy* **2013**, *38*, 2565–2577. [CrossRef]
42. Bose, R.J.; Illyaskutty, N.; Tan, K.S.; Rawat, R.; Matham, M.V.; Kohler, H.; Pillai, V.P.M. Hydrogen sensors based on Pt-loaded WO_3 sensing layers. *Europhys. Lett.* **2016**, *114*, 66002. [CrossRef]
43. Vallejos, S.; Grácia, I.; Chmela, O.; Figueras, E.; Hubálek, J.; Cané, C. Chemoresistive micromachined gas sensors based on functionalized metal oxide nanowires: Performance and reliability. *Sens. Actuators B Chem.* **2016**, *235*, 525–534. [CrossRef]

5 Conclusions

The main objective of this thesis was to propose and systematically investigate the materials suitable for gas sensing applications and to find strategies to improve their properties. Along with the development of WO_3 thin film-based gas sensor and enhancing the sensing response by combining various structures of CuO, Pd/PdO, and $CuWO_4$ materials, the development of the gas sensitivity testing apparatus was also an important part of this work. The main achievements which can confirm the fulfillment of all the objectives of this work can be summarized as follows:

1. The sensitivity measurement setup described in Section 2.2d) on page 22 has been successfully developed. The setup is designed by employing the four-point probe technique, and the routine process to collect the data for hydrogen detection is programmed at various parameters. A LabVIEW-driven program allows to control the inset values of temperature with time and also control the concentration of the hydrogen volume percent in synthetic air. The relative humidity in the gas transport can also be varied by controlling the flows of dry and humid portions of the air.

2. The crystallinity in WO_3 and CuO is achieved at 400 °C in an $Ar:O_2$ ratio 1:4 and 1:2, respectively. The WO_3 and CuO films were deposited by reactive sputtering technique in the DC and RF regime, respectively, in a two-step deposition process to synthesize $CuWO_4$ on the WO_3 or CuO backbone layer (Chapter 4 Sections B and C). Furthermore, the deposition temperature for crystalline WO_3 films is reduced to 200 °C by employing HiPIMS (Chapter 4 Section E). The important result is that WO_3 can be easily deposited by HiPIMS on substrates that cannot stand higher deposition temperatures.

3. The results presented in Chapter 4 Section D demonstrate the successful implementation of a combined model for the ionization region of plasma discharge and model for the reactive HiPIMS. The change in the average power density varies the deposition rate and the oxygen content in the WO_{3-x} films. The long length of the voltage pulse results in lower oxygen content, while the short pulse gives a higher oxygen content in the WO_{3-x} films probably due to the rarefaction of oxygen due to the sputtering wind. The change in the voltage pulse length results in various crystalline structures with different stoichiometries (Chapter 4 Section E). The crystalline phases and structure evolve further after stabilizing the films at 350 °C in air. The amorphous sub-stoichiometric films with a higher metal content further oxidize during stabilization and form a well-crystalline structure.

4. Various combinations of MOS such as CuO nanoclusters with WO_3, $CuWO_4$ with WO_{3-x}, Pd, $CuWO_4$, with CuO, and Pd nanoparticles with WO_3 are studied to improve the sensing response towards H_2 gas. The WO_3 films were decorated with various densities of CuO nanoclusters and the sensing response to H_2 detection is significantly improved (Chapter 4 Section A). P-type CuO nanoclusters and N-type WO_3 films formed a nano-sized PN junction at the interface which tuned the conductive channel of the WO_3 film. The

sequential deposition of CuO on WO_{3-x} at 400 °C leads to the formation of $CuWO_4$ nanoislands on WO_{3-x} film. The sensing response improved due to the formation of an NN-type heterojunction at the $CuWO_4/WO_{3-x}$ interface (Chapter 4 Section B). Similarly, in the case of $CuWO_4$/CuO in Chapter 4 Section C, the sensing response is better than pure CuO and WO_3 and is further enhanced by deposition of Pd nanoparticles and PdO nanoislands on $CuWO_4$/CuO bilayers.

5. The operating temperature of the gas sensor is lowered significantly (Chapter 4 Sections C and E). The optimal temperature for the best sensing response is reduced to 150 ° C by loading the films with Pd nanoparticles that work as a catalyst on the surface of the WO_{3x} films (Chapter 4 Section E) and $CuWO_4$/CuO films (Chapter 4 Section C). Some of the samples respond even at 50 °C but the response is comparably low.

6. The influence of humidity is reduced by adding Pd on $CuWO_4$/CuO bilayers (Chapter 4 Section C). The response decreased after adding Pd but the humidity does not affect the sensing response, i.e., the response to H_2 is equalized in dry and humid environments at a lower temperature. This combination of materials fulfilled the fifth objective of the thesis.

6 Contribution to Conferences

6.1 Conference Proceedings

1. **Kumar, N.**, Haviar, S., Čapek, J., Batková, Š., Rezek, J., Zeman P., Baroch, P. *"Tungsten Oxide Based Hydrogen Gas Sensor Prepared by Advanced Magnetron Sputtering Techniques"*. Dresden, Germany, 2021. DOI:10.3390/I3S2021Dresden-10154

2. Haviar, S., **Kumar, N.**, Batková, Š., Čapek, J. *"Nanostructured Materials Based on Thin Films and Nanoclusters for Hydrogen Gas Sensing"*. Proceedings MDPI, 4th International Conference nanoFIS 2020-Functional Integrated nano systems. DOI:10.3390/proceedings2020056038

6.2 International Conference Presentations

1. EUROMAT 2021 (Virtual)
   Kumar, N., Haviar, S., Rezek, J., Zeman P., Baroch, P. *"HiPIMS deposited Pd-WO_{3-x} Thin Films with tuned Structure and stoichiometry for Hydrogen Gas Sensing.* Graz, Austria 2021. **(Oral Presentation)**

2. I3S 2021 8th Symposium on sensor science– Dresden, Germany (Virtual)
   Kumar, N., Haviar, S., Čapek, J., Batková, Š., Rezek, J., Zeman P., Baroch, P. *"Tungsten Oxide Based Hydrogen Gas Sensor Prepared by Advanced Magnetron Sputtering Techniques"*. Dresden, Germany, 2021. **(Poster Presentation)**

3. ICMCTF 2021 – San Diego, USA (Virtual)
   Kumar, N., Haviar, S., Čapek, J., Batková, Š., Rezek, J., Zeman P., Baroch, P. *"Nanostructures CuO -WO_3 Thin Films for hydrogen gas sensing Prepared by Advanced Magnetron Sputtering Techniques"*. San Diego, U.S.A., 2021. **(Oral Presentation)**

4. PSE Satellite 2020 – Prague, Czech Republic
   Kumar, N., Haviar, S., Baroch, P. *"Reactive sputter deposited $CuWO_4$/ WO_3 nanostructured bilayers for hydrogen gas sensing"*. Prague, Czech Republic, 2020. **(Poster Presentation)**

5. RSD 2019 – Braunswick, Germany
   Kumar, N., Haviar, S, Rezek, J., Baroch, P. *"Reactive sputter deposited $CuWO_4$ / WO_3 nanostructured bilayers for hydrogen gas sensing"*. Braunschweig, Germany, 2019. **(Oral Presentation).**

6. JVC 2019- Malmo, Sweden

Haviar, S., **Kumar, N.**, Batková, Š., Čapek, J. *"Nanocluster-Based Metal Oxide Films for Hydrogen Gas Sensing Prepared by Advanced Magnetron Sputtering Techniques".* Malmö, Sweden, 2019. **(Co-author in Oral Presentation)**

7. **EMRS 2019 – Nice,**
   Kumar, N., Haviar, S., Baroch, P. *"Hydrogen gas sensor based on WO_3 and CuO thin films and nanoclusters".* Nice, France, 2019. **(Poster Presentation)**

8. ICMCTF 2019 – San Diego, USA
   Haviar, S., Čapek, J., Batková S., **Kumar, N.** *"Nanocluster-Based Metal Oxide Films for Hydrogen Gas Sensing". San Diego, USA, 2019.* ***(Co-author in Oral Presentation)***

9. PSE 2018 – Garmisch-Partenkirchen, Germany
   Kumar, N., Haviar, S., Čapek, J., Batková, S., Baroch, P. *"Nanostructured Metal-Oxide Based Hydrogen Gas Sensor Prepared by Magnetron Sputtering".* Garmisch-Partenkirchen, Germany 2018. **(Poster Presentation)**

10. SAV 2017 – Pilsen, Czech Republic
    Kumar, N., Haviar, S., Čapek, J., Batková, Š., Baroch, P. *"Nanostructured metal-oxide based hydrogen gas sensor prepared by magnetron sputtering".* SAV Pilsen Czech Republic 2017 **(Oral Presentation)**